The STAR Forward Calorimeter System and Forward Tracking System

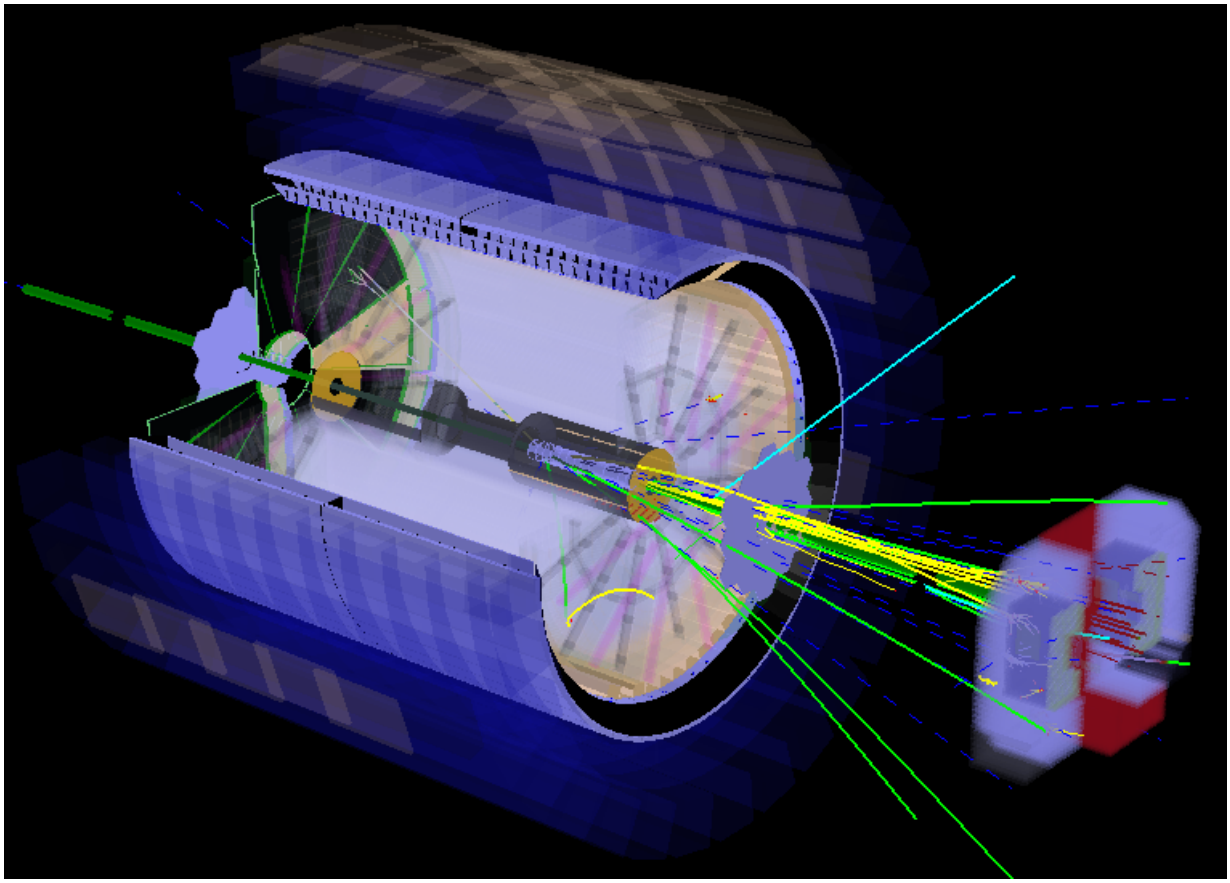

Proposal
November 2018

1 Executive Summary

Quantum Chromodynamics (QCD), the theory of strong interactions, is a cornerstone of the Standard Model of modern physics. It explains all strongly interacting matter in terms of point-like quarks interacting via the exchange of gauge bosons, known as gluons. This strongly interacting matter is responsible for 99% of the visible mass in the universe. Over the past several decades, QCD has proven to be a remarkably rich theory. Enormous progress has been made in computational techniques in many topical areas of QCD and quite remarkable observations have been made in experiment.

The theoretical and experimental achievements of the current US QCD facilities JLab and RHIC as well as the next pressing questions to be answered by the existing and the newly proposed facility the Electron Ion Collider (EIC) are detailed in the 2015 Long Range Plan [1].

By precisely imaging gluons and sea quarks inside the proton and nuclei, some of the deepest issues regarding the emergence of nuclear properties from QCD will be addressed. These issues include:

- How are the gluons and sea quarks, and their intrinsic spins, distributed in space and momentum inside the nucleon? What is the role of sea quark and gluon orbital motion in building the nucleon spin?
- What happens to the gluon density in nuclei at high energy? Does it saturate, giving rise to a gluonic matter component with universal properties in all nuclei, even the proton?
- How does the nuclear environment affect quark and gluon distributions and interactions inside nuclei? Do the abundant low-momentum gluons remain confined within nucleons inside nuclei?
- How does nuclear matter respond to a fast moving color charge passing through it? How do quarks of different flavor dress themselves in nuclear matter to emerge as colorless hadrons? What does this dressing process tell us about the mechanisms by which quarks are normally confined inside nucleons?

The outstanding p+p and p+A physics program as outlined in the 2016 RHIC Cold QCD Plan [2] and reviewed by the PAC in 2016 can address these questions in the next years preceding the EIC. This proposal gives a realization plan to address the 2016 PAC recommendation: “The PAC encourages the management and the collaborations to consider a potential (polarized) p+p and/or p+A program before 2024. In addition to the scientific benefits pointed out in the Cold QCD Report, this would help to keep the Cold QCD community active and engaged at RHIC, which might be important for the activities at BNL aiming at an EIC.” In 2018 the PAC recommendation was as follows “STAR presented a rich program for future operation after BES II that addresses many important and innovative topics in p+p, p+A and A+A physics. The most interesting of these is focused on forward physics that would be made possible by a forward upgrade covering rapidities up to 4.2 with $5.3 M further investment and would enable studies of novel reaction channels including several specific diffractive reactions and ultra-peripheral collisions of interest to hadron structure and QGP physics alike. Hadron structure measurements, such as diffractive dijet production, are highly relevant for the physics to be investigated at EIC, both for their e+p and e+A components and may help to further sharpen the EIC physics case. From the heavy-ion perspective, QGP vorticity and Lambda polarization measurements in peripheral collisions would address vorticity generation at the microscopic level. Several international groups have submitted or are ready to submit proposals to finance most of the needed cost-efficient forward hardware upgrades. We commend STAR for developing and sharpening this option, which enriches the range of future opportunities for BNL.”

The outlined measurements will be essential to fully realize the scientific promise of the EIC by providing a comprehensive set of measurements in hadronic collisions that, when combined with data from the EIC, will establish the validity and limits of factorization and universality. The outlined program will on the one hand lay the groundwork for the EIC, both scientifically and in terms of refining the experimental requirements for the physics program at the EIC, and thus be the

natural next step on the path towards an electron-ion collider. On the other hand, while much of the physics in this program is unique to proton-proton and proton-nucleus collisions and offers discovery potential on its own, when combined with data from the EIC it will provide a broad foundation to a deeper understanding of fundamental QCD.

This proposal details **only** the part of p+p and p+A physics program outlined in the RHIC Cold QCD Plan [2], which requires an upgrade to the forward rapidity ($2.5 < \eta < 4.$) detection capabilities of STAR (for a summary see Table 2-1). A brief discussion of STAR's ability concurrently to realize the mid-rapidity p+p and p+A physics program outlined in the RHIC Cold QCD Plan is given in a companion document [3].

The STAR forward upgrade is motivated mainly by exploration of cold QCD physics in the very high and low regions of Bjorken *x*. But it is specifically noted that the forward upgrade will also provide new detector capabilities at RHIC and STAR to explore the longitudinal structure of the initial state and the temperature dependent transport properties of matter in relativistic heavy ion collisions (for a summary of the A+A program see Table 2-2). A brief discussion of STAR's ability concurrently to realize a unique mid-rapidity A+A physics program is also outlined in the companion document [3].

Previous STAR efforts using the FPD and FMS detectors and the recently refurbished FMS and a new pre-shower and post-shower detector upgrade for Runs 2015-2017 have demonstrated that there are outstanding QCD physics opportunities in the forward region. In order to go beyond what STAR has already and will achieve with the currently existing forward detector system, a forward detector upgrade with superior detection capability for neutral pions, photons, electrons, jets and leading hadrons covering a pseudorapidity region of 2.5-4.5 in the years beyond 2020 is proposed. This is realized by combining tracking, an electromagnetic and a hadronic calorimeter.

The current design of the Forward Calorimeter System (FCS) is a follow up development of the original proposed FCS system and is driven by detector performance, integration into STAR and cost optimization. The FCS consist of the refurbished PHENIX sampling ECal. The hadronic calorimeter will be a sandwich iron scintillator plate sampling type, based on the extensive STAR Forward Upgrade and EIC Calorimeter Consortium R&D. Both calorimeters will share the same cost-effective readout electronics, with SiPMs as photo-sensors. The proposed FCS system will have very good ($\sim 8\%/\sqrt{(E)}$) electromagnetic and ($\sim 50\%/\sqrt{(E)} \oplus 10\%$) hadronic energy resolutions. It can operate without shielding in a magnetic field and in a high radiation environment. In addition, the FCS will utilize the existing Forward Preshower Detector ($2.5 < \eta < 4$) successfully operated in STAR since 2015. By design the system is scalable and easily re-configurable. Integration into STAR will require minimal modification of existing infrastructure.

In addition to the FCS, a Forward Tracking System (FTS) is also proposed. The FTS must be capable of discriminating hadron charge sign for transverse asymmetry studies and separating electrons and positrons for Drell-Yan measurements. In heavy ion collisions, it should be able to measure transverse momentum of charged particles in the range of $0.2 < p_T < 2$ GeV/c with 20-30% momentum resolution. In order to keep multiple scattering and photon conversion background under control, the material budget of the FTS has to be small.

We propose a FTS-system combining 3 Silicon mini-strip disks together with 4 Small-Strip Thin Gap Chamber (sTGC) wheels ala ATLAS [4,5]. The Si mini-strip disks will be placed in the region z=140-187 cm. The 4 sTGC wheels would be placed 30 cm apart starting from z=273 cm. The sTGCs would also be extremely interesting as a cost-effective alternative tracking detector technology to the planned GEM-trackers in the forward arms of the current EIC detector designs.

All projections and physics discussions are based on the following already planned data taking periods during the sPHENIX running periods in starting in 2023:

1. **2023/2025:** 20 and 24 weeks of Au+Au at $\sqrt{s}$ = 200 GeV
2. **2024:** 24 weeks of polarized pp and pA at $\sqrt{s}$ = 200 GeV

In addition, a 20 week $\sqrt{s}$ = 500 GeV polarized p+p run, split between transverse and longitudinal polarized running is proposed based on its merits for the overall physics program laid out in this document. This run could be scheduled in end of FY2021 and extend to the 1st quarter of FY22, for which currently no dedicated physics program is assigned. It is especially noted none of the data taking periods proposed would result in any extra time delay to an eRHIC construction. **It is also noted that this high impact and cost-effective physics program can be executed even in challenging financial times.**

The Proposal is structured as following, in Section 2 we describe in detail how new data from (un)polarized p+p and p+A collisions at RHIC will serve as a gateway to the physics program at a future EIC (for further details please also see [6]). Section 0 details the simulation of the forward upgrade and its performance, and Section 0 and 0 describe the detailed design of the FCS and FTS.

The proposed program builds on the particular and unique strength of the RHIC accelerator facility compared to JLab, Compass and the LHC in terms of its versatility (i.e., the option of running with arbitrary nuclei), the availability of polarized proton beams, and wide kinematic coverage, further enhanced through an upgrade, consisting of electromagnetic and hadronic calorimetry as well as tracking, at forward rapidities at STAR The program will bring to fruition the long-term campaign of STAR@RHIC on Cold QCD, with its recent achievements summarized in [7,2]. **It is especially stressed** that the final experimental accuracy achieved will enable quantitative tests of process dependence, factorization and universality by comparing lepton-proton with proton-proton collisions, providing critical checks of our understanding of QCD dynamics.

2 The Physics of the Forward Upgrade

2.1 Transverse Polarization Effects in the Proton: Twist-3 and TMDs

The study of spin phenomena in nuclear and particle physics has a long history of producing important and often surprising results. Attempts to understand such data have pushed the field forward, forcing the development of both new theoretical frameworks and new experimental techniques. The detector system proposed here, coupled with the versatility of RHIC, will allow us to gain new insights into long-standing puzzles, and to probe more deeply the complexities of emergent behavior in QCD.

Results from PHENIX and STAR have shown that large transverse single spin asymmetries (SSA) for inclusive hadron production, A_N, that were first seen in p+p collisions at fixed-target energies and modest p_T extend to the highest RHIC center-of-mass energies, $\sqrt{s}$ = 500 GeV, and surprisingly large p_T. Figure 2-1 summarizes the world data as a function of Feynman-x. The asymmetries are nearly independent of $\sqrt{s}$ over a very wide range ($\sqrt{s}$: 4.9 GeV to 500 GeV).

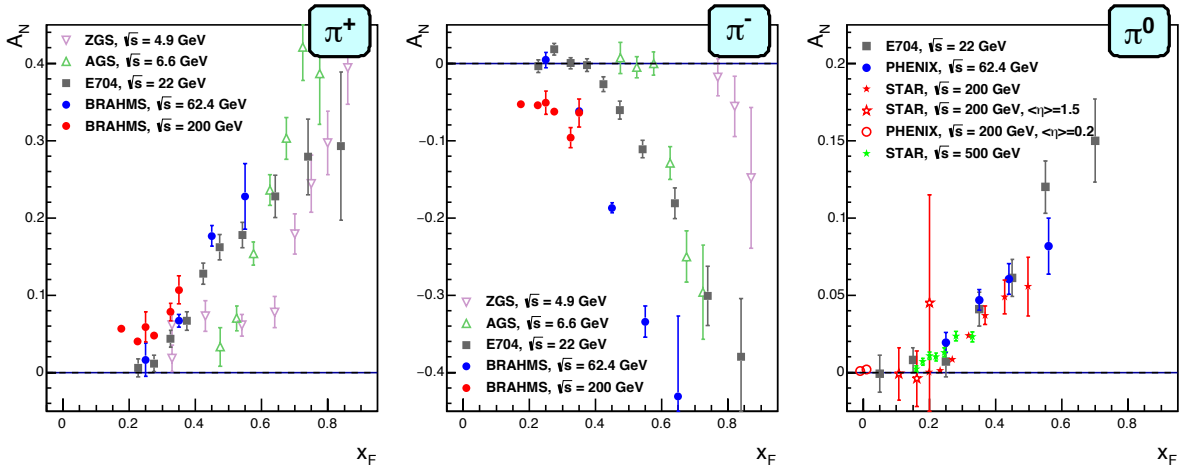

Figure 2-1: Transverse single spin asymmetry measurements for charged and neutral pions at different center-of-mass energies as a function of Feynman-x.

To understand the observed SSAs one has to go beyond the conventional leading twist collinear parton picture in the hard processes. Two theoretical formalisms have been proposed to explain sizable SSAs in the QCD framework: Transverse momentum dependent parton distributions and fragmentation functions, such as the Sivers and Collins functions, and transverse-momentum integrated (collinear) quark-gluon-quark correlations, which are twist-3 distributions in the initial state proton or in the fragmentation process. For many spin asymmetries, several of these functions can contribute and need to be disentangled to understand the experimental observations in detail, in particular the dependence on measured p_T. The functions express a spin dependence either in the initial state, for example the Sivers distribution and its Twist-3 analog, the Efremov-Teryaev-Qui-Sterman (ETQS) function [8], or in the final state via the fragmentation of polarized quarks, for example the Collins function.

The latest attempt to explain A_N for π^0 production at RHIC incorporated the fragmentation term within the collinear twist-3 approach [9]. In that work, the relevant (non-pole) 3-parton collinear fragmentation function $\widehat{H}_{FU}^{\Im}(z, z_z)$ was fit to the RHIC data. The so-called soft-gluon pole term, involving the ETQS function $T_{q,F}(x_1,x_2)$, was also included by fixing $T_{q,F}$ through its well-known relation to the TMD Sivers function $f_{1T}^{\perp}$. The authors found a very good description of the data due to the inclusion of $\widehat{H}_{FU}^{\Im}(z, z_z)$. Based on this work, one is able to make predictions for π^+ and π^- production at forward rapidities covered by the forward upgrade. The results are shown in Figure 2-2 for $\sqrt{s}$ = 200 GeV and 500 GeV and rapidity ranges ($2 < \eta < 3$ and $3 < \eta < 4$).

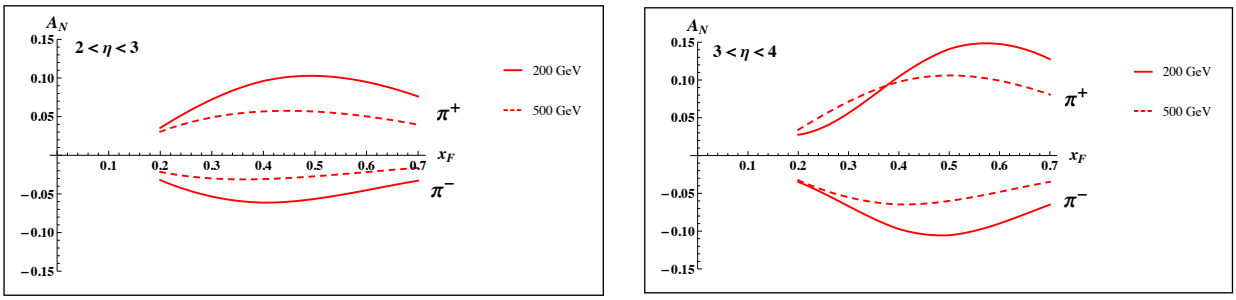

Figure 2-2: A_N predictions, based on the work in Ref. [9], for π^+ and π^- production for $2 < \eta < 3$ (left) and $3 < \eta < 4$ (right) at $\sqrt{s}$ = 200 GeV (solid lines) and $\sqrt{s}$ = 500 GeV (dashed lines). The $\sqrt{s}$ = 200 GeV BRAHMS A_N data for charged pions cover up to x_F of 0.3.

The proposed forward upgrade, incorporating forward tracking, will enable us to access the previously measured charged hadron asymmetries [10] up to the highest center-of-mass energies at RHIC. It will be important to confirm that the charged hadron asymmetries are independent of center-of-mass energy. The measurement of A_N for charged hadrons together with the data from Run-2015 and 2017 on direct photons A_N and π^0 should provide the best data set in the world to:

- Constrain the flavor dependence of the twist-3 ETQS distribution
- Constrain the evolution of the twist-3 ETQS distribution functions experimentally
- Determine if the 3-parton collinear fragmentation function $\widehat{H}^{\Im}_{FU}(z, z_z)$ is the main driver for the large forward A_N

Equally interesting is the opportunity to test the relation of the ETQS correlation functions and the Sivers function by measuring A_N for direct photon production and A_N for forward jet production. As discussed above, both the Sivers and the ETQS functions encapsulate partonic spin correlations inside the proton, but they are formally defined in different frameworks. The Sivers function is a TMD and the ETQS function is a twist three collinear distribution. Because both functions access essentially the same physics the Sivers function, $f_{1T}^{\perp}$, may be related to the ETQS functions, $T_{q,F}$, through an integral over transverse momentum:

$$T_{q,F}(x,x) = -\int d^2k_\perp \frac{|k_\perp|^2}{M} f_{1T}^{\perp q}(x, k_\perp^2)|_{SIDIS}$$

In contrast to the large pion asymmetries observed in the forward direction, inclusive jet asymmetries reported by the ANDY collaboration [11] in the same kinematic regime are small. An analysis by L. Gamberg et al. [12] argues these small asymmetries are due to cancelations between the *u* and *d* valence quark distributions. This idea is supported by the *u* and *d* Sivers functions extracted from SIDIS data have opposite sign but equal magnitude. Likewise, the twist-3 ETQS functions extracted from the Sivers functions using the integral relationship above, follow a similar pattern and fit the observed inclusive jet data well.

To better quantitatively test the relation between the two regimes, jet asymmetries which are *intentionally* biased towards either up or down quark jets with the help of a high-*z* charged hadron should be studied. In higher twist calculations of the jet asymmetries based on the Sivers function [13], sizeable asymmetries for the enhanced jet samples are predicted. This is experimentally accessible in forward jet reconstruction by tagging an additional charged hadron in the jet. Using realistic jet smearing in a forward calorimeter and tracking system and requiring a charged hadron with $z > 0.5$, the asymmetries can clearly be separated and compared to the predictions for the Sivers function based on the SIDIS data. The expected uncertainties plotted at the predicted values can be seen in Figure 2-3. Dilutions by underlying event and beam remnants were taken into account. The simulations have assumed an integrated luminosity of only 100 pb^{-1} at $\sqrt{s}$ = 200 GeV, which is

significantly lower than what is currently expected for a 200 GeV polarized p-p run in 2024. The same measurement is possible at 500 GeV.

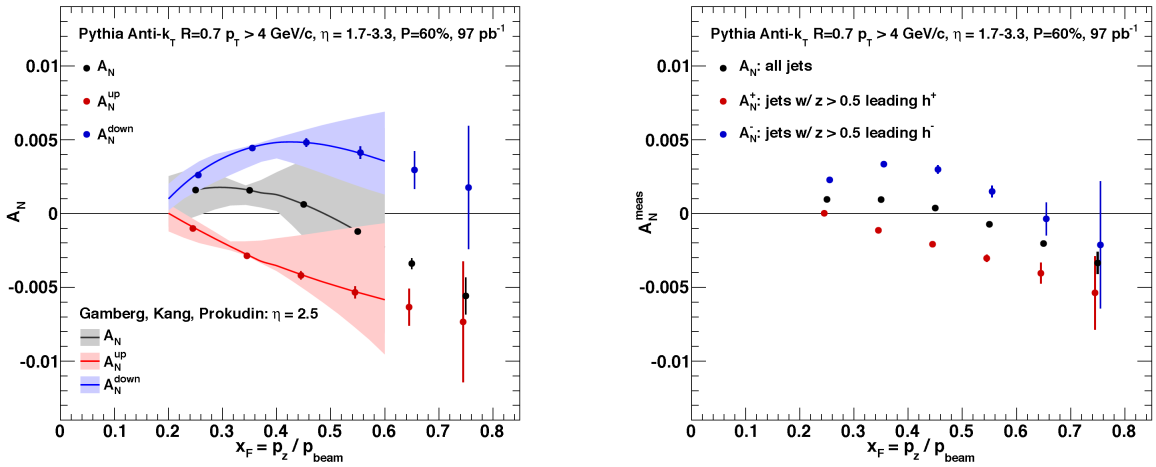

Figure 2-3: Left: up quark (red points), down quark (blue points) and all jet (black points) single spin asymmetries as a function of x_f as calculated by the ETQS based on the SIDIS Sivers functions. Right: Expected experimental sensitivities for jet asymmetries tagging in addition a positive hadron with z above 0.5 (red points), a negative hadron with z above 0.5 (blue points) or all jets (black) as a function of x_f. Note: these figures are currently for 200 GeV center-of-mass energy proton collisions – the 500 GeV results are expected to be qualitatively similar but with reduced uncertainties due to the larger luminosities expected.

2.2 Transversity, Collins and Interference Fragmentation Functions

A complete picture of nucleon spin structure at leading twist requires not only unpolarized and helicity distributions, but also those involving transverse polarization, such as the transversity distribution [14, 15, 16]. The transversity distribution can be interpreted as the net transverse polarization of quarks within a transversely polarized proton [15]. It is noted that the difference between the helicity distributions and the transversity distributions for quarks and antiquarks provides a direct, x-dependent, connection of nonzero orbital angular momentum components in the wave function of the proton [17]. Recently, the measurement of transversity has received renewed interest in an effort to access the so-called tensor charge of the nucleon, defined as the integral over the valence quark transversity: $\delta q^a = \int_0^1 [\,\delta q^a(x) - \delta \bar{q}^a(x)]\, dx$ [15,18]. Measuring the tensor charge is very important for two reasons: It can be calculated on the lattice with comparatively high precision, and due to the valence nature of transversity, it is one of the few quantities that allow us to compare experimental results on the spin structure of the nucleon to ab-initio QCD calculations. The second reason is that the tensor charge describes the sensitivity of observables in low energy hadronic reactions to beyond the standard model (BSM) physics processes with tensor couplings to hadrons. Examples are experiments with ultra-cold neutrons and nuclei [19].

Transversity is difficult to access due to its chiral-odd nature, requiring the coupling of this distribution to another chiral-odd distribution. SIDIS experiments have successfully probed transversity through two channels: asymmetric distributions of single pions, coupling transversity to the transverse-momentum-dependent (TMD) Collins fragmentation function [20], and azimuthally asymmetric distributions of di-hadrons, coupling transversity to the so-called "interference fragmentation function" (IFF) [21] in the framework of collinear factorization. Taking advantage of universality and robust proofs of TMD factorization for SIDIS, recent results [22,23,24,25] have been combined with e^+e^- measurements [26,27] isolating the Collins and IFFs for the first global analyses to extract simultaneously the transversity distribution and polarized FF [28, 29]. In spite of this wealth of data, the kinematic reach of existing SIDIS experiments, where

the range of Bjorken-x values does not extend above $x \sim 0.3$, limits the current extractions of transversity.

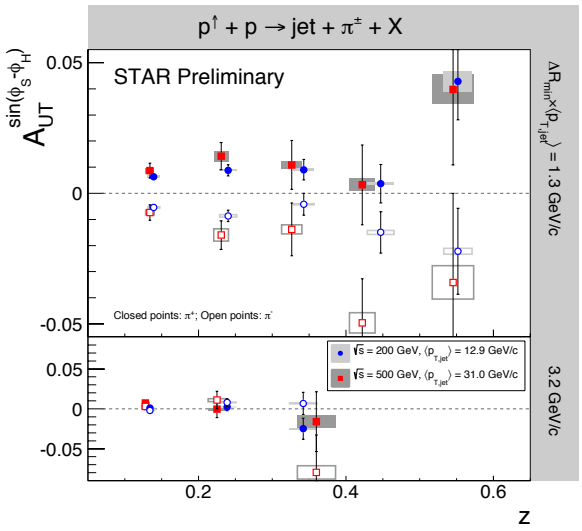

Figure 2-4: $A_{UT}^{\sin(\phi_S-\phi_h)}$ vs. z for charged pions in jets at $0 < \eta < 1$ from p+p collisions at $\sqrt{s} = 200$ GeV and 500 GeV by STAR. The $p_{T,jet}$ ranges have been chosen to sample the same parton x values for both beam energies. The angular cuts, characterized by the minimum distance of the charged pion from the jet thrust axis, have been chosen to sample the same j_T–values ($j_T \sim z \times \Delta R \times p_{T,jet}$). These data show for the first time a nonzero asymmetry in p+p collisions sensitive to transversity x Collins FF.

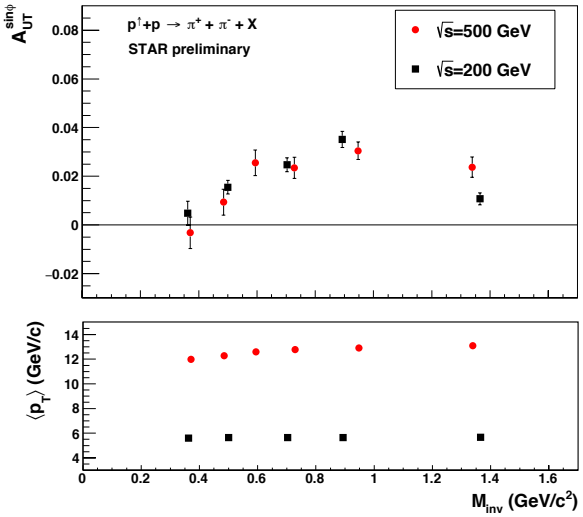

Figure 2-5: $A_{UT}^{\sin(\phi)}$ as a function of $M_{\pi+\pi-}$ (upper panel) and corresponding $p_{T(\pi+\pi-)}$ (lower panel). A clear enhancement of the signal around the ρ-mass region is observed both at $\sqrt{s} = 200$ GeV and 500 GeV by STAR for $-1 < \eta < 1$. The $p_{T(\pi+\pi-)}$ was chosen to sample the same x_T for $\sqrt{s} = 200$ GeV and 500 GeV.

Following the decomposition as described in [30,31,32] the Collins effect times the quark transversity distribution and the IFF times the quark transversity distribution may be accessed in polarized proton-proton collisions through single spin asymmetries of the azimuthal distributions of hadrons inside a high-energy jet [33] and the azimuthal asymmetries of pion pairs with different charges [34,35], respectively. Figure 2-4 and Figure 2-5 show the sizeable asymmetries measured with the STAR detector for the mid-rapidity Collins and IFF channels. A comparison of the transversity signals extracted from the two observables will explore questions about universality and factorization breaking, while comparisons of the same channel at 200 and 500 GeV will provide experimental constraints on evolution effects. The first extraction of transversity utilizing STAR 200 GeV IFF data from the 2006 RHIC run [35] has been performed recently [36]. While that global analysis was being finalized, STAR published the first measurements of IFFs in 500 GeV *pp* data [34]. These additional 500 GeV results will be included in the next generation global analysis.

By accessing the Collins asymmetry through the distribution of pions within a jet, one may also extract the k_T dependence of transversity, giving insight into the multidimensional dependence of the distribution. Following the decomposition described in Ref. [31], that shows how to correlate different angular modulations to different TMDs, STAR has extracted several other angular modulations [33]. One example is the Collins-like asymmetry $A_{UT}^{\sin(\phi_S-2\phi_h)}$. Currently all existing model predictions are unconstrained by measurements and suggest a maximum possible upper limit of ~2%. The present data fall well below this maximum with the best precision at lower values of z, where models suggest the largest effects may occur. Thus, these data should allow for the first phenomenological constraint on model predictions utilizing linearly polarized gluons beyond the positivity bounds.

While the measurements of transversity through the Collins FF need TMD factorization to hold in p+p scattering, di-hadron asymmetries utilize collinear factorization. Thus, not only can more precise measurements of these effects in p+p improve our knowledge of transversity, such measurements are invaluable to test the longstanding theoretical questions, such as the magnitude of any existing TMD factorization breaking. Extractions at RHIC kinematics also allow the possibility for understanding the TMD evolution of the Collins FF (e.g. Ref. [37]) by comparing to those extractions from SIDIS and e^+e^- data. As noted earlier, extending measurements of di-hadron and Collins asymmetries in the forward direction will allow access to transversity in the region x > 0.3, which is not probed by current experiments. This valence quark region is essential for the determination of the tensor charge, which receives 70% of its contributions from $0.1 < x < 1.0$, for details on the current status of the tensor charge please see [38] In addition, probing transversity in p+p collision provides enhanced sensitivity to the d-quark transversity compared to SIDIS, due to the fact that there is no charge weighting in the hard scattering QCD 2→2 process in p+p collisions. We note that this is a fundamental advantage of p+p collisions, as any SIDIS measurement of the d-quark transversity has to be on a bound system, i.e. He-3, which leads to nuclear corrections. The high scale we can reach in 500 GeV collisions at RHIC will also allow for the verification that previous SIDIS measurements at low scales are, in fact, accessing the nucleon at leading twist. Figure 2-6 shows the x-Q^2 coverage spanned by the RHIC measurements compared to a future EIC, JLab-12, and the current SIDIS world data.

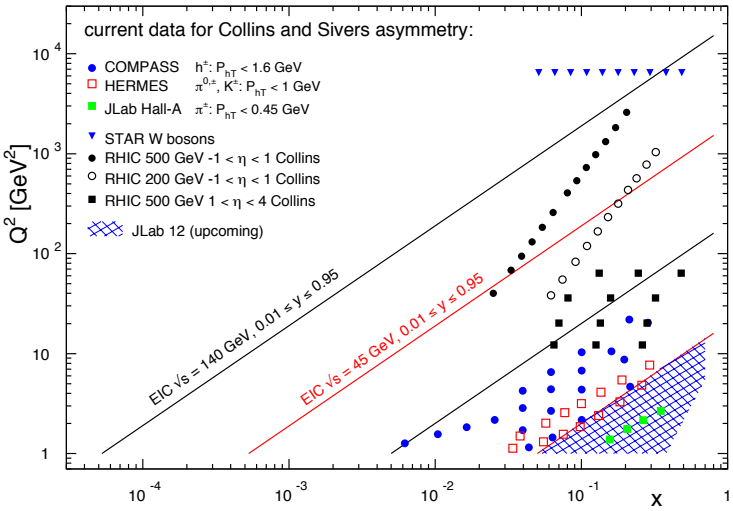

Figure 2-6: The x-Q^2 plane for data from the future EIC and Jlab-12 GeV as well as the current SIDIS data and the W-boson data from RHIC. All data are sensitive to the Sivers function and transversity times the Collins FF in the TMD formalism.

Another fundamental advantage of p+p collisions is the ability to access gluons directly. While gluons cannot carry any transverse spin, there is a strong analogy between quark transversity and the linear polarization of gluons. Similarly, there exists an equivalent of the Collins fragmentation function for the fragmentation of linearly polarized gluons into unpolarized hadrons [39]. The linear polarization of gluons is a largely unexplored phenomenon, but it has been a focus of recent theoretical work, in particular due to the relevance of linearly polarized gluons in unpolarized hadrons for the pT spectrum of the Higgs boson measured at the LHC. Polarized proton collisions at $\sqrt{s}$ = 500 GeV at RHIC are an ideal place to study the linearly polarized gluon distribution in polarized protons, especially for asymmetric partonic collisions in which the jets are detected in the backward direction. (Note: that the distributions of linearly polarized gluons inside an unpolarized and a polarized proton provide independent information). A first measurement of the "Collins-like" effect for linearly polarized gluons has been done by STAR with data from Run-2011, providing constraints on this function for the first time [33].

2.2.1 Opportunities with a Future Run at 500 GeV

In order to further advance our understanding of transverse momentum dependent effects it is critical to enhance the current kinematical reach to lower or higher *x*. This can only be realized by either going to substantially higher jet transverse momenta or by measuring jets at forward rapidities where more asymmetric collisions allow larger *x* and larger quark contributions in the hard process or to go to lower *x* and tag on gluon contributions in the hard scattering. The current RHIC plan does not include collisions above $\sqrt{s}$ = 200 GeV in the years after 2020. **If the timeline should change, making additional running in 2021 feasible**, proton-proton collisions at $\sqrt{s}$= 500 GeV, combined with forward rapidity coverage between 2.5 and 4, would allow RHIC to extend the currently accessed coverage in *x* substantially above 0.3 for reasonably high scales, as well as quantitatively test universality in the *x* range below, which is overlapping the range accessed in SIDIS experiments. On the other end of the partonic momentum spectrum, which is important for the study of linearly polarized gluons, *x* values below 2 x 10^{-3} can be reached.

To estimate the physics impact of a possible run at $\sqrt{s}$=500 GeV, we have done careful simulations of the uncertainties one might expect for some of the transverse asymmetries discussed above. A realistic momentum smearing of final state hadrons as well as jets in this rapidity range was assumed and dilutions due to beam remnants (which become substantial at high rapidities) and underlying event contributions have been taken into account. As currently no dedicated particle identification at forward rapidities is feasible for these measurements, only charged hadrons were taken into account that mostly reduces the expected asymmetries due to dilution by protons (10-14%) and a moderate amount of kaons (12-13%). As antiprotons are suppressed compared to protons in the beam remnants, the negative hadrons in particular can be considered a good proxy for negative pions (~78% purity according to PYTHIA6). Given their sensitivity to the down quark transversity via favored fragmentation, they are of particular importance because SIDIS measurements are naturally dominated by up-quarks due to their electromagnetic interaction.

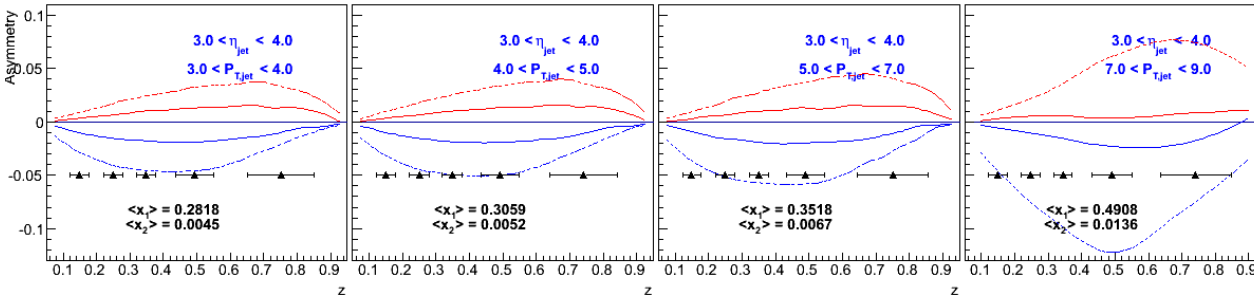

Figure 2-7: Expected h- Collins asymmetry uncertainties (black points) from a sampled luminosity of 268 pb-1 compared to positive (red) and negative (blue) pion asymmetries based on the Torino extraction [40] (full lines) and the Soffer bound [41] (dashed lines) as a function of fractional energy z for various bins in jet rapidity and transverse momentum.

We have estimated our statistical uncertainties based on a sampled luminosity of 268 pb^{-1}, which leaves uncertainties nearly invisible after smearing. The uncertainties were evaluated in a very fine binning in jet transverse momentum, jet rapidity and the fractional energy z of the hadrons relative to the jet-p_T. These expected uncertainties are compared in Figure 2-7 to the asymmetries obtained from the transversity extractions based on SIDIS and Belle data [28] as well as from using the Soffer positivity bound for the transversity PDF [42]. More recent global fits [43] have slightly different central up and down quark transversity distributions, but due to the lack of any data for *x* > 0.3 the upper uncertainties are compatible with the Soffer bounds. As can be seen from the average partonic *x* probed in the hard two-to-two process, *x* is increasing with increasing jet transverse momentum as well as rapidity. As discussed earlier it is this high-*x* coverage that provides critical sensitivity into the tensor charge. It is important to emphasize that even though the studies presented

here are for the Collins asymmetries, the resulting statistical uncertainties will be similar for other measurements using azimuthal correlations of hadrons in jets. One important example is the measurement of "Collins-like" asymmetries to access the distribution of linearly polarized gluons. As described earlier, the best kinematic region to access this distribution is at backward angles with respect to the polarized proton and at small jet p_T. With the instrumentation assumed for the forward Collins asymmetry studies, therefore a high precision measurement of the distribution of linearly polarized gluons can be performed as well.

Finally, it is worthwhile to note that a transversely polarized 500 GeV p+p run with anticipated delivered luminosity of 1 fb^{-1} will reduce by a factor of two the statistical uncertainties of all the TMD and twist-3 observables that motived the current RHIC Run 17, including A_N of $W^{+/-}$, Z^0, direct γ and Drell-Yan pairs. This experimental accuracy will significantly enhance the quantitative reach of testing the limits of factorization and universality in lepton-proton and proton-proton collisions.

2.3 Using Dijets to access ΔG at √s = 500 GeV

Additional longitudinally polarized proton-proton collisions at √s = 500 GeV would allow RHIC to explore the low x region of the gluon helicity distribution $\Delta g(x)$. A future 500 GeV longitudinal polarized p+p run (8 weeks with a delivered integrated luminosity of 1.1 fb^{-1}) would further reduce the statistical uncertainties of the two workhorses of the RHIC Δg program, inclusive mid-rapidity jets and neutral pions, by a factor of 1.25 compared to the existing data sets shown in Figure 2-8 and Figure 2-9.

The existing mid-rapidity analyses are sensitive to gluons in the range of $0.01 < x < 1$. While these measurements clearly point to a positive $\Delta g(x)$ for moderate x values, they do little to constrain the functional form of the distribution at lower x. This lack of data translates directly into a large uncertainty on the total gluon contribution to the spin of the proton $\Delta G = \int_0^1 \Delta g(x, Q^2) dx$, as shown in Figure 2-10. Di-jet measurements provide a more direct connection to the probed values of momentum fractions x, and if extended to forward region, allow us to access x down to 10^{-3}. Figure 2-11 shows the projected precision for the asymmetries A_{LL} as a function of the scaled invariant di-jet mass $M_{inv}/\sqrt{s}$ for four topological di-jet configurations involving a generic forward calorimeter system (FCS) in combination with either $-1.0 < \eta < 0.0$, $0.0 < \eta < 1.0$, $1.0 < \eta < 2.0$, and the FCS ($2.5 < \eta < 4.0$). In particular the $1.0 < \eta < 2.0$ / FCS and FCS / FCS configurations would allow one to probe x values as low as a few times 10^{-3}, as shown Figure 2-12. The systematic uncertainty, which is assumed to be driven by the relative luminosity uncertainty of $\delta R = 5 \cdot 10^{-4}$, is clearly dominating over the statistical uncertainties. Any future measurements in these topological configurations, including very forward measurements, would clearly benefit from an improved relative luminosity measurement.

Di-jet measurements would provide theoretically well-controlled insight into the nature of the proton spin compared to the current forward rapidity ($2.8 < \eta < 4.0$) inclusive π^0 A_{LL}. Jet reconstruction in the region will require electromagnetic and hadronic calorimetry, as well as some nominal tracking to associate charged particles with a single vertex.
The STAR collaboration has already established di-jet double spin asymmetry A_{LL} measurements in the pseudorapidity range $-1 < \eta < 2$.

Figure 2-13 shows the published results for p+p collisions at √s = 200 GeV (blue) [44] and preliminary results for √s = 510 GeV (red) [45], based on data that were recorded in 2009 and 2012, respectively. Figure 2-14 shows the most recent STAR result for di-jets at √s = 200 GeV with both jets at more forward rapidities $0.8 < \eta_{1,2} < 1.8$ [46]. The impact of the measurements from 2009+2015 (√s = 200 GeV) and 2012 + 2013 (√s = 500 GeV) on the helicity gluon distribution is currently being assessed by the DSSV collaboration in the context of a global QCD analysis at next-to-leading order accuracy, which matches the experimental cuts and jet parameters

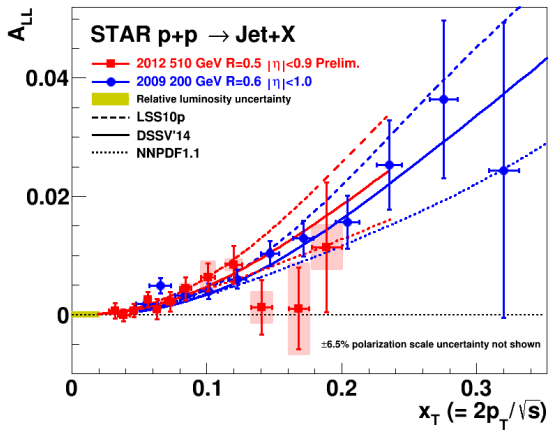

Figure 2-8: A_{LL} vs. x_T for inclusive jet production at mid-rapidity in 200 GeV (blue circles) [47] and 510 GeV (red squares) [48] p+p collisions, compared to NLO predictions [49,50] for three recent NLO global analyses [51,52,53] (blue curves for 200 GeV and red curves for 510 GeV).

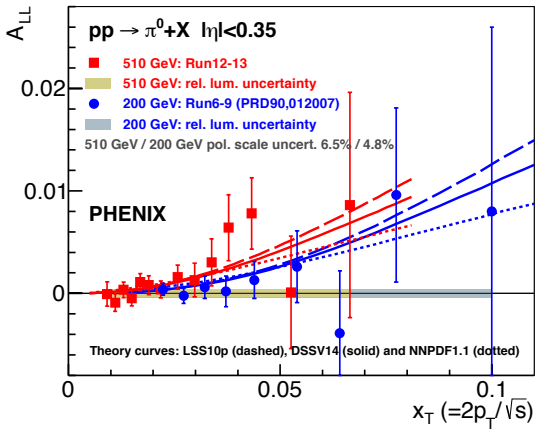

Figure 2-9: A_{LL} vs. x_T for π^0-meson production at mid rapidity with the point-to-point uncertainties in 200 GeV (blue circles) [54] and 510 GeV (red squares) [55] p+p collisions, compared to NLO predictions [56] for three recent NLO global analyses [51,52,53] (blue curves for 200 GeV and red curves for 510 GeV). The gray/gold bands give the correlated systematic uncertainties.

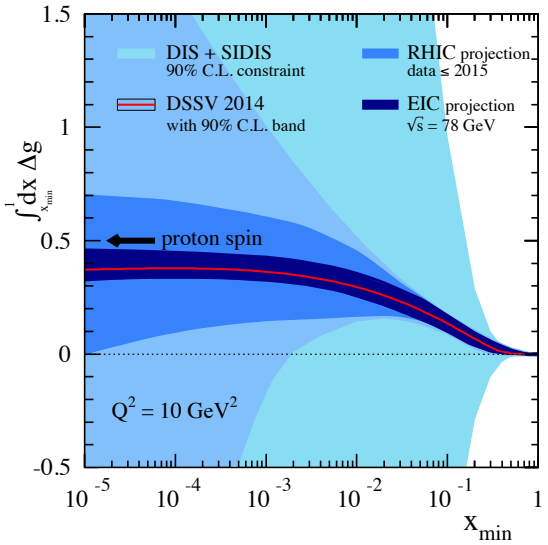

Figure 2-10: The running integral for Δg as a function of x_{min} at $Q^2 = 10$ GeV^2 as obtained in the DSSV global analysis framework. The different uncertainty bands at 90% C.L. are estimated from the world DIS and SIDIS data, with and without including the combined set of projected pseudo-data for preliminary and RHIC measurements up to Run-2015, respectively as well as including EIC DIS pseudo data (taken from Ref. [57]).

An EIC is anticipated to resolve the individual contributions to the spin of the nucleon with unprecedented precision in the x range down to a few times 10^{-5} [58,59]. Hence, RHIC mid- and forward-rapidity A_{LL} measurements would continue providing unique and compelling sensitivity to the gluon helicity distribution of the proton at higher x, but reaching to x-values, which might indicate if the low-x region makes a significant contribution to the spin of the proton and such informing the EIC community what the needed center-of-mass energy is to resolve the "spin-puzzle".

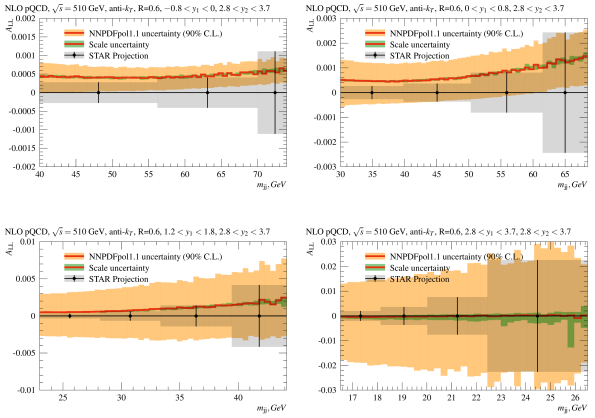

Figure 2-11: A_{LL} NLO calculations as a function of $M_{inv}/\sqrt{s}$ for $2.8 < \eta < 3.7$ together with projected statistical and systematic uncertainties. An uncertainty $5 \cdot 10^{-4}$ has been assumed for the systematic uncertainty due to relative luminosity. A beam polarization of 60% and a total delivered luminosity of 1 fb^{-1} have been assumed with a ratio of 2/3 for the ratio of recorded to delivered luminosity.

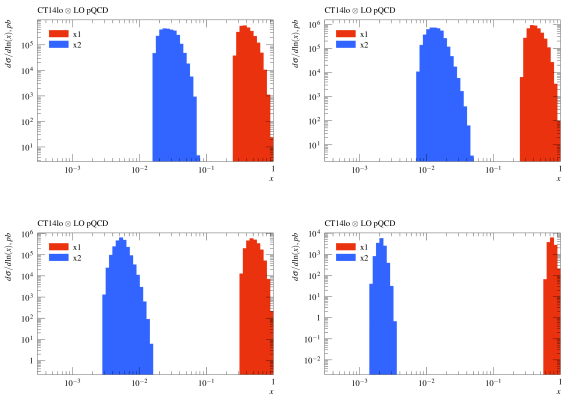

Figure 2-12: x_1/x_2 range for the forward acceptance region of $2.8 < \eta < 3.7$.

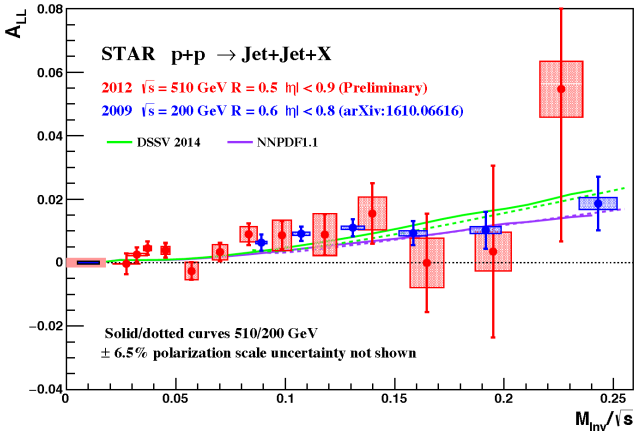

Figure 2-13: STAR measurements of the di-jet double spin asymmetry A_{LL} versus $Minv/\sqrt{s}$ of the pair for mid-rapidity p+p collisions at $\sqrt{s}$ = 200 GeV (blue) and $\sqrt{s}$ = 510 GeV (red), compared to model predictions based on DSSV14 and NNPDFpol1.1. The uncertainties will be reduced by a factor of approximately 1.7 after additional data recorded during 2013 (510 GeV) and 2015 (200 GeV) are included.

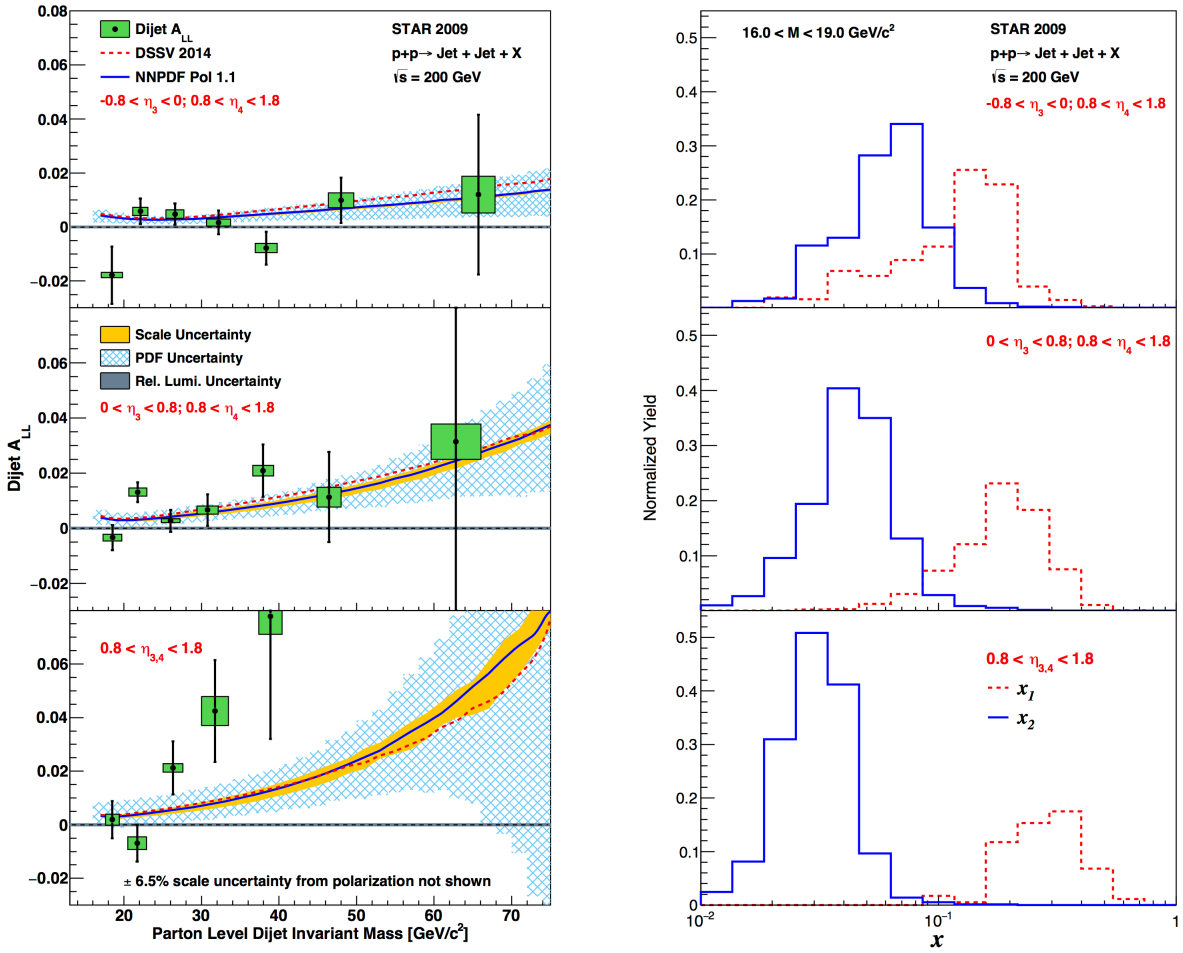

Figure 2-14: (left) STAR measurements of the di-jet double spin asymmetry A_{LL} versus *Minv* of the pair for mid-rapidity p+p collisions at $\sqrt{s}$ = 200 GeV with at least one jet in the rapidity range $0.8 < \eta_{1,2} < 1.8$ [updated 45], compared to model predictions based on DSSV14 and NNPDFpol1.1. (right) The corresponding x_1/x_2 ranges for the 3 different rapidity combinations of the di-jets.

2.4 Physics opportunities with (un)polarized proton-Nucleus collisions

Our quest to understand QCD processes in Cold Nuclear Matter (CNM) centers on the following fundamental questions:

- Can we experimentally find evidence of a novel universal regime of non-linear QCD dynamics in nuclei?
- What is the role of saturated strong gluon fields, and what are the degrees of freedom in this high gluon density regime?
- What is the fundamental quark-gluon structure of light and heavy nuclei?
- Can a nucleus, serving as a color filter, provide novel insight into the propagation, attenuation and hadronization of colored quarks and gluons?

Various aspects of these questions have been addressed by numerous experiments and facilities around the world, most of them at significantly lower center-of-mass energies and kinematic reach then RHIC. Deep inelastic scattering on nuclei addresses some of these questions with results from, for instance, HERMES at DESY [60], CLAS at JLab [61], and in the future at the JLab 12 GeV. This program is complemented by hadron-nucleus reactions in fixed target p+A at Fermilab (E772, E886, and E906) [62] and at the CERN-SPS.

In the following we propose a measurement program unique to RHIC to constrain the initial state effects in strong interactions in the nuclear environment. We also highlight the complementarity to the LHC p+Pb program and stress why RHIC data are essential and unique in the quest to further our understanding of nuclei. The uniqueness of the RHIC program is based on the flexibility of the RHIC accelerator to run collisions of different particle species at very different center-of-mass energies. This in combination with the existing and planned STAR detector capabilities allows to disentangle nuclear effects in the initial and final state as well as leading twist shadowing from saturation effects in a kinematic regime where all these effects are predicted to be large. The discussed measurements critically rely on the forward upgrade described in section 0.

2.4.1 The Initial State of Nuclear Collisions

Nuclear Parton Distribution Functions

A main emphasis of the 2015 and later p+A runs at RHIC is to determine the initial conditions of the heavy ion nucleus before the collision to support the theoretical understanding of the A+A program both at RHIC and the LHC. In the following, the current status of nPDFs will be discussed, including where the unique contribution of RHIC lie, in comparison to the LHC and a future EIC.

Our current understanding of nuclear parton distribution functions (nPDFs) is still very limited, in particular when compared with the rather precise knowledge of PDFs for free protons collected over the past 30 years. Figure 2-15 shows an extraction of nPDFs from available data, along with estimates of uncertainties. All results are shown in terms of the nuclear modification ratios, i.e., scaled by the respective PDF of the free proton. The yellow bands indicate regions in x where the fits are not constrained by data [63] and merely reflect the freedom in the functional form *assumed* in the different fits. Clearly, high precision data at small x and for various different values of Q^2 are needed to better constrain the magnitude of suppression in the x region where non-linear effects in the scale evolution are expected. In addition, such data are needed for several different nuclei, as the A-dependence of nPDFs cannot be predicted from first principles in pQCD and, again, currently relies on assumptions. Note that the difference between DSSZ [64] and EPS09 for the gluon modification arise from the different treatment of the PHENIX midrapidity π^0 R_{dAu} data [65], which in the EPS09 [66] fit are included with an extra weight of 20. The π^0 R_{dAu} data are the only data, which can probe the gluon in the nucleus directly, but these data also suffer from unknown nuclear effects in the final state (see Ref. [67]). Therefore, it is absolutely critical to have high precision data only sensitive to nuclear modification in the initial state over a wide range in x and intermediate values of Q^2, away from the saturation regime but where nuclear effects are still large, to establish the nuclear modification of gluons in this kinematic range.

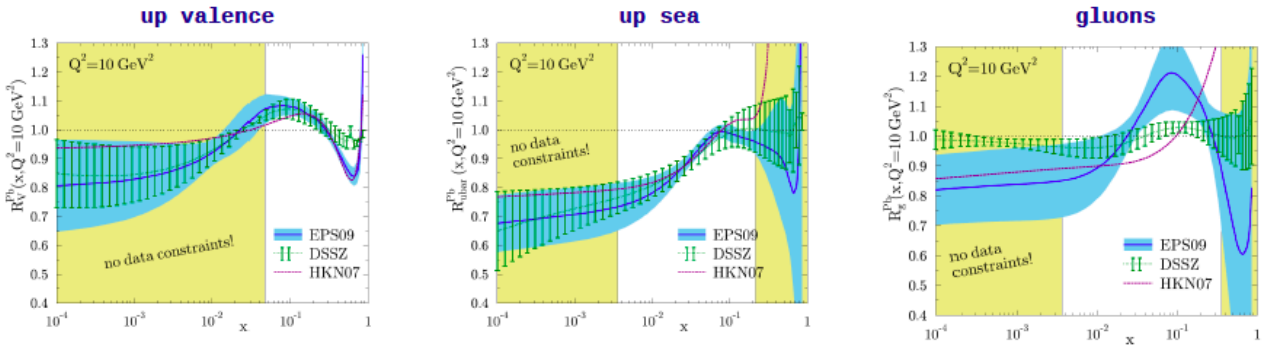

Figure 2-15: Summary of the most recent sets of nPDFs. The central values and their uncertainty estimates are given for the up valence quark, up sea quark, and the gluon. The yellow bands indicate regions in x where the fits are not constrained by any data (taken from Ref. [68]).

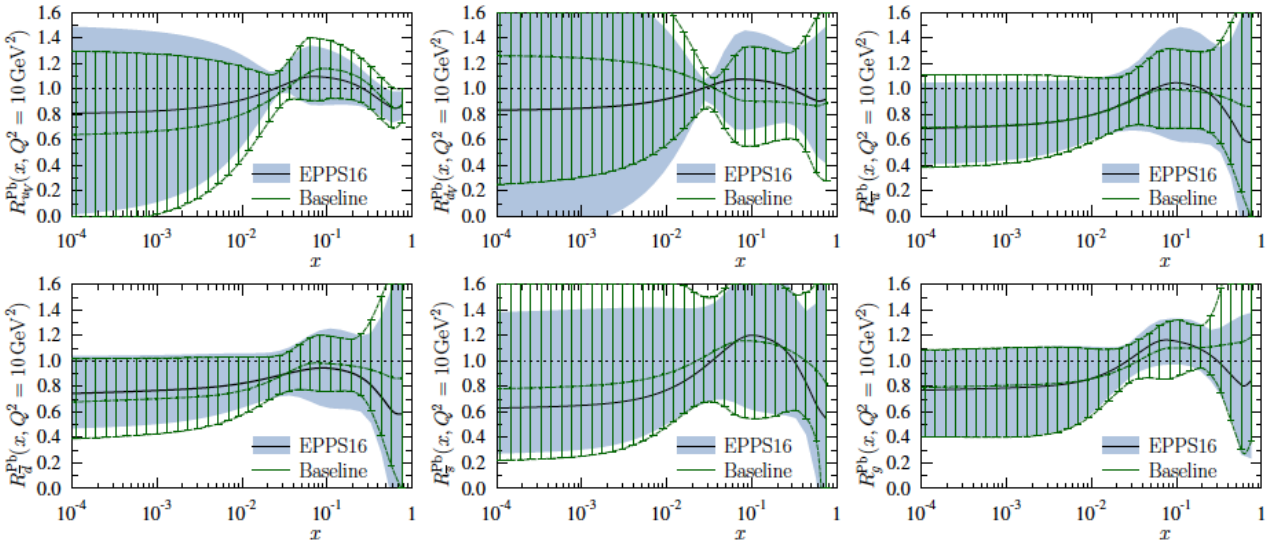

Figure 2-16: The nuclear modifications at Q^2=10GeV^2 from the EPPS-16 fit (black central line and light-blue bands) compared with the Baseline fit (green curves with hatching) which uses only the data included in the EPS09 fit.

It is important to realize that the measurements from RHIC are compelling and essential even when compared to what can be achieved in p+Pb collisions at the LHC. Due to the higher center-of-mass system energy, most of the LHC data have very high Q^2, where the nuclear effects are already reduced significantly by evolution and are therefore very difficult to constrain. A recent article [69] assessed the impact of the available LHC Run-I p+Pb data on determinations of nPDFs. The rather moderate impact of these data is illustrated in Figure 2-16. Note that the extra weight factor of 20 for the PHENIX midrapidity π^0 R_{dAu} data [70] in the original EPS09 [71] fit was removed in all of the new fits, leading to a much smaller nuclear modification factor for gluons, especially at medium to high x.

RHIC has the *unique* capability to provide data in a kinematic regime (moderate Q^2 and medium-to-low x) where the nuclear modification of the sea quark and the gluon is expected to be sizable and currently completely unconstrained. In addition, and unlike the LHC, RHIC can vary the nucleus in p+A collisions and as such also constrain the A-dependence of nPDFs.

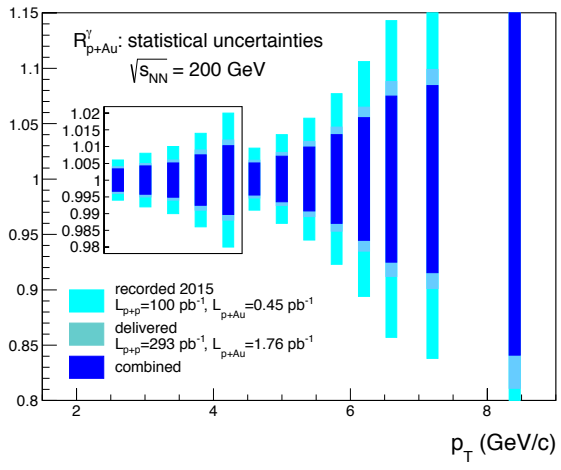

Figure 2-17: Projected statistical uncertainties for R_{pAu} for direct photons in Run-2015 (light blue) and a run in 2024 (blue) and the sum of both (dark blue). The recorded luminosity for Run-2015 was L_{pAu} = 450 nb^{-1} and L_{pp} = 100 pb^{-1}. The delivered luminosity for Run-2024 is assumed to be L_{pAu} = 1.8 pb^{-1} and L_{pp} = 300 pb^{-1}. A p+Al run of 8 weeks in 2024 would have matched parton luminosity resulting in an equal statistical precision.

Extraction of this information is less ambiguous if one uses processes in which strong (QCD) final-state interactions can be neglected or reduced. Such golden channels would include: a measurement of R_{pA} for Drell-Yan production at forward pseudo-rapidities with respect to the proton direction ($2.5 < \eta_{\square} < 4.$) to constrain the nuclear modifications of sea-quarks; and of R_{pA} for direct

photon production in the same kinematic regime to constrain the nuclear gluon distribution. The first measurement of R_{pA} for direct photon production has been done already during the p+Au and p+Al runs in 2015, with recorded luminosities by STAR of L_{pAu} = 0.45 pb^{-1} and L_{pAl} = 1 pb^{-1}, respectively. The anticipated statistical precision for pA runs in 2015 and projections for a run in 2024 are shown in Figure 2-17. The planned forward upgrade with its tracking at forward rapidities will also provide the possibility to measure R_{pA} for positive and negatively charged hadrons.

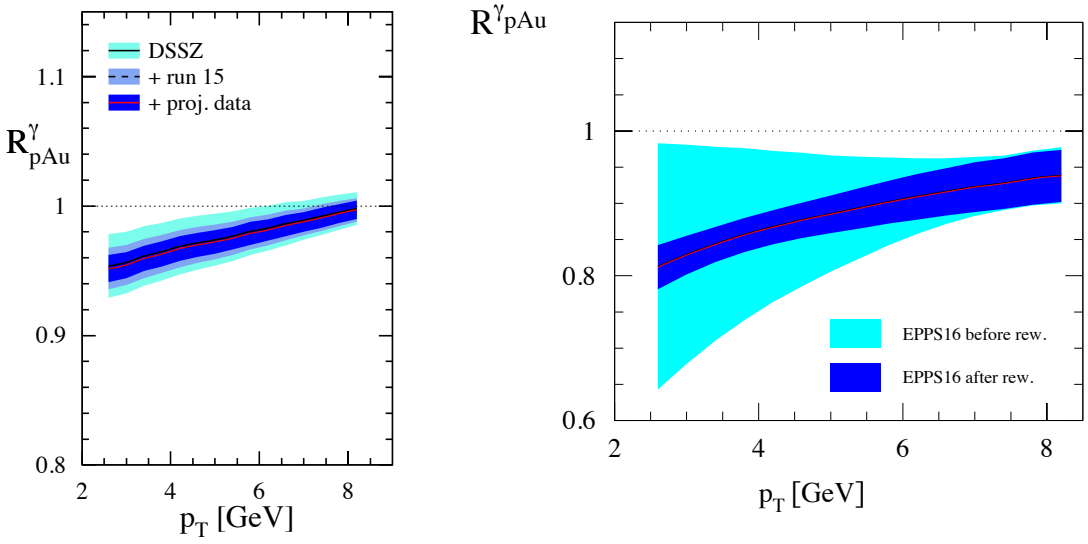

Figure 2-18: The impact of the direct photon R_{pA} data measured in Run-2015 (blue band) and for the anticipated statistics for a future p+Au run in 2024 (dark blue band) compared with the current uncertainties (cyan band) from DSSZ (left) and EPPS-16 (right).

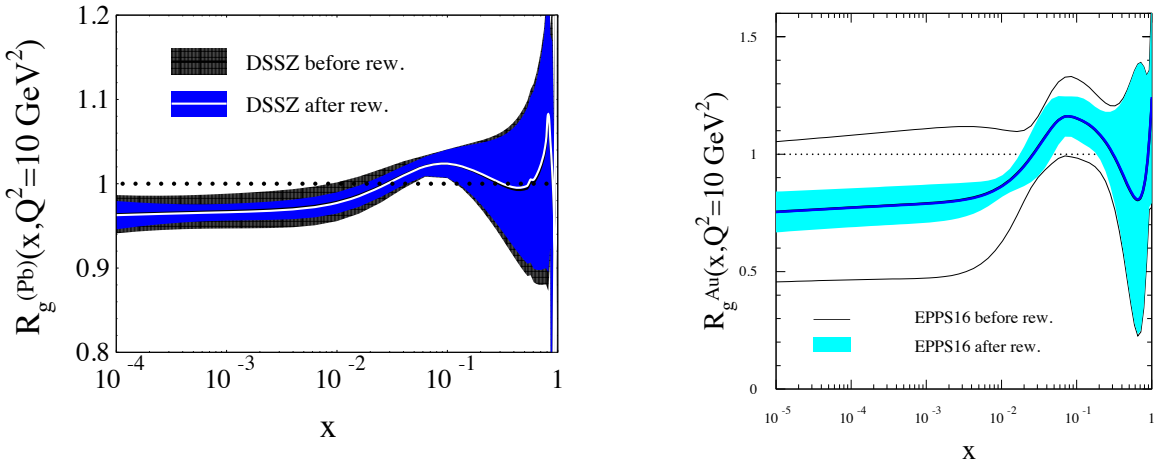

Figure 2-19: The impact of the direct photon R_{pA} data measured in Run-2015 and for the anticipated statistics for a future p+Au run in 2024 (blue band) on DSSZ (left) and (red band) EPPS-16 (right). The impact is shown on the nuclear suppression factor R_g of nPDF to the proton PDF, the grey bands represent the uncertainties before including the RHIC pseudo data.

Figure 2-18 shows the significant impact of the Run-2015 R_{pA} for direct photon production plus a future run in the 2024, on the corresponding theoretical expectations and their uncertainties obtained with both the EPPS-16 and DSSZ sets of nPDFs. The uncertainty bands are obtained through a reweighting procedure [72] by using the projected data shown in Figure 2-17 and randomizing them according to their expected statistical uncertainties around the central values obtained with the current

set of DSSZ and EPPS-16 nPDFs, respectively. Figure 2-19 shows how these measurements will help significantly in further constraining the nuclear gluon distribution in a broad range of x that is roughly correlated with accessible transverse momenta of the photon, i.e., few times $10^{-3} < x <$ few times 10^{-2}. The relevant scale Q^2 is set be $\sim p_T^2$ and ranges from 6 GeV^2 to about 40 GeV^2. Like all other inclusive probes in p+p and pA collisions, e.g., jets, no access to the exact parton kinematics can be provided event-by-event but global QCD analyses easily account for that. After the p+Au run in 2024, the statistical precision of the prompt photon data will be sufficient to contribute to a stringent test of the universality of nuclear PDFs when combined with the expected data from an EIC (see Figure 2.22 and 2.23 in Ref [73]).

Figure 2-20 shows the kinematic coverage in x–Q^2 of past, present, and future experiments capable of constraining nuclear parton distribution functions. The experiments shown provide measurements that access the initial state parton kinematics on an event-by event basis (in a leading order approximation) while remaining insensitive to any nuclear effects in the final state. Some of the LHC experiments cover the same x-range as DY at forward pseudo-rapidities at RHIC but at a much higher scale Q^2, where nuclear modifications are already significantly reduced [69, 74]. At intermediate Q^2, DY at RHIC will extend the low-x reach by nearly one decade compared to EIC.

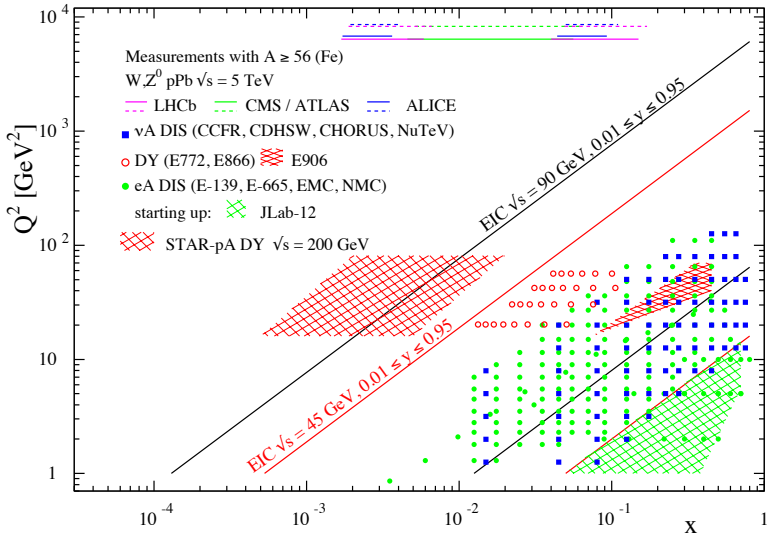

Figure 2-20: The kinematic coverage in x–Q^2 of past, present and future experiments constraining nPDFs with access to the exact parton kinematics event-by-event and no fragmentation in the final state.

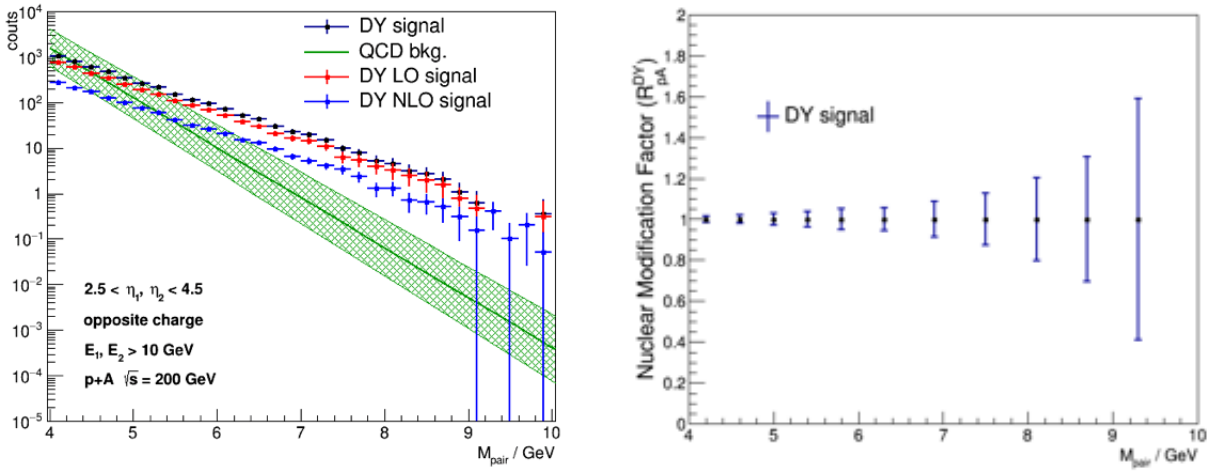

Figure 2-21: (left) DY signal and background yield from 2.3 pb^{-1} p+Au 200 GeV collisions. (right) The expected R_{pA} based on the 2.3 pb^{-1} p+Au and 383 pb^{-1} p+p reference data.

The biggest challenge of a DY measurement is to suppress the overwhelming hadronic background: the total DY cross-section is about 10^{-5} to 10^{-6} smaller than the corresponding hadron production cross-sections. Therefore, the probability of misidentifying a hadron track as a lepton has to be suppressed to the order of 0.1% while maintaining reasonable electron detection efficiencies. To that end, we have studied the combined electron/hadron discriminating power of the proposed forward tracking and calorimeter systems. It was found that by applying multivariate analysis techniques to the features of EM/hadronic shower development and momentum measurements we can achieve hadron rejection powers of 200 to 2000 for hadrons of 15 GeV to 50 GeV with 80% electron detection efficiency.

The left panel in Figure 2-21 shows the normalized background yields along with the expected DY production and their uncertainties for a delivered luminosity of 2.3 pb^{-1} and assuming the performance of the upgraded forward instrumentation as described in detail in Section 0 and 0. The green band represents the statistical uncertainties of the background yield and its shape. The right panel shows the statistical precision of the DY R_{pA} measurement as a function of the lepton pair mass.

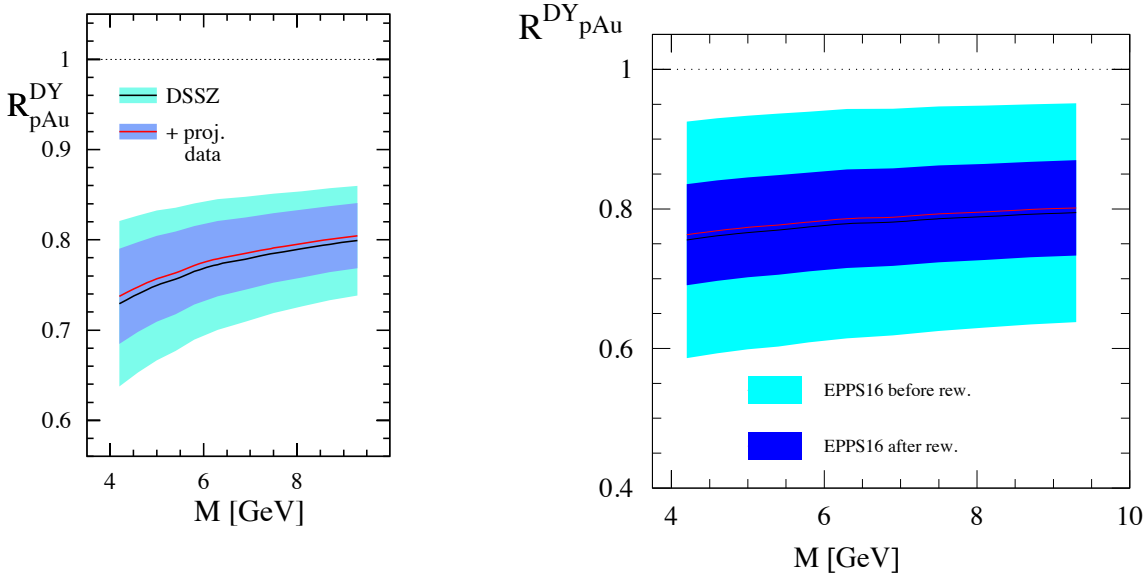

Figure 2-22: The impact of the DY R_{pA} data for the anticipated statistics for a p+Au run in 2024 (dark blue band) compared to the current uncertainties (cyan band) from DSSZ and EPPS-16.

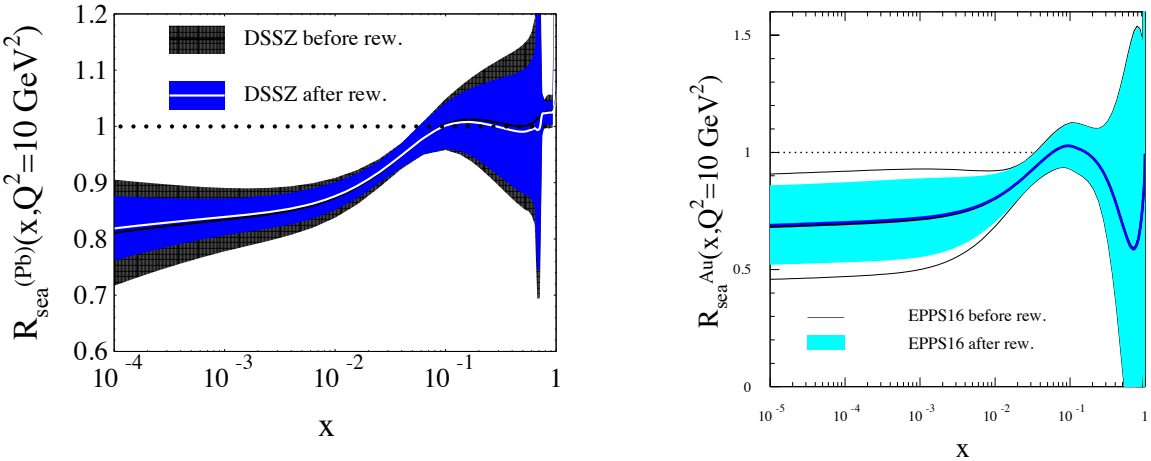

Figure 2-23: The impact for the anticipated statistics for the DY R_{pA} data for a future p+Au run in 2024 (blue band) on DSSZ (left) and (red band) EPPS-16 (right). The impact is shown on the nuclear suppression factor R_{ubar} of nPDF to the proton PDF, the grey bands represent the uncertainties before including the RHIC pseudo data.

The same procedure as for the direct photon R_{pA} was used to study the potential impact of the DY R_{pA} data. For the DSSZ and EPPS-16 sets of nPDFs both the predicted nuclear modifications and the current uncertainties are very similar. This is because both groups use the same DIS and DY data without any special weight factors in constraining sea-quarks. As can be inferred from Figure 2-21 we expect again a significant impact on the uncertainties of R_{pA} DY upon including the projected and properly randomized data (see Figure 2-22). Clearly, the DY data from RHIC will be instrumental in reducing present uncertainties in nuclear modifications of sea quarks (see Figure 2-23). Again, these data will prove to be essential in testing the fundamental universality property of nPDFs in the future when EIC data become available.

Gluon Saturation

Our understanding of the proton structure and of the nuclear interactions at high energy would be advanced significantly with the definitive discovery of the saturation regime [75]. Saturation physics would provide an infrared cutoff for perturbative calculations, the saturation scale Q_s, which grows with the atomic number of the nucleus A and with decreasing value of x. If Q_s is large it makes the strong coupling constant small, $\alpha_s(Q_s^2) << 1$ allowing for perturbative QCD calculations to be under theoretical control.

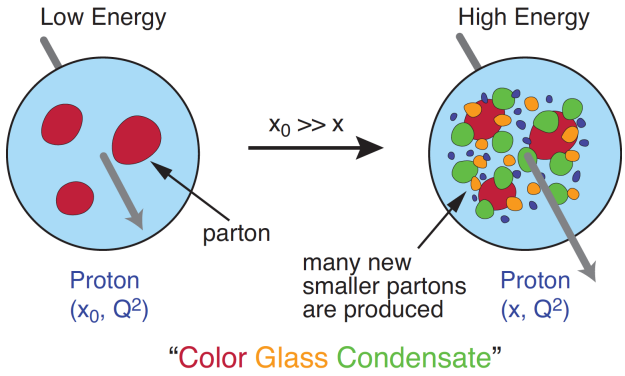

Figure 2-24: Proton wave function evolution towards small-x.

It is well known that PDFs grow at small-x. If one imagines how such a high number of small-x partons would fit in the (almost) unchanged proton radius, one arrives at the picture presented in Figure 2-24: the gluons and quarks are packed very tightly in the transverse plane. The typical distance between the partons decreases as the number of partons increases, and can get small at low-x (or for a large nucleus instead of the proton). One can define the saturation scale as the inverse of this typical transverse inter-parton distance. Hence Q_s indeed grows with A and decreasing x.

The actual calculations in saturation physics start with the classical gluon fields (as gluons dominate quarks at small-x) [76], which are then evolved using the nonlinear small-x BK/JIMWLK evolution equations [77]. The saturation region is depicted in Figure 2-25 in the (x,Q^2) plane and can be well-approximated by $Q_s^2 \sim (A/x)^{1/3}$. Note again that at small enough x the saturation scale provides an IR cutoff, justifying the use of perturbative calculations. This is important beyond saturation physics, and may help us better understand small-x evolution of the TMDs.

While evidence supporting saturation physics has been gleaned from the data collected at HERA, RHIC and the LHC, the case for saturation is not sealed and alternative explanations of these data exist. The EIC is slated to provide more definitive evidence for saturation physics [78]. To help the EIC complete the case for saturation, it is mandatory to generate higher-precision measurements in p+A collisions at RHIC. These higher-precision measurements would significantly enhance the discovery potential of the EIC as they would enable a stringent test of universality of saturation. We stress again that a lot of theoretical predictions and results in the earlier Sections of this document would greatly benefit from saturation physics: the small-x evolution of TMDs in a longitudinally or

transversely polarized proton, or in an unpolarized proton, can all be derived in the saturation framework [79] in a theoretically better-controlled way due to the presence of Q_s. Hence saturation physics may help us understand both the quark and gluon helicity PDFs as well as the Sivers and Boer-Mulders functions.

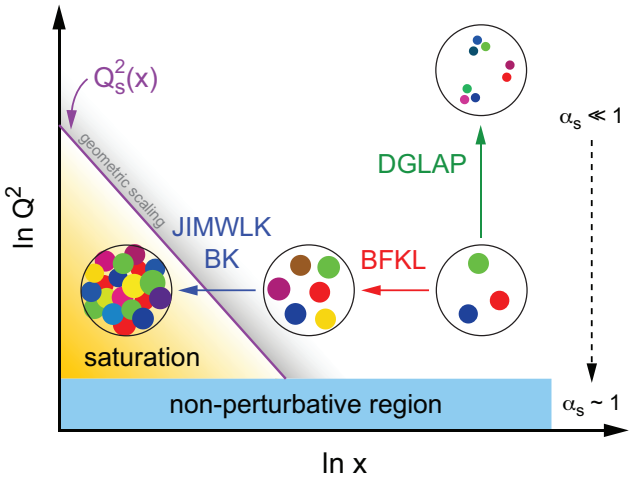

Figure 2-25: Saturation region in the (x,Q^2) plane.

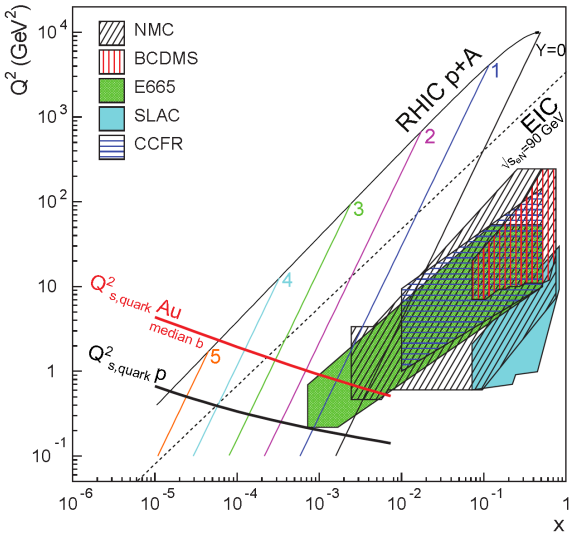

Figure 2-26: Kinematic coverage in the x-Q^2 plane for p+A collisions at RHIC, along with previous e+A measurements, the kinematic reach of an electron-ion collider, and estimates for the saturation scale Q_s in Au nuclei and protons. Lines are illustrative of the range in x and Q^2 covered with hadrons at various rapidities.

The saturation momentum is predicted to grow approximately like a power of energy, $Q_s^2 \sim E^{\lambda/2}$ with $\lambda \sim 0.2$-0.3, as phase space for small-x (quantum) evolution opens up. The saturation scale is also expected to grow in proportion to the valence charge density at the onset of small-x quantum evolution. Hence, the saturation scale of a large nucleus should exceed that of a nucleon by a factor of $A^{1/3} \sim 5$ (on average over impact parameters). RHIC is capable of running p+A collisions for different nuclei to check this dependence on the mass number. This avoids potential issues with dividing say p+Pb collisions in N_{part} classes [80]. Figure 2-26 shows the kinematic coverage in the x-Q^2 plane for p+A collisions at RHIC, along with previous e+A measurements and the kinematic reach of an EIC. The saturation scale for an Au nucleus and the proton is also shown. To access at RHIC a kinematic regime sensitive to saturation with $Q^2 > 1$ GeV^2 requires measurements at forward rapidities. For this kinematics the saturation scale is moderate, on the order of a few GeV^2, so measurements sensitive to the saturation scale are by necessity limited to semi-hard processes.

To date the golden channel at RHIC to observe strong hints of saturation has been the angular dependence of two-particle correlations, because it is an essential tool for testing the underlying QCD dynamics [81]. In forward-forward correlations facing the $p(d)$ beam direction one selects a large-x parton in the p(d) interacting with a low-x parton in the nucleus. For $x < 0.01$ the low-x parton will be back-scattered in the direction of the large-x parton. Due to the abundance of gluons at small x, the backwards-scattered partons are dominantly gluons, while the large-x partons from the p(d) are dominantly quarks. The measurements of di-hadron correlations by STAR and PHENIX [82,83] have been compared with theoretical expectations using the CGC framework based on a fixed saturation scale Q_s and considering valence quarks in the deuteron scattering off low-x gluons in the nucleus with impact parameter $b = 0$ [84,85]. Alternative calculations [86], that include both initial and final state multiple scattering (which determine the strength of this transverse momentum imbalance) and

in which the suppression of the cross-section in d+Au collisions arises from cold nuclear matter energy loss and coherent power corrections, have also been very successful in describing the data.

The 2015 p+Au run at RHIC has provided unique opportunities to study this channel in more detail at STAR. The high delivered integrated luminosities (0.45 pb^{-1}) allow one to vary both the trigger and associated particle p_T from 1 GeV to 4 GeV, thereby crossing the saturation boundary as shown in Figure 2-26 and reestablishing the correlations for central p+Au collisions for forward-forward π^0's. In 2015 STAR took not only p+Au collisions for this channel, but also p+Al collisions with an integrated luminosity of 1 pb^{-1}. This provides for the first time the opportunity to test also the A-dependence of the saturations scale as predicted by models.

Studying di-hadron correlations in p+A collisions instead of d+A collisions has a further advantage. In reference [87], the authors point out that the contributions from double-parton interactions to the cross-sections for d+A → $\pi^0\pi^0$X are not negligible. This mechanism is illustrated in Figure 2-27.

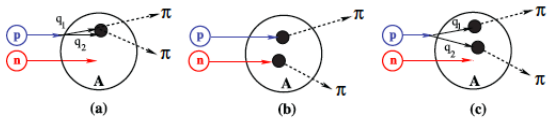

Figure 2-27: Contributions to two-pion production in d+A collisions through the double-interaction mechanism [87].

They find that such contributions become important at large forward rapidities, and especially in the case of d+A scattering. Whether or not this mechanism provides an alternative explanation of the suppression of the away-side peak in π^0-π^0 can be settled with the 2015 p+A data.

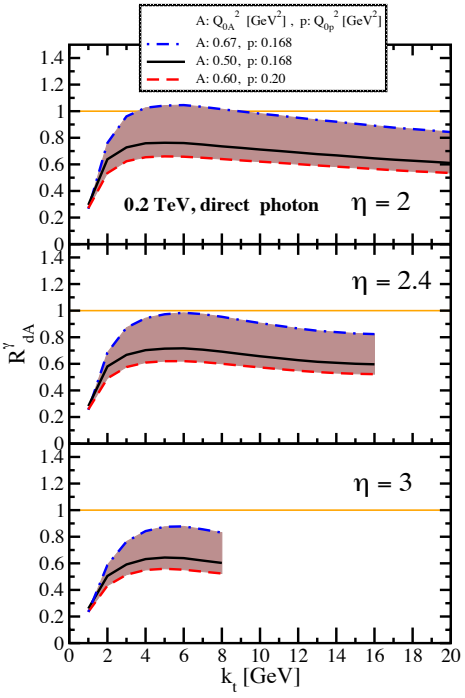

Figure 2-28: Nuclear modification factor for direct photon production in p(d)A collisions at various rapidities at RHIC $\sqrt{s}$ = 0.2 TeV. The curves are the results obtained from Eq. (12) in Ref. [88] and the solution to rcBK equation using different initial saturation scales for a proton Q_{op} and a nucleus Q_{oA}. The band shows our theoretical uncertainties arising from allowing a variation of the initial saturation scale of the nucleus in a range consistent with previous studies of DIS structure functions as well as particle production in minimum-bias p+p, p+A and A+A collisions in the CGC formalism, see Ref. [88] for details.

It is very important to note that for the measurements to date in p(d)+A collisions both initial and final states interact strongly, leading to severe complications in the theoretical treatment (see [89, 90] and references therein). As described in detail in the Section above in p+A collisions, removing the strong interaction from the final state, by using photons and Drell-Yan electrons, can ameliorate these complications. The Run-2015 p+A run will for the first time (see Figure 2-17) provide data on R_{pA} for direct photons and therefore allow one to test CGC based predictions on this observable as depicted in Figure 2-28 (taken from Ref. [88]). The higher delivered integrated luminosity for the upcoming p+Au and p+Al run in 2024 together with the proposed forward upgrade will enable one

to study more luminosity hungry processes and/or complementary probes to the di-hadron correlations, i.e. photon-jet, photon-hadron and di-jet correlations.

We use direct photon plus jet (direct γ+jet) events as an example channel to indicate what can be done in 2024. These events are dominantly produced through the gluon Compton scattering process, g+q→ γ +q, and are sensitive to the gluon densities of the nucleon and nuclei in p+p and p+A collisions. Through measurements of the azimuthal correlations in p+A collisions for direct γ+jet production, one can study gluon saturation phenomena at small-x. Unlike di-jet production that is governed by both the Weizsäcker-Williams and dipole gluon densities, direct γ+jet production only accesses the dipole gluon density, which is better understood theoretically [88,91]. On the other hand, direct γ+jet production is experimentally more challenging due to its small cross-section and large background contribution from di-jet events in which photons from fragmentation or hadron decay could be misidentified as direct photons. The feasibility to perform direct γ+jet measurements with the proposed forward upgrade in unpolarized p+p and p+Au collisions at $\sqrt{s_{NN}}$=200 GeV has been studied. PYTHIA-8.189 [92] was used to produce direct γ+jet and di-jet events. In order to suppress the di-jet background, the leading photon and jet are required to be balanced in transverse momentum, $\left|\phi^{\gamma} - \phi^{jet}\right| > 2\pi/3$ and $0.5 < p_T^{\gamma}/p_T^{jet} < 2$. Both the photon and jet have to be in the forward acceptance $1.3 < \eta < 4.0$ with $p_T > 3.2$ GeV/c in 200 GeV p+p collisions. The photon needs to be isolated from other particle activities by requiring the fraction of electromagnetic energy deposition in the cone of ΔR=0.1 around the photon is more than 95% of that in the cone of ΔR=0.5. Jets are reconstructed by an anti-k_T algorithm with ΔR=0.5. After applying these selection cuts, the signal-to-background ratio is around 3:1 [93]. The expected number of selected direct γ+jet events is around 1.0M/0.9M at $\sqrt{s_{NN}}$=200 GeV in p+Au/p+Al collisions for the proposed run in 2024. We conclude that a measurement of direct photon-hadron correlation from p+A collisions is feasible, which is sensitive to the gluon density in 0.001<x<0.005 in the Au nucleus (see Figure 2-29) where parton saturation is expected.

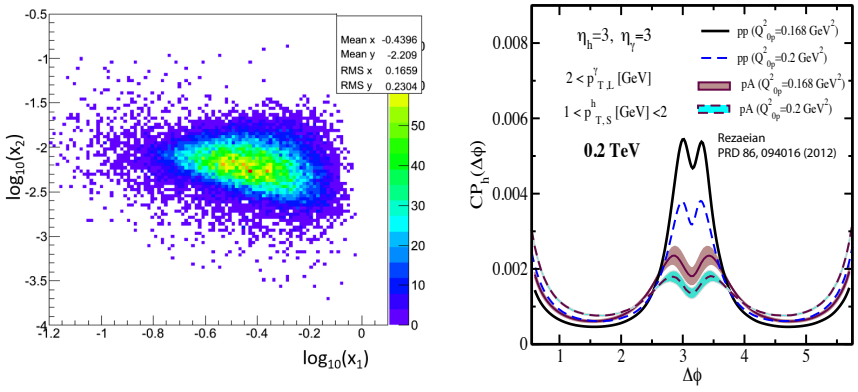

Figure 2-29: Left: Bjorken-x distributions of hard scattering partons in direct γ+jet production after event selections described in the text in p+p collisions at $\sqrt{s}$=200. Right: γ-hadron azimuthal correlation in minimum bias p+p and p+Au collisions at $\sqrt{s_{NN}}$=200 GeV. The curves are obtained with two different initial saturation scale of proton Q^2_{0p}=0.168 and 0.2 GeV^2 and the corresponding initial saturation scale in the nucleus within Q^2_{0A}~3-4Q^2_{0p} (c.f. [88,91]).

Summary of the pp and pA measurements:

In Table 2-1 summarizes the pp and pA the scientific goals and measurements critical to reach these goals as discussed in the prior chapters. In addition, the needed integrated luminosity as well as the detector components of the forward upgrade critical for the observable are listed.

	Year	$\sqrt{s}$ (GeV)	Delivered Luminosity	Scientific Goals	Observable	Required Upgrade
In parallel with sPHENIX running	2024	p↑p @ 200	300 pb^{-1} 8 weeks	Subprocess driving the large A_N at high x_F and η	A_N for charged hadrons and flavor enhanced jets	Forward instrum. ECal+HCal+Tracking
	2024	p↑Au @ 200	1.8 pb^{-1} 8 weeks	What is the nature of the initial state and hadronization in nuclear collisions Clear signatures for Saturation	R_{pAu} direct photons and DY Dihadrons, γ-jet, h-jet, diffraction	Forward instrum. ECal+HCal+Tracking
		p↑Al @ 200	12.6 pb^{-1} 8 weeks	A-dependence of nPDF, A-dependence for Saturation	R_{pAl}: direct photons and DY Dihadrons, γ-jet, h-jet, diffraction	Forward instrum. ECal+HCal+Tracking
Potential future running	2021/22	p↑p @ 510	1.1 fb^{-1} 10 weeks	TMDs at low and high x	A_{UT} for Collins observables, i.e. hadron in jet modulations at $\eta > 1$	Forward instrum. ECal+HCal+Tracking
	2021/22	$\vec{p}\vec{p}$@ 510	1.1 fb^{-1} 10 weeks	$\Delta g(x)$ at small x	A_{LL} for jets, di-jets, h/γ-jets at $\eta > 1$	Forward instrum. ECal+HCal

Table 2-1: Summary of the pp and pA measurements as planed in the years 2021 and 2024. The most right coloumn summarizes, which detector of the forward upgrade is essential for the measurement.

2.5 Ridge in p+p, p+A and A+A

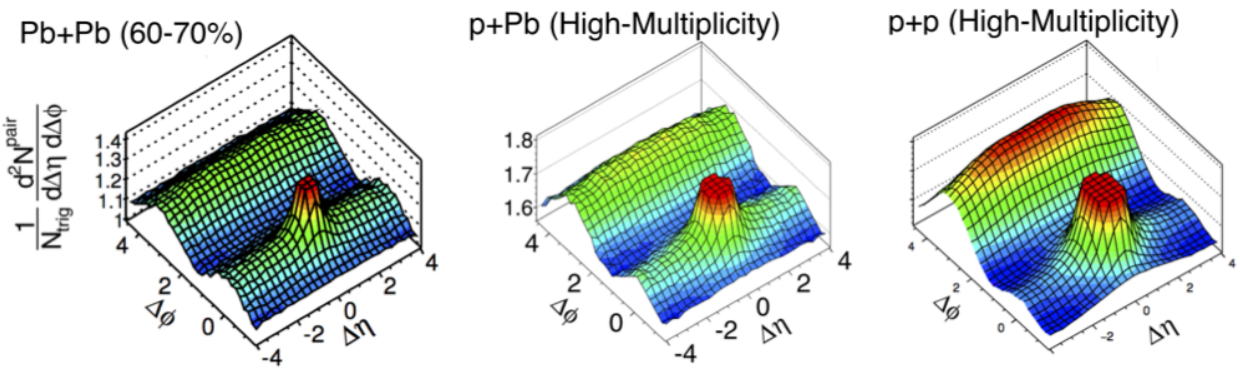

Figure 2-30: Long-range ridge structure observed in the di-hadron correlations measured in relative pseudorapidity and azimuthal angle in peripheral Pb+Pb and high multiplicity p+Pb and p+p collisions [94,95,96,97]

In heavy-ion (A+A) collisions the QCD matter formed immediately after the collisions undergoes a pre-equilibrium evolution and eventually evolves to a phase describable by viscous hydrodynamics. The most convincing evidence of such a scenario has been the long-range two-dimensional (2D) di-hadron correlation functions (per-trigger-particle associated yield distribution) expressed in terms of relative pseudorapidity *(Δη)* and azimuthal angle *(Δϕ)* of the emitted particles as shown in the left panel of Figure 2-30 (left). Such correlations include two major components, the di-jet and the ridge. The back-to-back di-jet correlations give rise to a narrow near-side peak at ($\Delta\eta$=0, $\Delta\phi$=0) but can extend over the entire $\Delta\eta$ range on the away side $\Delta\phi\sim\pi$) whereas the long-range ridge-like correlations can persist up to large $\Delta\eta$ on both near and away sides. The ridge-like correlations are attributed to nearly boost-invariant (longitudinally invariant) hydrodynamic response of initial-state spatial anisotropy created at the early stages of collisions.

For years, collisions of small systems, such as hadronic (p+p) and light-heavy-ion (p/d/He^3+A), have been providing baselines for measurements in A+A collisions. Such consensus has been strongly challenged by the recent striking observation of the long-range ridge like structure in the high multiplicity events in p+p and p+Pb collisions as shown in Figure 2-30 (middle and right).

An outstanding question is: does the same underlying mechanism drive these long-range correlations in all collision systems shown in Figure 2-30? The applicability of hydrodynamics is often debated in small collision systems particularly due to lack of evidences that can support the formation of a nearly equilibrated system. However, it has also been recently argued that criteria such as thermalization or isotropizations are not necessary for the applications of hydrodynamics [98]. Therefore, hydrodynamics can be a correct approach to describe small collision systems in principle down to the size of QCD matter of about 0.15 fm [98]. Several hydrodynamic calculations have successfully described many aspects of the experimental results in the small system collisions [99].

The alternative approaches are based on gluon saturation or Color Glass Condensate (CGC) that indicates intrinsic initial-state momentum space correlations of partons that survive the process of hadronization can lead to ridge-like structure of di-hadron correlations [100]. Many such predictions based on gluon saturation have been verified at LHC indicating small-*x* dynamics playing an important role in the multi-particle production at high energies. In the CGC picture, the energy dependence of ridge-like correlations is determined by BK/JIMWLK evolution equations of non-linear QCD. In the saturation regime, CGC predicts an energy independent scaling of the strength of ridge-like correlations when measurements are performed for events with fixed multiplicity [100]. Measurement of ridge correlations over a wide range of energy will be essential to test such predictions. A systematic breaking of such scaling will be essential to probe the regime of multi-

particle production dominated by non-linear small-x dynamics of QCD. Along with the existing LHC data, high multiplicity p+p and p+A collisions at RHIC provide unique opportunities in this context. Since RHIC kinematics are very different from those at the LHC, a measurement of the ridge-like correlations in p+A collisions at RHIC would provide direct access to the distribution of gluons inside hadrons at lower energies (large-x).

Measurements at RHIC can also provide a decisive test to distinguish whether the long-range correlations in small systems is due hydrodynamic response to the initial-state spatial correlations or due to the intrinsic momentum space correlations developed in the saturated wave functions of the colliding systems. An interesting approach taken so far at RHIC was to study various small collision systems such as p+Au, d+Au and ^{3}He+Au [101]. Comparisons with hydrodynamic calculations have confirmed the expectations based on initial shapes of such collision systems [102]. It is however remain to be seen if initial-state models can also explain such data.

Earlier measurements of long-range ridge-like correlations at RHIC have previously been performed via di-hadron correlations, with an attempt to subtract the elliptic-flow and jet contributions from the region around $\Delta\phi \sim 0$ and designating the remaining yield as ridge [103]. However such measurements have been limited to light-heavy-ion collisions, low-statistics data sets and most importantly over a very narrow window of pseudorapidity $|\Delta\eta| < 2$. The planned forward upgrade of STAR will increase the capability of measurement of di-hadron correlations over a wide range of $\Delta\eta$ and with high statistics (providing more high-multiplicity events). For example, a measurement of correlations between the detected particles in the forward rapidity with the charged particles from mid-rapidity, with a large $\Delta\eta$ gap will be ideal for investigating the physics of the ridge at RHIC energies. Along with providing direct access to non-linear dynamics of QCD, in certain window of kinematics, such measurements might enable us to distinguish between final-state effects such as hydrodynamic response to initial geometry and intrinsic initial-state effects such as momentum-space correlations due to gluon saturation.

2.6 Correlation Measurements to Characterize Hot and Dense Nuclear Matter

One of the primary goals of the forward upgrade program of STAR is to explore the longitudinal structure of the initial-state and the temperature-dependent transport properties of the matter in relativistic heavy-ion collisions (HICs). The most conventional measurement in this context is the transverse momentum-dependent two-particle correlation function in relative azimuthal angle and pseudorapidity $C(\Delta\eta,\Delta\varphi)$. The current acceptance of the STAR detector ($-1<\eta<1$) limits the window of such a measurement to $|\Delta\eta|<2$ ($|\Delta\eta|<3.4$, with the iTPC upgrade). The proposed forward upgrade of STAR with the FTS (FCS) detector, providing an additional with acceptance of $-4.2<\eta<-2.5$, $p_T(E_T)$ information, and enhanced rate capabilities, will enable high-statistics measurements of long-range correlations $C(\Delta\eta,\Delta\varphi)$ up to $\Delta\eta\sim5.2$ ($\Delta\eta\sim5.9$ with the iTPC). Figure 2-31 demonstrates how the STAR forward upgrade with the FTS (FCS) will extend the two-particle phase space (in terms of η_1 and η_2) by about a factor of 6.5.

The importance of the measurements of long-range correlations can be understood as follows. As demonstrated in Figure 2-32 due to causality, correlations developed at different times over the evolution of a heavy-ion collision will spread to different ranges of space-time rapidities. In an approximately boost-invariant scenario, such correlations will appear at different values of the two-particle rapidity difference ($\Delta\eta$ or Δy). Correlations that span a wide range in rapidity are thus dominated by the early-time dynamics of the collision, although there is considerable "thermal blurring" [104]. The goal of the forward upgrade is thus to measure such long-range correlations to explore the initial states of both A+A and light-ion+A collisions.

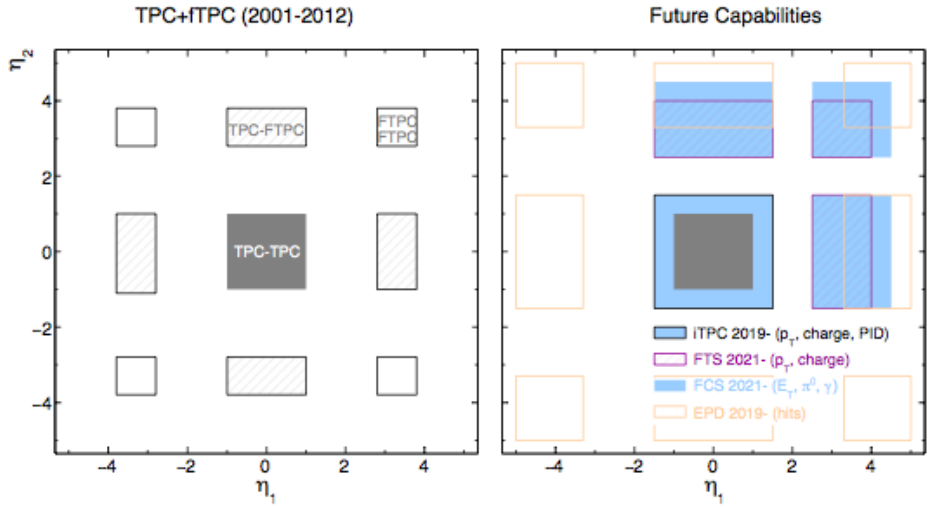

Figure 2-31: (left panel) The pseudorapidity coverage (area in the $\eta_1 \times \eta_2$ space) of the STAR detector prior to the removal of FTPC in 2012. (right panel) The projected $\eta_1 \times \eta_2$ acceptance after the iTPC and the forward upgrade shown can be quantified as $|\Delta\eta|^2$. One finds, $|\Delta\eta|^2$ (past, before 2012) = $(2+1.5 \times 2)^2 = 25$, $|\Delta\eta|^2$ (current, 2012-17) = $(2)^2 = 4$, $|\Delta\eta|^2$ (with forward upgrade) = $(2+1.7)^2 = 13.7$, $|\Delta\eta|^2$ (with iTPC & forward upgrade) =26.

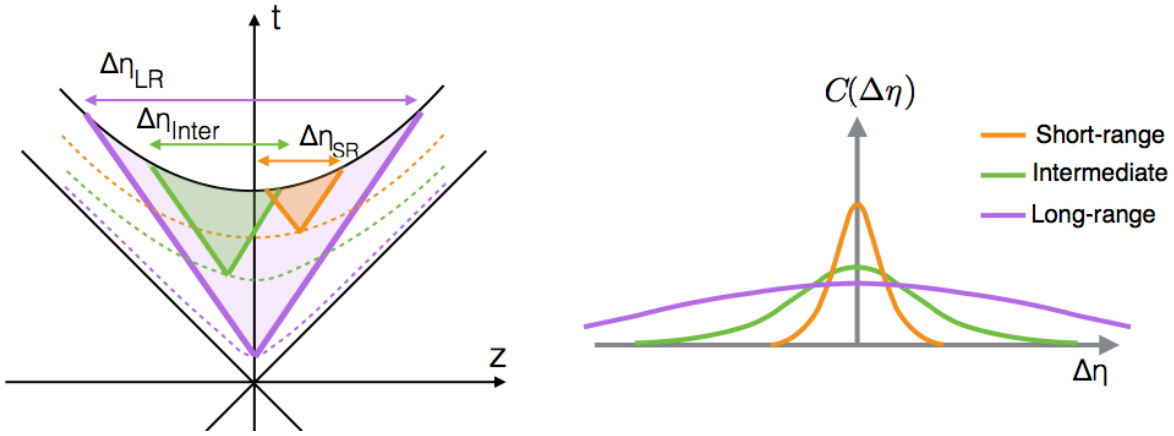

Figure 2-32: An illustration (inspired by Ref [105]) of the time evolution of correlations spreading over different windows of Δη in a heavy-ion collision (left).

In the subsequent stages of evolution, fluid-dynamic response of the system converts the initial-state spatial correlations to long-range momentum-space correlations. Therefore, measurements of such long-range correlations can also provide ways to study the transport properties of such fluid-dynamical evolution. As we argue in the following section, the combination of STAR's wide acceptance and the versatility of RHIC provides a unique opportunity to explore the rich dynamics that drives the early stages of collisions as well as the subsequent stages of evolution via measurements of long-range correlations over a wide range of energy and for varying collision systems.

In particular, the STAR forward upgrade will address the following two major topics:

- Constraining the longitudinal structure of the initial stages of HICs
- Constraining the temperature dependence of transport coefficients of the matter formed in HICs

In addition, the forward upgrade will also enable studies of jets, underlying correlations, event-shape engineering [106], removal of the background for the chiral magnetic effect [107], etc. Also, in the case of light+heavy-ion collisions, the current upgrade will provide the opportunity to pin down the origin of initial-state and final-state interactions.

2.6.1 A more precise estimation of flow through measurements of long-range correlations

So far, long-range correlations at RHIC have been analyzed through the measurement of a ridge-like structure along $\Delta\eta$ (at $\Delta\varphi$~0) of the di-hadron correlation function $C(\Delta\eta,\Delta\varphi)$. As we have discussed in the previous chapter, in HICs such correlations are a consequence of initial-state geometric fluctuations and nearly boost-invariant fluid-dynamic evolution. In particular for the transverse-momentum range of $p_T < 3$ GeV, the long-range ridge-like correlations in HICs are dominantly driven by anisotropic flow. The strength of the long-range azimuthal ridge-like correlations are often characterized by the Fourier coefficients $V_{n\Delta}$ (which can be related to the single-particle azimuthal anisotropy harmonics v_n) obtained after the harmonic decomposition of the di-hadron correlation functions integrated over $\Delta\eta$. As shown in Figure 2-32 (right), since at small $\Delta\eta$ different sources of short-range and intermediate-range correlations (e.g. HBT, Coulomb, Jet-Fragmentation, thermal fluctuations etc.) dominate the $\Delta\eta$ dependence of the correlation function $C(\Delta\eta)$, a precise extraction of $V_{n\Delta}$ can only be possible by measurements over a wider range of rapidity.

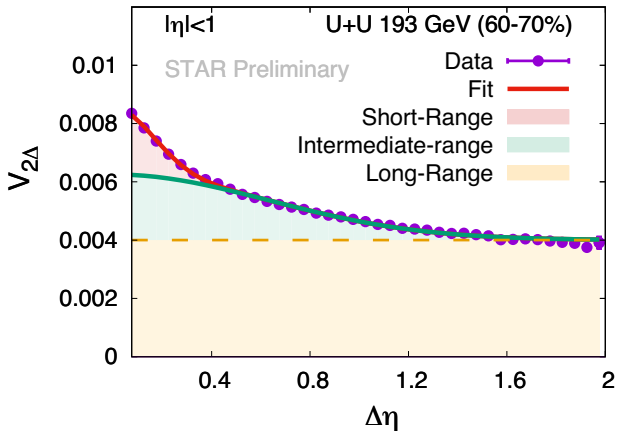

Figure 2-33: The STAR measurement of the relative pseudorapidity ($\Delta\eta$) dependence of the second order Fourier harmonic coefficient $V_{2\Delta}$ of two-particle azimuthal correlations at mid-rapidity in 193 GeV U+U collisions. The measurement over the limited window of $|\eta|<1$ indicates that the long-range flow driven component of $V_{2\Delta}$ has contamination from short-range non-flow contributions. The proposed upgrade of STAR will extend the window of $\Delta\eta$, allowing for improved removal of non-flow correlations and thus a more precise estimation of the flow-driven component of $V_{2\Delta}$.

Figure 2-33 shows the STAR preliminary measurement of $V_{2\Delta}$ in a window of $|\Delta\eta|<2$ at mid-rapidity using the Time Projection Chamber ($|\eta|<1$). Double Gaussian fits indicate the presence of both a short-range (red shading) and an intermediate-range (green shading) correlation. These contributions are effectively backgrounds to the long-range flow-driven components of $V_{2\Delta}$ which are shown with the yellow shading below the dashed line in Figure 2-33. These backgrounds arise from non-flow contributions in the late stages of the collisions. It is only for the largest (presently accessible) values of $\Delta\eta$ do these backgrounds disappear. This clearly demonstrates the importance of increasing the longitudinal acceptance of the STAR detector, so that short-range non-flow correlations can be efficiently removed for precise extraction of $V_{n\Delta}$. Thus, the precision measurement of $V_{n\Delta}$ will lead to : 1) better constraints on the initial stages of HICs 2) more precise estimations of transport parameters such as η/s involved in the fluid-dynamic evolution of the subsequent phases of HICs [108,109,110]. Such measurements are of highest priority for the ongoing and the upcoming physics program at RHIC because the matter formed in HICs is expected to have its smallest η/s value near the transition region ($T=T_C$) from strongly correlated Quark Gluon Plasma (sQGP) to hadronic phase.

RHIC collisions spend relatively more time in that region of minimum η/s and are therefore best suited for studying the most perfect liquid known in nature as compared to collisions at LHC energies. Several recent theoretical estimates demonstrate that RHIC provides the best constraint on η/s at T_c [108,109,110]. The importance of the "Characterization of liquid QGP" through more precise measurements of its transport parameters (and its temperature dependence) has been mentioned as one of the future goals in the 2015 Long-range Plan for Nuclear Science (LRPNS) [111].

2.6.2 Constraining longitudinal structure of the Initial stages of Heavy Ion Collisions

Significant theoretical and experimental efforts have been made in recent times to understand the fluctuating structure of the initial stages of HICs. Although our knowledge of transverse (perpendicular to the collision axis) density fluctuations has improved over the years, the longitudinal structure of the initial-state has remained largely unexplored. One of the main challenges to model the longitudinal structure of HICs is the lack of experimental constraints. The goal of the STAR forward upgrade project is to provide precision measurements that will inspire studies of the breaking of longitudinal invariance (boost-invariance) and full 3D fluid-dynamic modeling of HICs. The proposed upgrade will teach us: 1) if the effective theories of QCD predict the correct rapidity dependence of the initial state, 2) about the mechanism of baryon stopping and, 3) potentially about the early-time non-equilibrium dynamics that lead to thermalization and formation of the sQGP. Understanding the longitudinal structure of the initial-state is also relevant for a better interpretation of the quantities like flow harmonics $V_{n\Delta}$ that are sensitive to the transverse structure of the initial state.

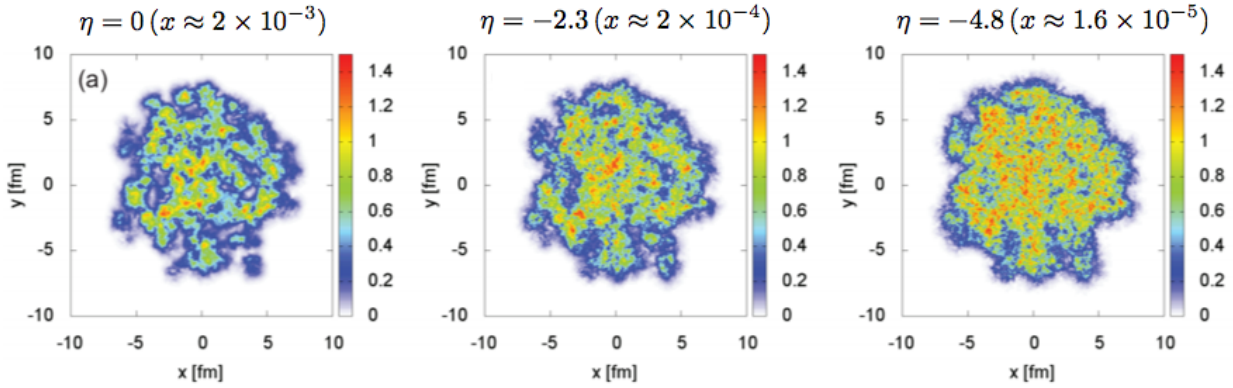

Figure 2-34: Obtained from Ref [112] showing rapidity (Bjorken $x \sim \langle p_T \rangle \exp(-y)/\sqrt{s}$, $y \sim \eta$) evolution of the gluon fields in the transverse plane (perpendicular to the beam axis) inside colliding nuclei obtained by 3D-Glasma model calculations. The three frames show how the length scale of fluctuations vary due to rapidity evolution of the parton densities when going from mid-rapidity to forward rapidity at RHIC. This will lead to the breaking of boost-invariance of the initial conditions, which, can only be probed by measurements at forward rapidities. While 3D-Glasma has been constrained at the LHC, future measurements at RHIC will provide crucial tests for the underlying QCD evolution equation that predicts the rapidity evolution of gluon densities inside the colliding nuclei.

Figure 2-34 shows the theoretical calculation from the 3D-Glasma model of the initial conditions [112], indicating, that the characteristic transverse length scale over which gluon distributions are correlated inside a nucleus changes with the evolution in Bjorken-x. The corresponding (pseudo) rapidity values at RHIC are also shown. Such an evolution of the gluon density will determine the structure of the transverse energy-density at different pseudorapidities,

eventually leading to the breaking of longitudinal invariance. This can only be probed by measurements over a wider range of pseudorapidity. In that context, a large number of observables have been identified that go beyond the conventional measurements of flow harmonics $V_{n\Delta}$ to better quantify the 3D structure of HICs [113,114,115,116,117,118,119,120,121].

For example, the a_{mn} coefficients of the Legendre polynomial decomposition of the two-particle rapidity correlation function, the three particle correlator $C_{m,n,m+n}(\eta_a, \eta_b)$, the $r_n(\eta_a, \eta_b)$ variables etc., which we discuss in the following section, are ideal observables for studying the longitudinal structure of the HICs. Current measurements of some of these observables at RHIC are available for a narrow window of $\Delta\eta$ from STAR. The forward upgrade will allow us to perform measurements over wider $\Delta\eta$ and with greater precision. This will be necessary to confirm predictions from saturation models such as the 3D-Glasma. This model has been constrained at the LHC, but measurements at RHIC will provide crucial tests for the underlying QCD evolution equation that predicts rapidity dependence of the initial state. It must be noted that, even with the measurements of these observables, in HICs it is challenging to directly constrain the longitudinal structure of the initial-state though data-model comparisons without sophisticated modeling of the subsequent sQGP and hadronic phase.

It is worth noting the uniqueness of RHIC for explorations of the longitudinal structure of HICs. Since the beam rapidity at RHIC is smaller than that at the LHC, one expects stronger variations of the initial geometry, fluctuations, energy density, temperature, baryon density, etc., over a relatively smaller window of acceptance. In principle, at RHIC it is possible to build upgrades that reach near-beam rapidity; or even beyond for lower energies (as in the Beam-Energy-Scan program). In addition, the structure of the initial-state and its fluctuations at lower energies have not been well constrained. The proposed upgrade of STAR will help constrain models of initial conditions at lower energies [119], which is absolutely necessary for a successful dynamical modeling of heavy-ion collisions in the Beam-Energy-Scan program.

Along with a state-of-the-art modeling of initial-state geometry and fluctuations by including longitudinal dynamics, a complete modeling of HICs must also include a full treatment of 3+1-dimensional viscous hydrodynamics evolution, and, (ideally) transport of the hadronic phase. Due to the large number of unknown parameters involved in such simulations, uncertainties remain in full 3+1-dimensional modeling of HICs. It turns out that one needs to go beyond the conventional measurement of flow harmonics and find new observables to constrain such models. As mentioned previously, recent combined explorations from both theory and experiment have produced several promising tools for studying longitudinal correlations in HICs [113-121].

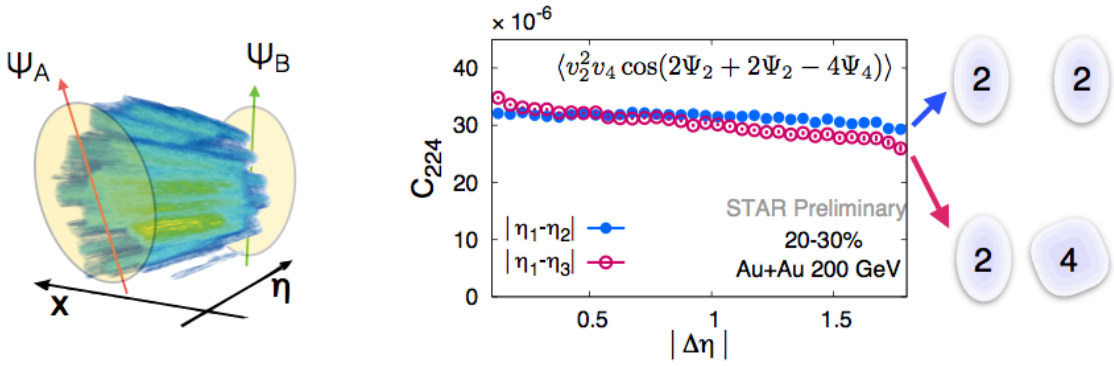

Figure 2-35: (left) A cartoon inspired by Ref [112] showing the deceleration of the transverse geometry characterized by event-plane angles Ψ along the longitudinal (pseudorapidity) direction. (Right) Figure from Ref [113] showing the STAR measurement of such effects through relative pseudorapidity variation of the three-particle azimuthal correlator $C_{2,2,4}(\eta_a,\eta_b)$. Measurements for different harmonics are highlighted to the right of the plot by cartoons of corresponding initial-state anisotropies.

The cartoon in Figure 2-35 demonstrates how the initial-state longitudinal fluctuations and fluid dynamical response of the medium formed in HICs can lead to decorrelations of the reaction planes $\Psi_n(\eta)$ (which determines the orientation of the harmonic anisotropies) in different pseudorapidity regions. Such effects are often referred to as torque or twist of the event shape [114] and can be probed by measurements of mixed harmonic correlations of reaction planes as shown in the right frame of Figure 2-35. Such correlations have been measured in STAR [113] using the relative pseudorapidity dependence of the three-particle correlator $C_{m,n,m+n}(\eta_a,\eta_b) = \langle\cos(m\varphi_1(\eta_a)+n\varphi_2(\eta_b)-(m+n)\varphi_3)\rangle$. In the limited (currently available) acceptance at STAR, a small but significant decorrelation of the event planes is observed [113]. At lower energies such decorrelations are found to be stronger than at higher energies[122]. One also expects the effect of such a decorrelation to be more pronounced over a wider range of relative pseudorapidity. The proposed forward upgrade of STAR will explore the origin of such decorrelations in detail.

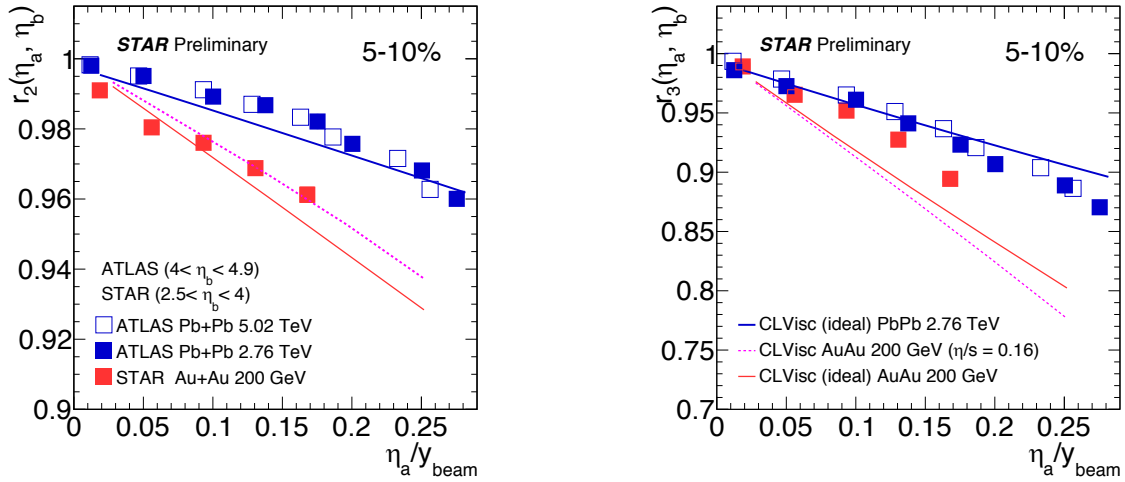

Figure 2-36: The decorrelation of the second v_2 (left panel) and third v_3 (right panel) harmonic anisotropies between η_a and η_{-a} with the reference detector chosen at certain η_b ranges at 5-10%, measured by ATLAS (blue open and solid squares) and STAR (red solid squares), and calculated with a (3+1)D ideal hydrodynamic model for LHC (blue solid lines) and RHIC (red solid lines) energies. The correlator r_n is calculated from the two-particle flow coefficients $V_{n\Delta}$ as: $r_n(\eta_a, \eta_b)$. The model describes the ATLAS 2.76 TeV data and overestimates the effect at RHIC. With a viscosity correction of η /s = 0.16 (magenta dashed line) for RHIC, the results give a weak decorrelation for v_2 and an even stronger decorrelation for v_3.

Another promising observable which measures the decorrelation of azimuthal anisotropies along pseudorapidity is the observable $r_n(\eta_a, \eta_b) = V_{n\Delta}(-\eta_a,\eta_b)/V_{n\Delta}(\eta_a\eta_b)$, where $V_{n\Delta}(\eta_a\eta_b)$ is the Fourier coefficient calculated with pairs of particles taken from different pseudorapidity regions, as introduced in Ref [115]. Figure 2-36 shows the experimental measurement of this observable for two harmonics $r_2(\eta_a, \eta_b)$ and $r_3(\eta_a, \eta_b)$ by the ATLAS collaboration [115] and preliminary results from STAR with the existing data from the Forward Meson Spectrometer (a previously operational but presently dismantled subsystem). The results are compared to estimates from a 3+1D hydrodynamic simulation, which predicts a much stronger variation of $r_n(\eta_a, \eta_b)$ with η at RHIC than at the LHC. A similar, stronger longitudinal decorrelation effect was also demonstrated using the AMPT model (see Figure 2-37) [123], where the variation of the observable $C_n(\Delta\eta)\sim\cos(n(\varphi(\eta_a)-\varphi(\eta_b)))$ with $\Delta\eta = |\eta_a - \eta_b|$ was studied. Forward upgrade with increased event plane resolution and differential pT information will enable us 1) to explore new observable for flow decorrelation, to separate contributions from flow magnitude fluctuation and flow phase fluctuation; 2) to study the event-by-event and intra-event fluctuation of v_n in the forward rapidity, where the QGP may have different properties from mid-rapidity; 3) to better constrain the event centrality and centrality fluctuations,

which are important for measurement at mid-rapidity. These possibilities allow us to better constrain the 3D initial condition and full space-time evolution in the final state.

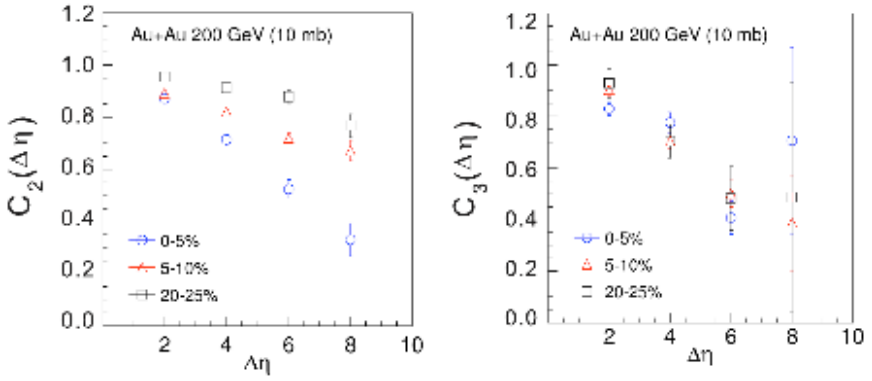

Figure 2-37: AMPT predictions of v_2 and v_3 de-correlation estimated in terms of the observable $C_n(\Delta\eta)$ versus the pseudorapidity at RHIC with given parton cross-sections [123]. $C_n(\Delta\eta)$ directly probes the longitudinal structure of the HICs. The STAR forward upgrade will enable precise measurements of such observables and help constrain 3D modeling of HICs.

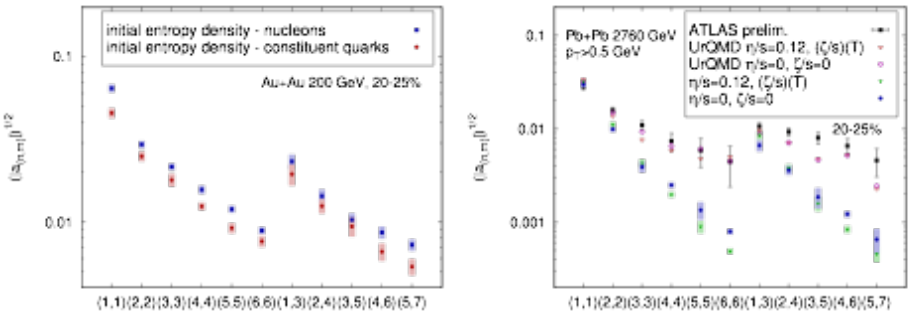

Figure 2-38: The The *amn* coefficients obtained from the two-particle pseudorapidity correlation functions projected onto a basis set of Legendre polynomials [116,117,118] for different combinations of orders *m* and *n*. Model calculations [119] are done with a 3+1D viscous hydrodynamic simulation for RHIC (left panel) and the LHC (right panel). The model calculations shown in the right panel are compared to the LHC data, whereas the proposed forward upgrade will constrain the prediction shown in the left panel.

Observables like $C_{m,n,m+n}(\eta_a, \eta_b)$ and $r_n(\eta_a,\eta_b)$ are designed to study the longitudinal dependence of two-particle correlations decomposed in terms of Fourier coefficients. Recent studies have proposed a similar decomposition of the two-particle pseudorapidity correlations in the basis of Legendre polynomials [116,117]. Based on such decomposition, a new observable has been recently introduced by the ATLAS collaboration [118] to characterize the structure of the longitudinal fluctuation which is referred to as a_{mn} coefficients, for which the indices "*m*" and "*n*" correspond to different orders of Legendre polynomials. STAR results for these observables were reported at Quark Matter 2017 [124]. So far, measurements of a_{mn} done at the LHC have been compared to a recent 3+1D viscous hydrodynamic simulation in Ref [108, 119] as shown in Figure 2-38. The study has shown that the coefficients a_{mn} are not very sensitive to the transport properties of the sQGP. They are however sensitive to the initial-state longitudinal fluctuations and the hadronic re-scattering and decays at the final stages of the collisions. With the future forward upgrade, measurements of this observable at RHIC over a wider range of rapidity will provide insight about energy dependence of the longitudinal fluctuations, further constraining the initial-state models of HICs. Also since the effect of the hadronic phase is different at lower collision energies, the measurements at RHIC will allow ways to constrain the hadronic transport models ("afterburners") used along with the 3D hydrodynamic models. Full 3D fluid-dynamical modeling is crucial for data-model comparisons and interpretations of several experimental results at RHIC. In particular, at the lower energies of the

RHIC BES program, baseline predictions from 3D fluid-dynamical models are important in the search for the QCD critical point.

Constraining the temperature dependence of the transport parameter η/s (T)

The QCD matter formed at RHIC shows nearly perfect fluidity characterized by the smallest viscosity to entropy ratio *η/s* known in nature. Although significant efforts from both theory and experiment have been dedicated towards the precise extraction of *η/s*, the temperature dependence of this transport parameter has not been fully constrained. A major goal of the STAR forward upgrade is to provide precision measurements to contain the temperature dependence of the transport parameters *η/s* (*T*) (and *ζ/s* (*T*)) of the matter formed in HICs.

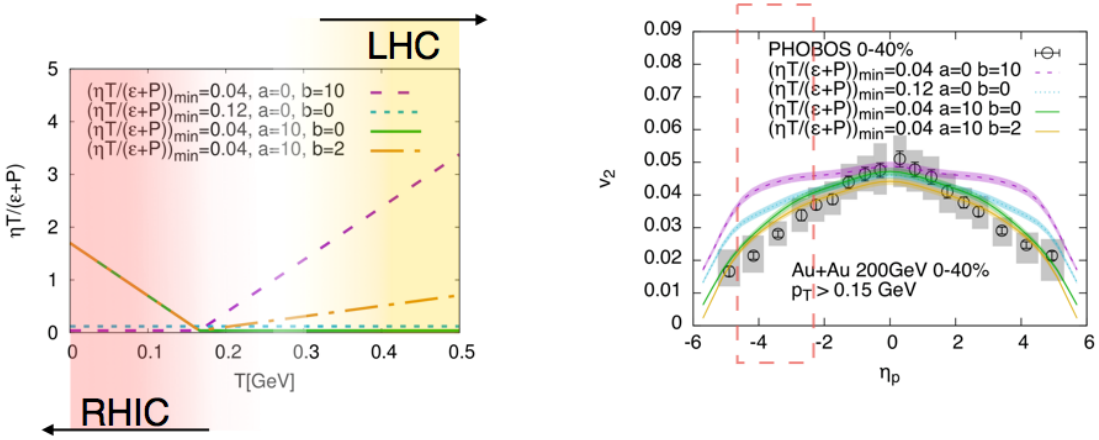

Figure 2-39: (left) Different parameterizations of temperature dependence of shear viscosity to entropy *η/s* (at zero chemical potential) used in the hydrodynamical simulation of Ref [108]. Interestingly, it has been demonstrated in Ref [110] that the region of lowest *η/s* is the one that can be probed at RHIC. (Right) Effects on the elliptic flow co-efficient v_2 due to the different parameterizations of the viscosity parameter indicating better constraints on *η/s(T)* can only be performed by measurements at forward rapidities at RHIC. The red box shows the region of the proposed STAR upgrade. The interpretation of the PHOBOS results is limited by the large uncertainties.

Recently, hydrodynamic simulations have demonstrated that since the temperature of the produced fireball in HICs vary with the rapidity, the measurement of the rapidity dependence of flow harmonics has the potential to constrain *η/s* (*T*) and *ζ/s* (*T*) [108]. The advantage of performing such measurements at RHIC over LHC is 1) the measurement can be more precise because, even at a single energy, the smaller beam rapidity at RHIC provides stronger variations of the temperature with rapidity, 2) measurements at RHIC can be done over a wide range of energy which, in addition to rapidity, provide an additional handle on temperature to map *η/s* (*T*), and *ζ/s (T)* over a wide range of temperature. In particular, the hydrodynamic simulation of Ref [110] indicates that *η/s*(*T*) at lower temperatures, near its possible minimum ($T=T_c$), can be better constrained at RHIC.

Figure 2-39 shows the results of a very recent theoretical calculation using event-by-event 3+1D viscous relativistic hydrodynamic simulations from Ref [108]. In this simulation, a number of QCD-motivated parameterizations of the temperature dependence of the shear viscosity was assumed, as shown in Figure 2-39 (left). It was shown that a precise measurement of the pseudorapidity dependence of the flow harmonics is instrumental in discriminating such parameterizations. A comparison to the predictions from this study with the existing elliptic flow as a function of pseudorapidity, v_2 (*η*), data from RHIC is shown in Figure 2-39 (right). However, due to the large uncertainties and limited acceptance of the currently available measurements, only limited conclusions can be drawn on the temperature dependence of the transport parameters. The forward

upgrade of STAR will provide precise estimation of $v_2(\eta)$ and other higher-order flow coefficients $v_n(\eta)$ that are essential in terms of constraining $\eta/s\ (T)$ near its possible minimum.

Additional studies using the proposed forward upgrade

The forward upgrade of STAR, with its wide acceptance and enhanced-rate capabilities, will be useful for many other measurements that are important towards understanding the properties of the hot and dense matter formed at RHIC. Along with the previously mentioned main interests, the forward upgrade program of STAR will also enable us to perform many more interesting studies such as:

- In 2017, the STAR Collaboration has published in NATURE [125] the discovery of Global Hyperon Polarization (GHP) in the most vortical fluid known. GHP is predicted to grow with rapidity due to the increase of QGP hydrodynamic viscosity. This discovery provides a new tool for studying viscosity and vorticity at RHIC from top energies to the BES-II energies. Even with the multiple major upgrades in recent years, the STAR detector is only capable of tracking and particle identification of hyperons within pseudorapdity of $|\eta|<1.5$. First simulations, still to be refined, show that the proposed forward upgrade allow us to reconstruct Lambdas in both polarized p+p collisions at 500 GeV and non-central Au+Au collisions at different energies.
- Event-shape engineering [126,127] and correlation between flow harmonics to test the non-linear hydrodynamic response.
- Data-driven subtraction of anisotropic-flow backgrounds in jet-correlations measurements.
- Background estimation to improve the presently observed signals of charge separation in the search for the Chiral Magnetic Effect [107].
- Independent estimation of centrality to remove auto-correlations in the study of higher moments of conserved-charge fluctuations in the search for the QCD critical point.

In summary, the forward upgrade program of STAR will enable us to study the longitudinal structure of the initial-state that leads to the breaking of boost invariance in heavy-ion collisions and to explore of the transport properties of the hot and dense matter formed in heavy-ion collisions near the region of perfect fluidity. The measurements at forward rapidity at RHIC will provide crucial tests for the effective theories of high-energy QCD and its evolution equation, such as BK or JIMWLK [112], that predicts the rapidity dependence of the parton densities inside the colliding nuclei that leads to the fluctuating structure of the initial states in heavy-ion collisions.

Physics Measurements		**Longitudinal de-correlation $C_n(\Delta\eta)$ $r_n(\eta_a,\eta_b)$**	**η/s(T), ζ/s(T)**	**Mixed flow Harmonics $C_{m,n,m+n}$**	**Ridge**	**Event Shape and Jet-studies**
Detectors	**Acceptance**					
Forward Calorimeter **(FCS)**	$-2.5 > \eta > -4.2$ E_T (photons, hadrons)	One of these detectors necessary		One of these detectors necessary	Good to have	One of these detectors needed
Forward Tracking System **(FTS)**	$-2.5 > \eta > -4.2$ (charged particles)		Important		Important	

Table 2-2: Physics measurements in A+A collisions with the proposed forward upgrade and with other STAR upgrades that are relevant to those measurements.

Such studies will be essential for a smooth transition toward the physics program in e+A collisions at a future Electron Ion Collider (EIC). Understanding the longitudinal structure of the

initial-state will lead to a better understanding of the early time non-equilibrium dynamics that leads to thermalization and the formation of the sQGP. Measurements at forward rapidities will also provide more insights about baryon stopping. In particular, the proposed upgrade program will help constrain full three-dimensional fluid-dynamical modeling of heavy-ion collisions. Such modeling will be essential to provide baseline predictions for the search for the QCD critical point. In addition, increasing the rapidity acceptance of STAR will allow for more precise measurements of anisotropic flow and its rapidity dependence. Building on the discovery of the perfect liquid, such measurements at RHIC will be crucial for mapping out the temperature-dependent transport properties that characterize such an extreme state of matter. A brief summary of the different heavy-ion physics topics, and the corresponding detector requirements for each, are listed in Table 2-2.

3 Forward Upgrade Overview and Simulation

3.1 Forward Calorimeter System

The STAR forward upgrade is motivated to a large extent to explore QCD physics in the very high and low regions of Bjorken *x*. Previous STAR efforts using the FPD and FMS detectors, and the recently refurbished FMS and a new pre-shower and post-shower detector upgrade for Runs 2015-2017, have demonstrated that there are outstanding QCD physics opportunities in the forward region. In order to go beyond what STAR has/will achieve with the currently existing forward detector system, a forward detector upgrade with superior detection capability for neutral pions, photons, electrons, jets and leading hadrons covering a pseudo-rapidity region of 2.5-4 in the years beyond 2020 is proposed. The forward upgrade program of STAR will also enable to study the longitudinal structure of the initial state that leads to breaking of boost invariance in heavy ion collisions and explore of the transport properties of the hot and dense matter formed in heavy ion collisions near the region of perfect fluidity. Table 3-1 gives a summary of the detector requirements of the different components of the forward upgrade based on the discussed pp, pA and AA physics programs.

Detector	pp and pA	AA
ECal	~10%/√E	~20%/√E
HCal	~50%/√E+10%	---
Tracking	charge separation photon suppression	$0.2<p_T<2$ GeV/c with 20-30% $1/p_T$

Table 3-1: Requirements of the different forward upgrade detector parts for the different physics programs summarized in Table 2-1 and Table 2-2.

The design of the FCS is a modification of the original proposed Forward Calorimeter System and is driven by required detector performance, integration into STAR and cost optimization.

Figure 3-1 shows the location of the proposed FCS at the West side of the STAR detector system and a schematic description of the FCS in the STAR three-dimensional CAD model. The original design of the FCS consisted of a Spaghetti ElectroMagnetic Calorimeter (SPACal) followed by a Lead and Scintillating Plate sampling Hadronic Calorimeter (HCal) with a tower size of $10\times10\times81$ cm^3 corresponding to 4-interaction length. The SPACal is made of Tungsten powder and scintillating fibers as such it has achieved one of the highest densities and among the most compact calorimeters [128]. The goal was to have a fully compensated calorimeter system. With the end of the PHENIX data-taking in 2016, the PHENIX ECal [129] became available. The PHENIX ECal has the required energy resolution and constitutes therefore a very cost-effective alternative. The only drawback is that the calorimeter system will not be fully compensated anymore. The read-out for the refurbished PHENIX ECal will be placed in the front so that there will be no significant dead gaps between the ECal and the HCal. Wavelength-shifting slats are used to collect light from the HCal scintillating plates to be detected by photon sensors at the end of the HCal. Both calorimeters will share the same cost-effective readout electronics and SiPMs as photo-sensors.

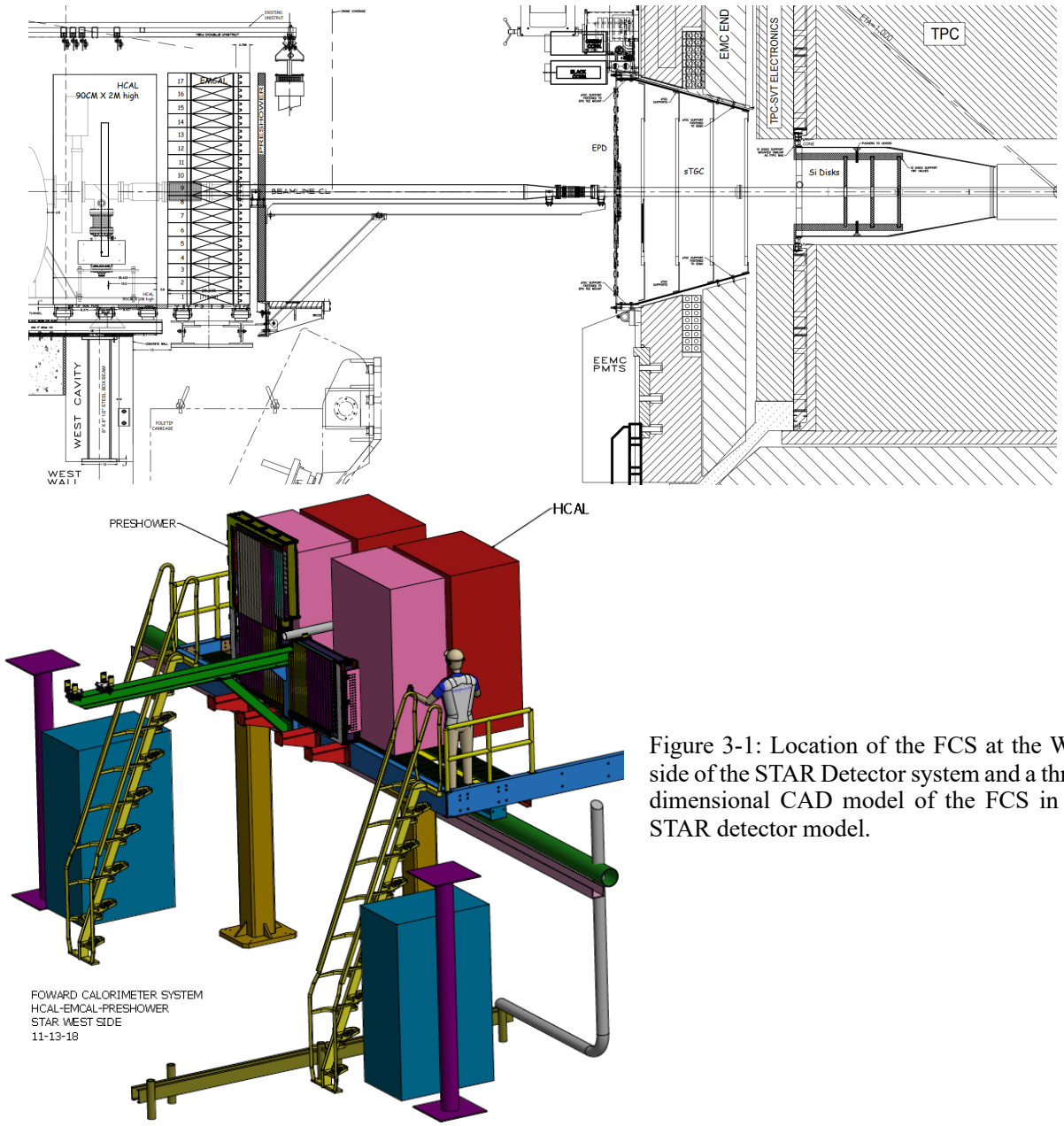

Figure 3-1: Location of the FCS at the West side of the STAR Detector system and a three-dimensional CAD model of the FCS in the STAR detector model.

3.2 FCS Simulation results

A series of simulation studies have been carried out for the Forward Calorimeter System, based on the detector geometry described above and in Section 4. These studies fall into several categories: simulations of the response of the ECal and HCal to single particles (photons or charged pions); kinematic studies; quality of jet reconstruction (comparing results at particle vs. detector level, as explained below); and estimates of systematic and statistical errors for some physics observables of interest, which were introduced in Section 2.2.

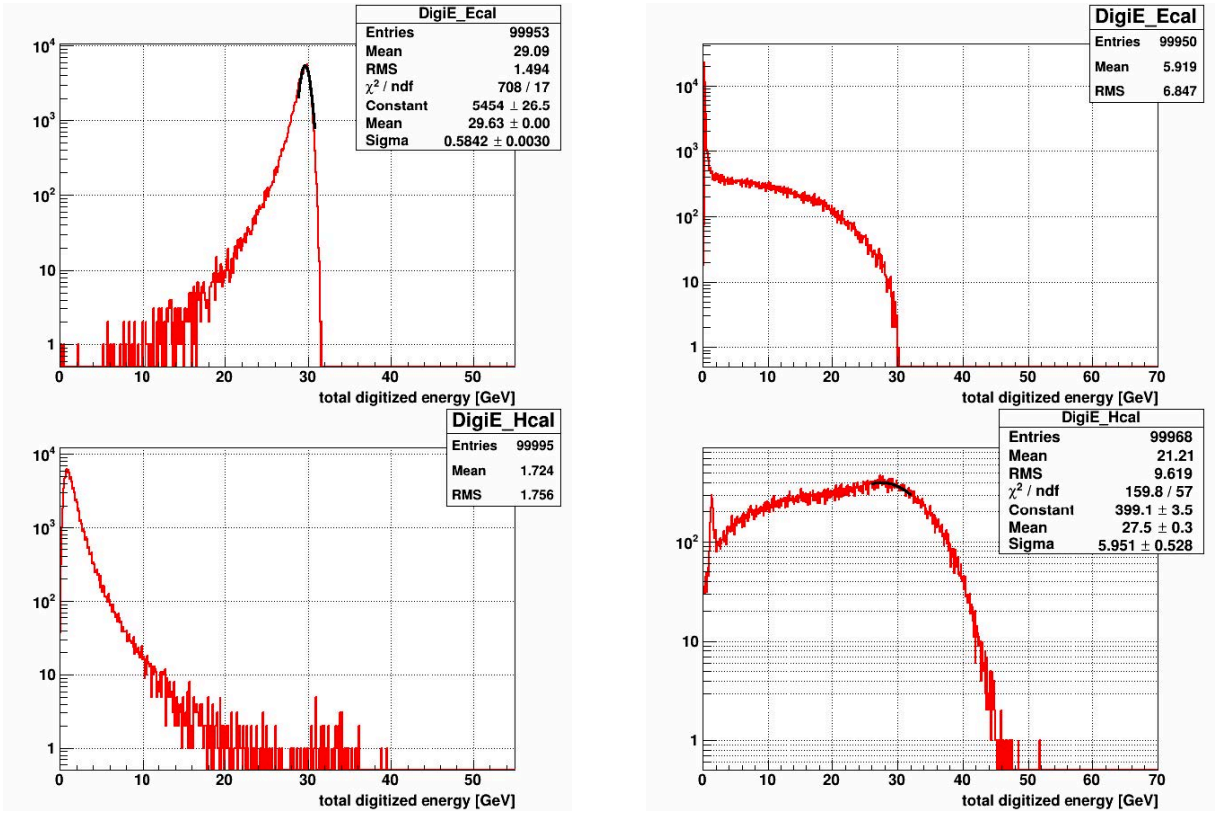

Figure 3-2: Simulated response of the ECal (upper) and HCal (lower) to a 30 GeV photon (left) or 30 GeV charged pion (right). The particle is thrown at η =3 near the middle of the detector in ϕ. Sampling fractions of 0.20 and 0.0145 were assumed.

A detailed model of the envisioned FCS has been incorporated into the GEANT simulation package of the STAR detector. Because the calorimeter system is not fully compensated, a first step was to examine the ECal and HCal responses to individual e.m. particles (photons) or hadron (π^-) over a range of incident energies from 3-100 GeV. Typical spectra are shown in Figure 3-2, for which 100k particles were generated at an energy of 30 GeV and a pseudorapidity of 3. The particles were distributed evenly over a small range in azimuth near the center of each detector.

The plots on the left demonstrate the expected FCS response to a high-energy photon. For most events, a very large fraction of the energy is deposited in the ECal (upper plot), as expected. The HCal detects the energy leaking 'out the back' of the ECal, as well as those components of the e.m. shower that pass through the gaps between individual towers, due to their quasi-projective geometry. This also explains the small peak observed near 30 GeV in the HCal as arising from the rare photon that passes undisturbed through the whole ECal via such gaps. The responses of the two calorimeters to an individual photon are thus highly correlated, as can be seen in the left plot of Figure 3-3. The non-compensated nature of the detector is reflected in a slope that deviates from unity.

The right-hand plots in Figure 3-2 provide similar information for incident charged particles, in this case negative pions. While most deposit only a mip-equivalent in the ECal (upper right plot), a non-negligible fraction will interact hadronically in this detector, resulting in the broad smearing towards lower energies observed in the HCal response. The correlation between the two detectors is again fairly tight (right plot in Figure 3-3) though not as linear as for e.m. particles. Based on plots of this sort, we are just starting to investigate simple algorithms for combining the energy information collected from the two detectors.

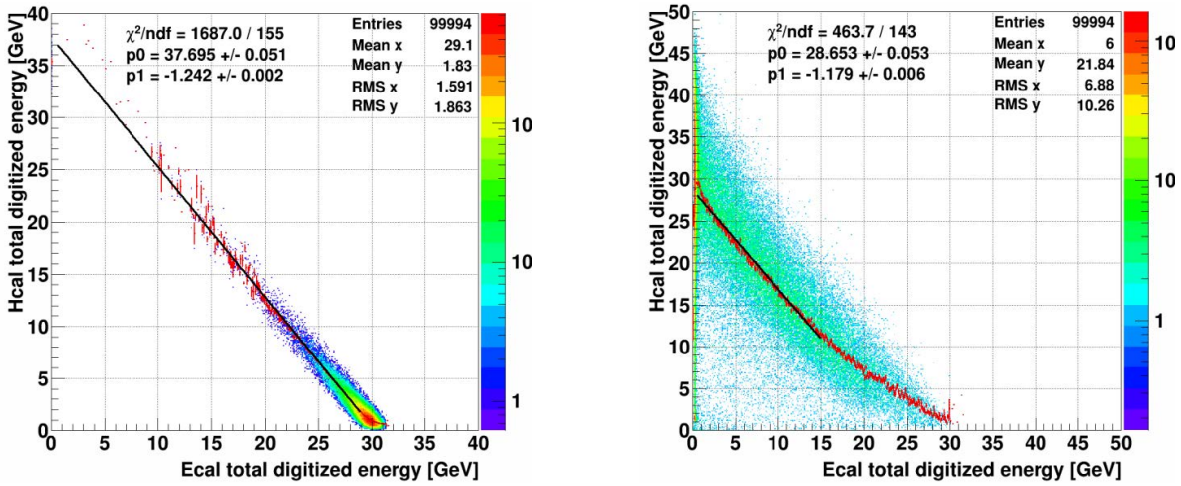

Figure 3-3: Correlation between the ECal and HCal responses shown in Fig. 3-2 for 30 GeV photons (left) and 30 GeV negatively charged pions (right). Due to being non-compensated, the response to e.m. particles is linear but with a slope not equal to -1, while the response to hadrons is globally better, but far from linear.

3.2.1 Jet measurements

For single- (inclusive) and di-jet events, the jet pseudorapidity η and p_T are related to the underlying partonic variables x_1 and x_2. We studied these relations for the STAR geometry, including the FCS, for realistic x_1 and x_2 distributions. More importantly, we also examined the matching that can be achieved between reconstructed jets and scattered partons, and the resolutions with which the parton axis can be reconstructed from the reconstructed detector jets. The latter is important to understand, in order to evaluate how well azimuthal asymmetries around the outgoing parton axis will be reconstructed by looking at asymmetries of individual particles around the reconstructed jet axis.

For our initial study on jet kinematics, we used 500k events simulated with PYTHIA Tune A at $\sqrt{s}$ = 500 GeV and a minimum partonic p_T (CKIN3) of 3 GeV. We then used a fast simulation of the detector resolutions of the STAR Barrel, Endcap, and Forward calorimeters. For the FCS, we assumed hadronic and electromagnetic calorimeters with $0.58/\sqrt{E}$ hadronic resolution and an electromagnetic resolution of $0.11/\sqrt{E}$. Jets were reconstructed with an anti-k_T algorithm with a radius R of 0.7. An association, or "matching," between a reconstructed jet and a scattered parton is established if they are separated by a distance in η-ϕ space of less than 0.5. In the following, we refer to reconstructed jets as "detector jets," and jets found using stable, final state particles (from the PYTHIA record) as "particle jets." The outgoing partons in the event were determined by using the corresponding entries in the PYTHIA record, so there is no partonic jet finding in this analysis.

Figure 3-6 shows the regions of x that can be accessed by jets in the forward region. A minimum jet p_T of 3 GeV/c was chosen to ensure that the momentum transfer is sufficiently high for pQCD calculations to be valid. At high x, values of $x \sim 0.6$ should be reachable. This compares well with the current limit of SIDIS measurements, $x \sim 0.3$, and encompasses the region in x that dominates the tensor charge. To investigate the possibility of selecting specific x regions, in particular high x, the dependence of x on the jet p_T and pseudorapidity was studied. Figure 3-5 shows x_1 as a function of jet p_T, while Figure 3-6 and Figure 3-7 show the η–dependence in the Endcap and FCS regions for

two p_T bins. For both the η and p_T dependences, one can observe two bands: one that exhibits an η or p_T dependence (at higher x), and one that remains at low x. Based on these kinematic correlations, it is clear that large x values can be reached with good purity at high η and/or p_T.

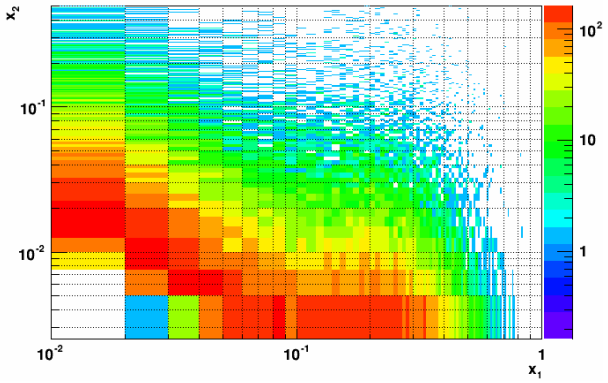

Figure 3-4: Distribution of the partonic variables x_1 and x_2 for events with a jet with $p_T > 3$ GeV/c and $2.8 < \eta < 3.5$. x_1 values of around 0.6 can be reached whereas x_2 goes as low as 7×10^{-3}.

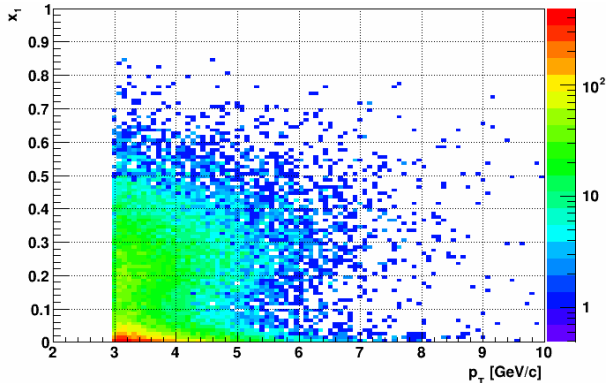

Figure 3-5: x_1 versus jet p_T. The expected correlation between the x accessed and the p_T of the jet is seen. The band of low x_1 values can be reduced by restricting the jet η range – here, $2.8 < \eta < 3.8$.

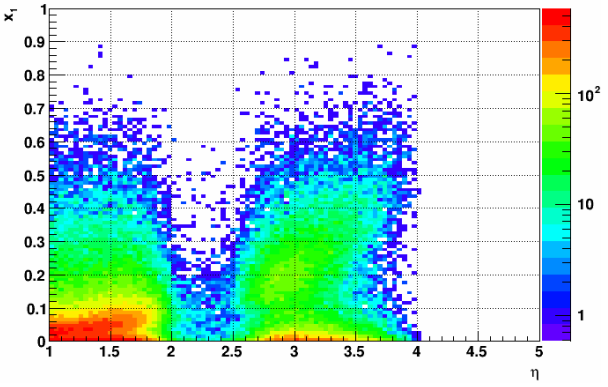

Figure 3-6: x_1 vs jet η. A minimum jet p_T of 3 GeV/c was required. The events are split into two bands in x. One exhibits a strong correlation with η, whereas the other is flat at low x_1. With the forward upgrade x_1-values between 0.15 and 0.3 are accessible.

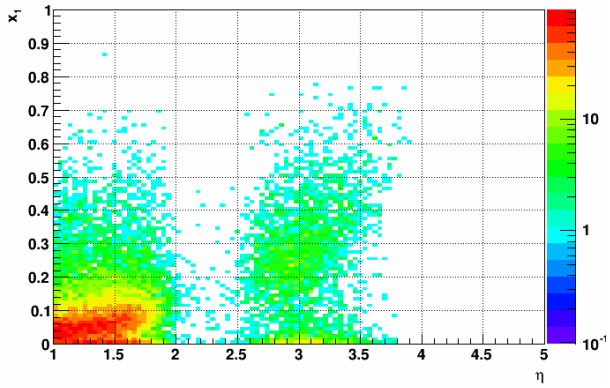

Figure 3-7: Same as Figure 3-6, but with a minimum jet p_T of 5 GeV/c. This shows that additional p_T cuts allow one to push the accessible mean x to higher values. In this case, x_1 values between 0.2 and 0.4 are achievable.

For measurements of azimuthal asymmetries of jets, or (especially) hadrons within a jet – quantities needed in order to probe the transverse spin structure of the nucleon – it is important to reconstruct reliably the outgoing parton direction. For these types of studies, a more realistic model of the FCS is required, *i.e.*, one that simulates the correct geometry and detector responses. For the work shown here, 500 GeV *pp* events were generated using PYTHIA 6.4.28, tune 370 (Perugia 2012), with no partonic p_T cut. The events were then filtered, and only accepted for further processing if the total particle energy in the range $2.0 < \eta < 4.5$ exceeded 50 GeV. Accepted events were run through a full Geant simulation of the FCS. Jet reconstruction, based on an anti-k_t algorithm and a cone radius of 0.6, was performed on the simulated events, with all particles of reconstructed $E_T > 50$ MeV used as input. Jets were kept for further analysis if their transverse momentum exceeded 3 GeV at detector (reconstructed) level and at least 1 GeV at particle (PYTHIA) level. Finally, to remove the jets most susceptible to reconstruction error, we imposed a fiducial cut, requiring that the detector-level thrust axis lie more than 0.2 (in η-ϕ) inside the outer edges of the front face of the ECal.

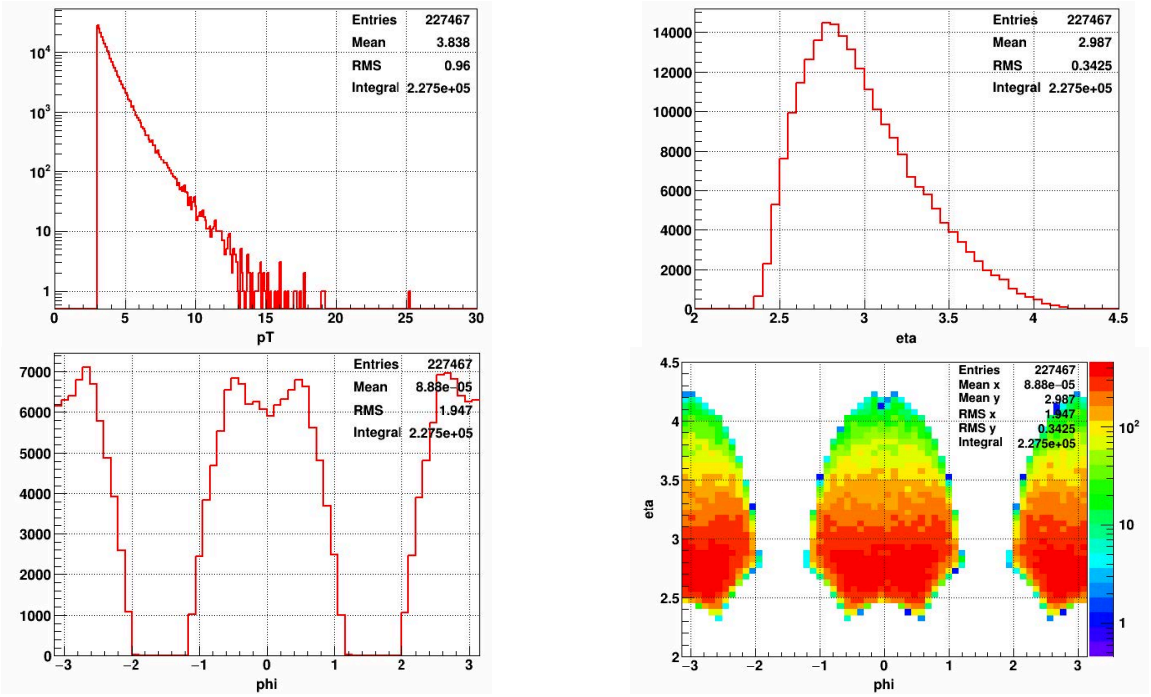

Figure 3-8: Distributions of detector-level jets, as described in the text, as a function of the reconstructed transverse momentum (upper left), pseudorapidity (upper right), azimuth (lower left), and η-ϕ (lower right).

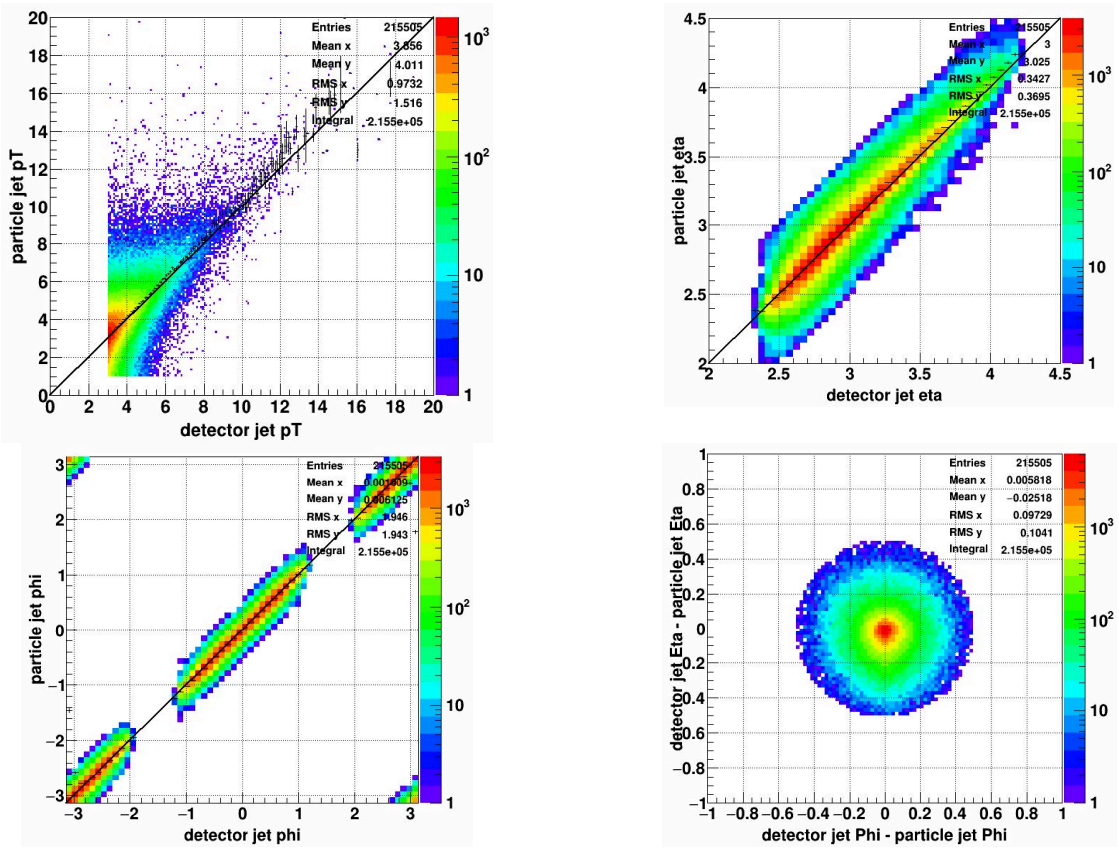

Figure 3-9: Comparisons of key jet parameters between their values calculated at particle level, based on the PYTHIA record, to the values determined through jet reconstruction based on the FCS response.

The distribution of the reconstructed jets, as functions of jet p_T, η, ϕ, and the η-ϕ correlation, are shown in Figure 3-8, indicating the effects of the 'box' geometry of the FCS detectors, as well as the rapid fall-off in jet cross section at forward rapidities. Of more relevance to the physics program

proposed here, Fig. 3-9 shows the correlation, or matching, between these same parameters when determined at detector level (simulated data) or particle level ("truth").

The plots presented in Figure 3-9 are very encouraging: relatively little distortion is observed for the jet direction in either η or ϕ. As expected, the detector-level jet eta (upper right) is 'pulled' to somewhat larger values at the outer edges of the detectors (near $\eta \approx 2.5$), and to smaller values at the inner edges, due to particles in the jet simply missing the detector. These effects, and similar features in phi, can be mitigated through more aggressive fiducial cuts applied to the jet direction, at some cost in detector acceptance and statistics. The detector level p_T is consistently ~5% lower than the value determined at particle level.

3.2.2 Physics observables

Section 2 describes the envisioned science program with the FCS and FTS. Jets are among the experimentally more elaborate probes in this program. The remainder of this section focuses on some of the proposed jet measurements and quantifies the anticipated precision from simulation.

Longitudinal Spin Physics

Figure 3-10 shows the correlation of the particle and detector di-jet mass based on the fast simulation framework discussed earlier. Good correlation is found for all four topological di-jet configurations. This study assumes only a forward calorimeter system. The impact of a tracking system based on silicon disks would have a marginal effect on the p_T reconstruction, considering the STAR magnetic field configuration. However, a tracking system is expected to improve the actual localization and separation of jets, in particular for the FCS+FCS di-jet topology that gives access to the lowest possible values of Bjorken-x. High rate capability and efficiency are essential performance measures in particular for background rejection. The FCS and FTS upgrade is required for these measurements. In addition to di-jet correlation measurements, we will make measurements of π^0-jet correlations, with the neutral pion reconstructed at forward rapidity as a systematic cross-check [130]. The NLO framework for hadron / hadron jet measurements exists [131].

The proposed forward di-jet production measurements, shown in Figure 2-11, in combination with measurements of the current STAR acceptance region, would allow STAR to probe spin phenomena of gluons well below the region of x that is currently accessible.

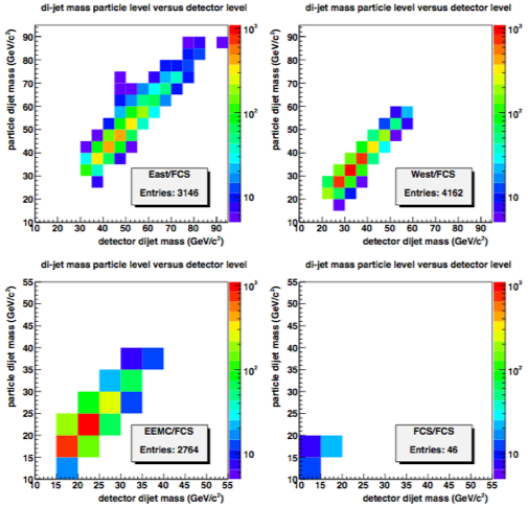

Figure 3-10: Correlation of the particle and detector di-jet mass, including effects for the forward STAR acceptance region.

Transverse Spin Physics

As discussed in Section 2.2, the spin-dependent azimuthal distribution of charged particles within jets is sensitive to quark transversity × Collins fragmentation, resulting in a so-called Collins asymmetry. RHIC measurements are complementary to those that will be carried out at Jefferson Lab,

with unique sensitivity at forward rapidity. In Figure 3-11, we show the expected Collins asymmetries for $p^{\uparrow} + p \rightarrow \text{jet} + \pi^{\pm} + X$ for $2.8 < \eta < 3.7$ and $\sqrt{s} = 500$ GeV. Jets are required to have a minimum p_T of 3 GeV/c. The 2008 transversity and Collins fragmentation function parameterization by the Torino group [28] has been inserted into a leading-order PYTHIA simulation using CDF Tune A. Jets are reconstructed utilizing an anti-k_T algorithm, and the asymmetries are calculated relative to the associated hard-scattered parton. The projections assumed 1 fb^{-1} of luminosity with 60% beam polarization. Particle kinematics are reconstructed using a fast simulation of the FTS and FCS detectors. Asymmetries of nearly 2% are expected for both flavors of pions. In Figure 3-12 we show a comparison of di-hadron asymmetries at the detector level, with the fast simulation detector smearing, to those at the particle level, before simulated detector smearing. Based on these simulations, the effects of kinematic smearing on the asymmetries are expected to be quite small. This suggests that within the same subsystem, one can simultaneously measure in a robust fashion the Collins asymmetry (within the TMD framework) and the di-hadron asymmetry (within the collinear framework). These measurements are critical for extending current understanding of transversity and questions concerning TMD evolution, factorization breaking, and universality, as well as longstanding questions about the nature of large inclusive asymmetries seen in p+p collisions.

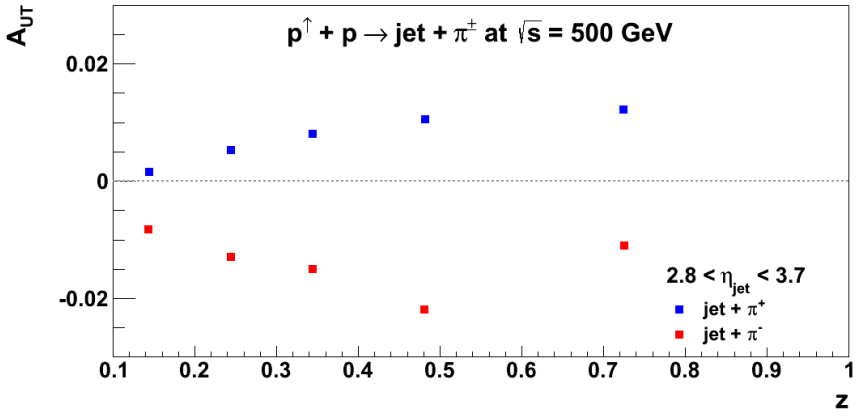

Figure 3-11: Expected Collins asymmetries assuming the Torino parameterization [28] within a leading-order PYTHIA Monte Carlo for charged pions within jets produced with $2.8 < \eta < 3.7$ and $p_T > 3$ GeV/c.

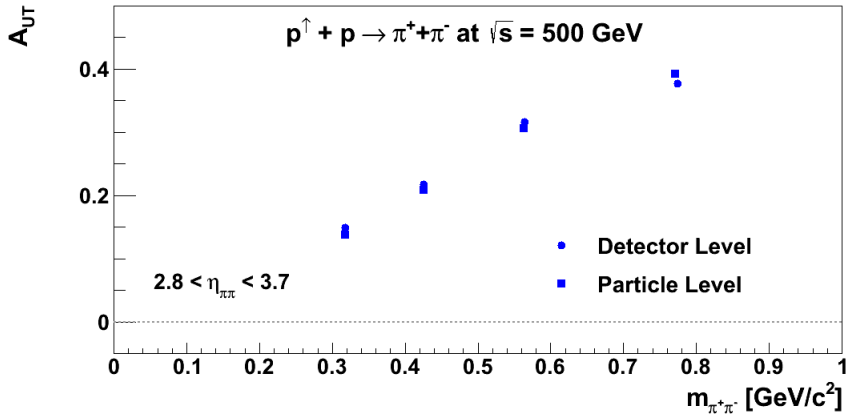

Figure 3-12: Comparison of IFF asymmetries at the detector level and at particle level for charged pions produced in $2.8 < \eta < 3.\ 7$. Asymmetries are shown as a function of di-hadron invariant mass, using a parameterization inspired from fragmentation function measurements at Belle [27]. Statistical uncertainties are smaller than the size of the points.

The above figures suggest that with the proposed forward upgrade detectors, and assuming realistic values for the integrated luminosity that may be achieved, it should be possible to measure both Collins and IFF asymmetries with statistical uncertainties far smaller than the predicted values. For the Collins measurement, however, and certainly for studies of the Sivers effect (predicted to be several times smaller), it is essential to have confidence that the dominant sources of systematic error can be kept under control. To test this, we took our sample of PYTHIA jets (those that would be run through the full Geant simulation described previously, results shown in Figure 3-8 and Figure 3-9) and randomly assigned each a spin state of either 'up' or 'down.' Depending on its spin state and

other properties, such as pseudorapidity, each jet was given a weight factor that deviated slightly from 1, in a manner that would mimic the effects of a Sivers or Collins asymmetry. We then ran the weighted sample through Geant. Using the same jet requirements – and in particular, imposing the same fiducial cut to eliminate jets that pointed within $R < 0.2$ of all detector edges – we extracted the asymmetries of interest, and compared our results to the input values.

The spin-dependent yield asymmetries extracted in this procedure are shown in Figure 3-13. For the Sivers effect (left), one calculates asymmetries as a function of azimuthal angle ϕ, and searches for a cos ϕ dependence. The effects of the 'box' detector geometry, with acceptance gaps near $\pi/2$ and $3\pi/2$, are clearly seen in the error bars. We note that for a vertically polarized beam the gaps occur near the asymmetry zero-crossings, and hence result in little loss of statistical precision in determining the cos ϕ amplitude. The Collins effect (right), however, leads to a spin dependence in the pion yield measured azimuthally around the jet thrust axis, denoted as ϕ_C. This angle is sampled with almost equal statistics when averaged over all detected jet directions.

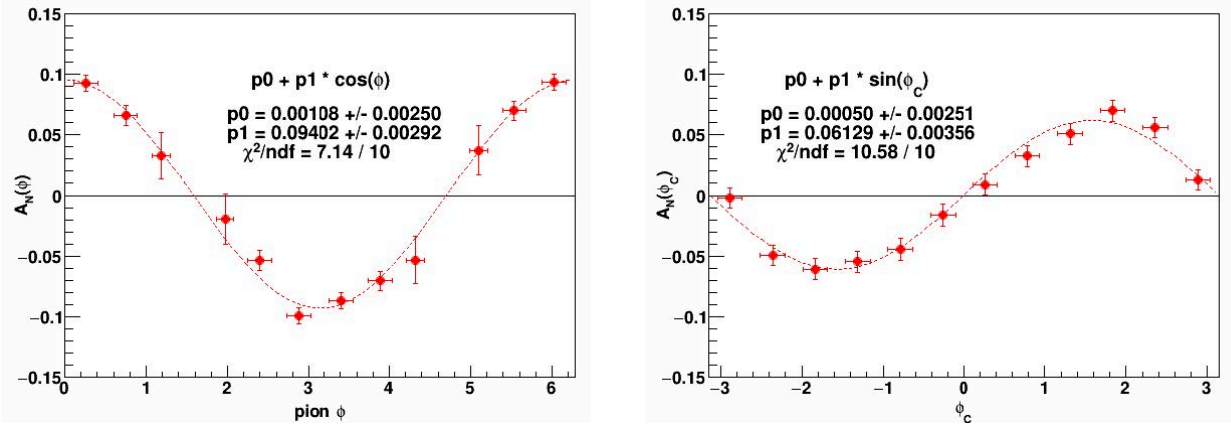

Figure 3-13: Extracted asymmetries for 'toy' models of the Sivers (left) and Collins (right) effects. Key features are explained in the text.

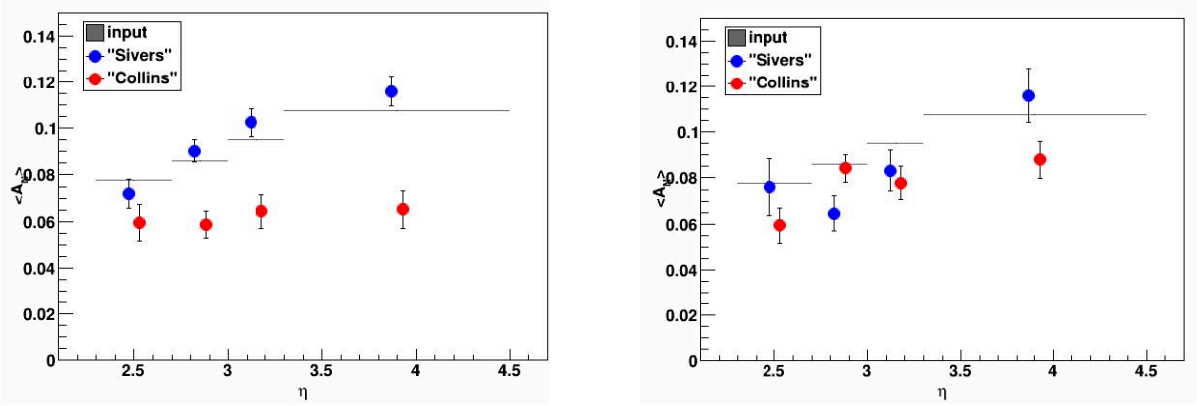

Figure 3-14: Comparisons of the extracted and input values for the Sivers and Collins asymmetries using our 'toy' models. The plot on the left corresponds to expectations with a vertically polarized proton beam, while the plot on the right assumes a sideways, or radial, polarization.

The fitting procedures indicated in Figure 3-13 were carried out after sorting the jets by their pseudorapidity. The fitted amplitudes in each η bin are shown in Figure 3-14 for the two asymmetries, and are compared to the input values, which were chosen to be equal (though η-dependent) in our simple model. For beams polarized vertically (left plot), we see no systematic shift in the extracted Sivers asymmetries, but find substantial dilution of the Collins effect (red points). Given that one is effectively looking for left/right yield differences *relative to the jet direction* for the latter, the FCS geometry appears to introduce severe biases. To understand more definitively the source of the bias, we are investigating several possibilities. By rotating the beam spin into the plane of the RHIC ring,

resulting in a radial polarization (right plot), we see little effect on the Sivers measurement beyond the expected loss of statistical precision, and a significant improvement in the Collins result. We are also exploring other possible solutions, such as increasing the fiducial cut around the detector edges or rejecting all pions that are too close in angle to the jet direction.

In addition to the inclusive jet measurements outlined above, di-jet measurements allow further probes of the transverse momentum-dependent structure of the nucleon. Here the relative transverse momentum between the jets, k_T, gives the additional soft scale needed for the TMD framework. In addition, accessing functions like Sivers [17] and Boer-Mulders [132] in p+p collisions allow one to explore additional asymmetries that may result from the "color-entanglement" in p+p, which also leads to the breakdown of factorization theorems [133].

3.2.3 Drell-Yan capability

The most formidable challenge of DY measurements is to suppress the overwhelming hadronic background. The total DY cross-section is on the order of 10^{-5}-10^{-6} of the hadron production cross-sections; therefore, the probability of mis-identifying a hadron track as e^+/e^- has to be suppressed down to the order of 0.1% while maintaining reasonable electron detection efficiencies. To that end, we have studied the combined electron/hadron discriminating power of the proposed forward tracking and calorimeter systems. We found that by applying multivariate analysis techniques to the features of EM/hadronic shower development and momentum measurements we can achieve hadron rejection powers of 200 to 2000 for hadrons of 15 GeV to 50 GeV with 80% electron detection efficiency. The hadron rejection power has been parameterized as a function of hadron energy and pseudo-rapidity, and has been used in a fast simulation to estimate DY signal-to-background ratios. In the subsection we will describe the procedures of our simulation and discuss some of the results.

We have implemented the exact geometry of the proposed forward calorimeter system in section 0 into the STAR simulation framework. With the EM and hadronic sections, as well as the high-granularity of the ECal, we will be able to measure the shower development in both longitudinal and transverse directions. We have simulated the response of the FCS to single electrons and π^-.

To discriminate EM shower against hadronic shower we have used three observables:

1. **Eratio:**
   the ratio of a 5x5 ECal cluster energy to the sum of the energies of the same 5x5 ECal cluster and the projected 5x5 HCal cluster.
2. **Swidth:**
   The effective ECal shower width defined as $R_p = \sum_i r_i E_i^{0.4} / \sum_i E_i^{0.4}$ where r_i is the distance of the ith tower to the centroid of a 5x5 ECal cluster, and E_i is the energy of that tower. The summation is over the 25 towers in the 5x5 ECal cluster around the highest tower.
3. **NTratio:**
   the number of EM towers with energies above 100 MeV divided by the total number of ECal and HCal towers above the same threshold. All the towers come from a pre-defined 5x5 ECal cluster around the highest tower and the corresponding 5x5 HCal cluster.

Figure 3-15 shows the distribution of these three variables for 30 GeV electrons and π^-, respectively. The FTS helps reject hadrons by measuring the total track momentum. The ratio of energy deposition in the ECal to track momentum (E/p ratio) could serve as additional information in separating $e^{+/-}$ from charged hadrons. The momentum resolution was evaluated from a standalone simulation of the forward tracking system, with typical expected performance for the technology choice and parameterized as a function of energy and pseudo-rapidity. Figure 3-16 shows the parameterized momentum resolution at η = 2.5 and 4.0. Figure 3-17 shows the energy to momentum ratio, E/p, for 30 GeV electrons and π^-.

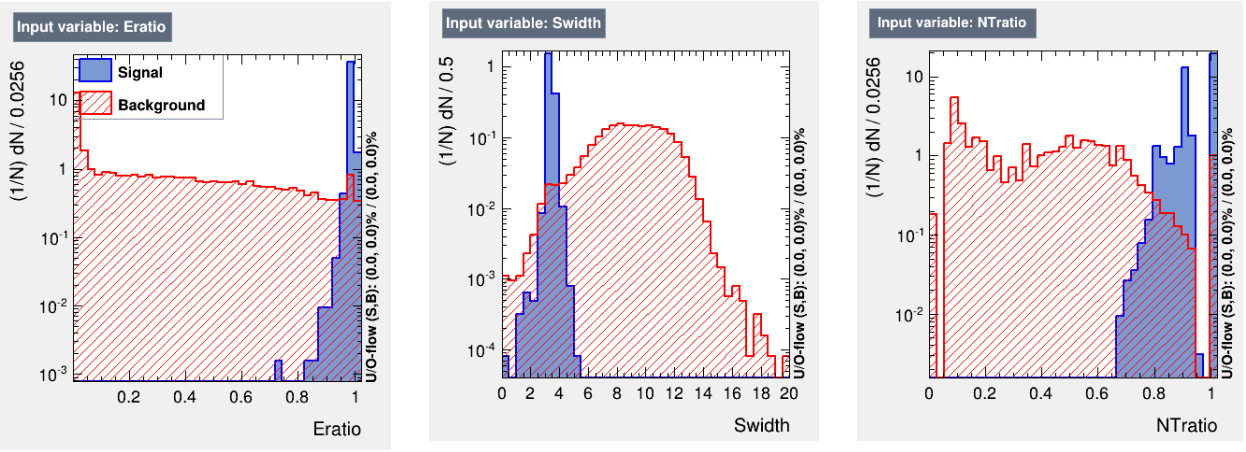

Figure 3-15: Eratio, Swidth & NTratio distribution for 30 GeV electrons (Signal) and π^- (Background). See text for explanation.

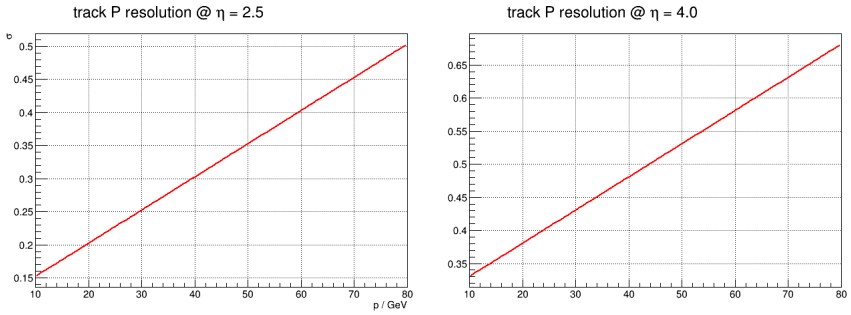

Figure 3-16: Expected track momentum resolution of the forward tracking system from simulations.

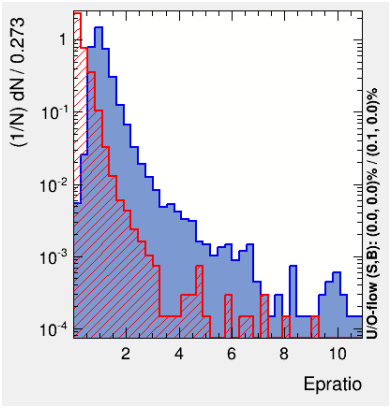

Figure 3-17: *E/p* ratio of 30 GeV electrons (blue) and π^- (red).

These observables from the FTS and FCS have been used as inputs to a Boosted Decision Trees (BDT) algorithm. The BDT contains 1000 binary decision trees: each has a depth of 4 and corresponds to a particular partition of the 4-dimensional feature space into signal (electron) and background (hadron) regions. They are trained sequentially using half of the electron/π^- samples generated. Mis-identified tracks from the previous decision trees were given a higher weight in training the subsequent trees. In the end, each decision tree was given an index representing its performance during the training. In the validation stage, the decision of each track identification was made based on the collective response of all of the decision trees, with each of their responses weighted by the performance index. The boosting algorithm takes advantage of using not only the discriminating power of each single observable, but also the correlations among them.

To estimate the DY signal to background ratio the *e/h* discriminating power has been parameterized as a function of the track energy and the pseudo-rapidity, as is shown in Figure 3-18. We have generated 4 billion PYTHIA p+p events at 200 GeV with CKIN(3) = 3 GeV and a forward filter requiring a total $p_T > 3$ GeV in any of the four jet-patch-like regions in $2.5 < \eta < 4.0$. All basic QCD 2→2 scatterings, as well as heavy flavor channels, were enabled. As a reference we note that 2.5 pb^{-1} p+Au luminosity is equivalent to 500 pb^{-1} p+p luminosity, which corresponds to 240.5 billion p+p events with the above setting. The DY productions through $q\bar{q}$ annihilation and qg scattering processes were separately generated and scaled to 500 pb^{-1}.

Figure 3-19 (left panel) shows the yield of track pairs from a QCD background sample with the proposed cuts applied accumulatively to illustrate the background reduction process from each

step. The final background yields from the 4 billion event sample after gamma/neutron removal + track energy cuts + charge sign requirement and *e/h* discrimination are shown by the green points. The right panel of Figure 3-19 shows the accumulative background reduction factor after each step of applying the cuts.

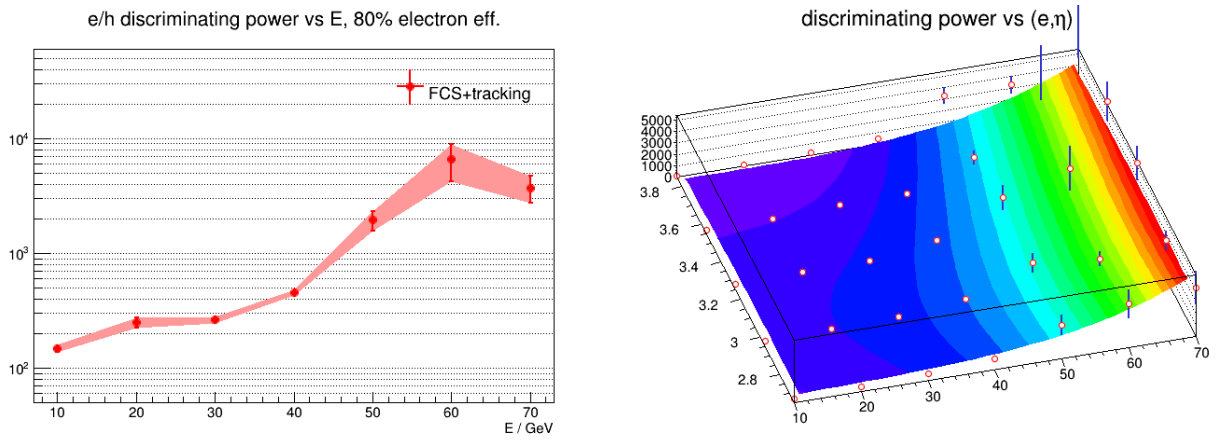

Figure 3-18: *e/h* discriminating power as a function of the track energy (left panel) and the variation over the pseudo-rapidity (right panel) from combined forward tracking and calorimeter systems

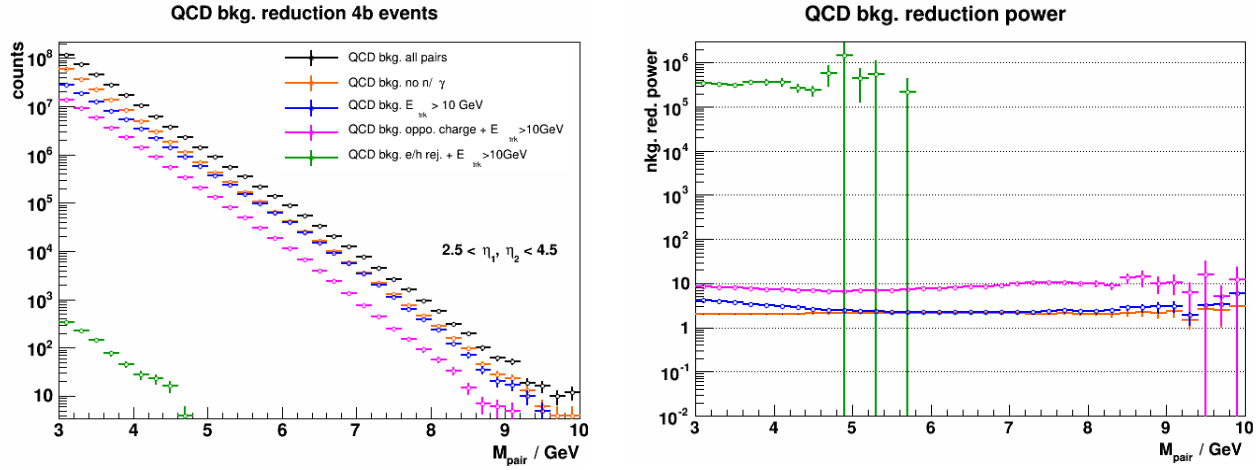

Figure 3-19: QCD background reduction with kinematics cuts and *e/h* rejections

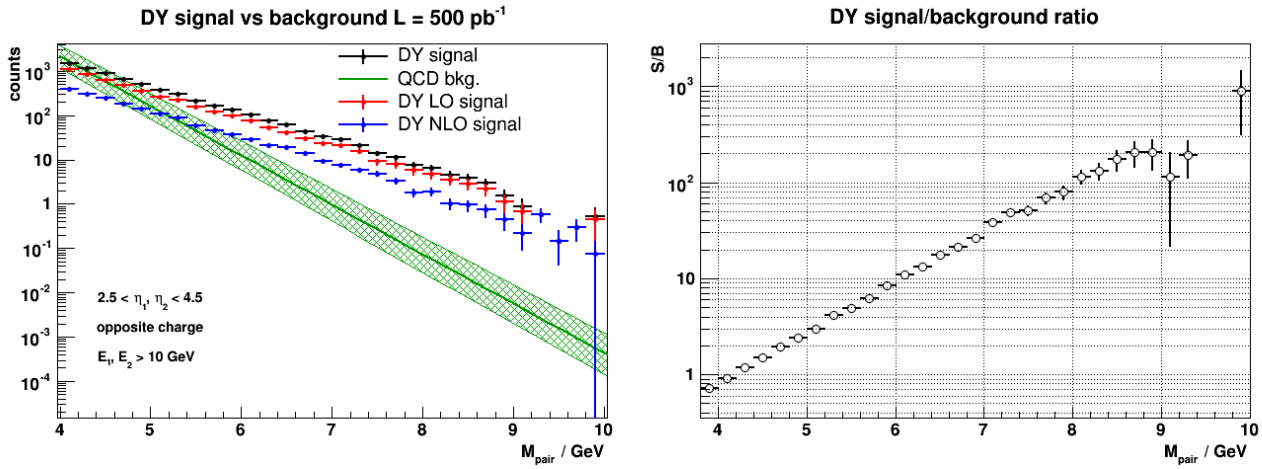

Figure 3-20: DY signal and background yield from 500 pb^{-1} p+p 200 GeV collisions

The final background yields as a function of pair mass were then fit by an exponential function and rescaled to a total luminosity of 500 pb^{-1}. The left panel of Figure 3-20 shows the normalized background yield, along with the expected DY productions. The green band represents the statistical uncertainties of the background yield and its shape. The right panel shows the DY signal to the QCD background ratio as a function of pair mass.

Finally we note that we have only considered the QCD background in the DY signal-to-background ratio presented in this subsection. We expect additional backgrounds from photon conversion from materials. Without a detailed design of the beam pipe and the FTS and its supporting structure, we do not have a reliable GEANT model to simulate the photon conversion background yet. Rough estimates indicate that these additional backgrounds may be on the same order as the QCD background, if care is taken to minimize the materials in the fiducial acceptance of the forward detectors.

3.3 Forward Tracking System

In addition to the Forward Calorimeter System, a Forward Tracking System (FTS) is required for the STAR forward upgrade project. The FTS, aided by the STAR 0.5 T magnetic field, must discriminate the charge sign of tracks for transverse asymmetry studies, and those of dielectron pairs for Drell-Yan measurements. It needs to find primary vertices for tracks and point them towards the calorimeters in order to suppress pile-up events in the anticipated high luminosity collisions, or to select particles from Lambda decays. It should also help with electron and photon identification by providing momentum and track veto information. In studies of heavy ion collisions, it should be able to measure transverse momenta of charged particles in the range of $0.2 < p_T < 2$ GeV/c with 20-30% momentum resolution. In order to keep multiple scattering and photon conversion background under control, the material budget of the FTS has to be small. These requirements present challenges for detector design in terms of position resolution, fast readout, high efficiency, and low material budget.

3.3.1 Silicon-based and Small-Strip Thin Gap Chamber FTS detector simulations

Simulations of a FTS comprised of three Si disks and four small-strip thin gap chambers (sTGC) were performed in the STAR software framework. Particles were thrown uniformly over the acceptance of the detector, in order to estimate the detector performance for various hit densities and various levels of segmentation. For this study, the Si disks were segmented into 12 sectors, each containing 128 divisions in phi and 8 divisions in radius. Each sTGC station was divided into four 60cm square quadrants. Each quadrant consists of two overlapping faces rotated 90 degrees with respect to one another. The first face primarily provides measurement in the local-x direction while the second face provides the measurement in the local-y direction. Each face was subdivided into four columns of 15cm strips. The width of the strips was tuned to approximate the resolution anticipated from the ATLAS test-beam measurements. The Si disks were placed at z = 139.9, 163.2, and 186.5 cm. The sTGC wheels were placed at z = 273, 303, 333 and 363 cm. Figure 3-21 shows the layout of the 7 detector planes, and the resulting hit densities at ~300 tracks/event (which is similar as what we expect in central AuAu collisions at RHIC).

The simulated events were reconstructed by the Stv tracker – a Kalman-filter tracker using a follow-your-nose seed finder. The tracker is permitted to reuse hits during track finding but must uniquely assign hits to tracks before track fitting. Shared hits are assigned to the best track, based on length and chi-squared. Tracks with fewer than 4 hits are eliminated. We will present results from these initial tracking studies.

Figure 3-22 shows the reconstructed Q/p_T distributions for global tracks (red histogram) and primary tracks (blue histogram) for 0.2, 1.0 and 2.0 GeV muons, for 100 pions/event. The charge of both global and primary tracks can be cleanly identified, although at low p_T inclusion of the primary

vertex in the fit becomes important. The dependence of the tracking performance on the track density (logarithm of the number of tracks/event) is shown in Figure 3-23. For up to 100 tracks/event, the tracking efficiency is good (>80%), with adequate tracking efficiency out to ~300 tracks/event. Figure 3-24 and Figure 3-25 show the performance for pions including the charge separation probabilities, momentum resolution and the tracking efficiency from the PYTHIA6 simulated events instead of the single particle generator. In general, the PYTHIA simulated events give a similar and consistent performance as the single particle guns.

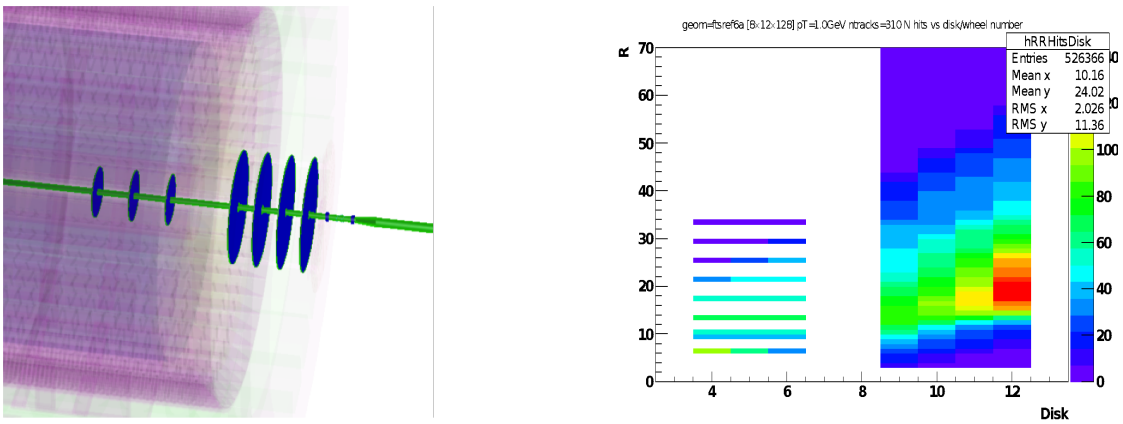

Figure 3-21: The implementation of the different tracking layers along z into STAR (left) and the hit density per tracking layer for tracks with p_T = 1 GeV/c and a total track density of 300 tracks.

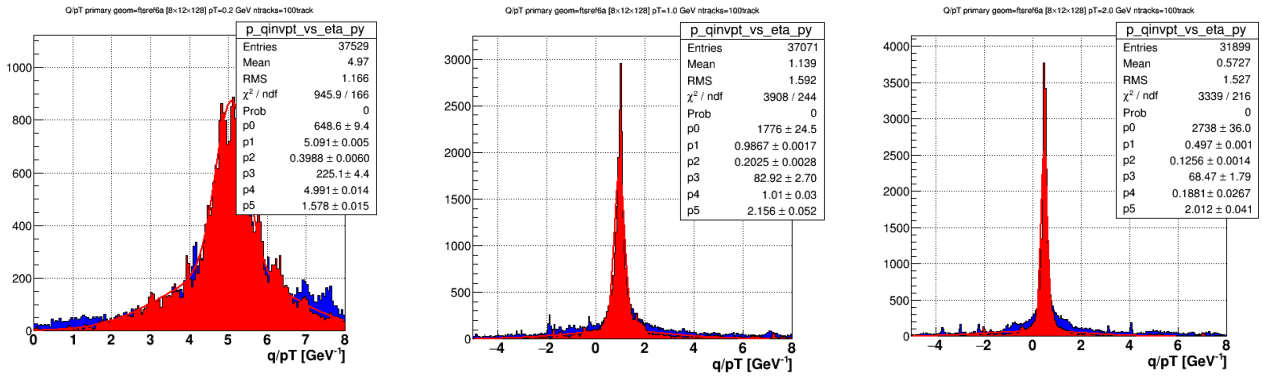

Figure 3-22: The ratio of Q/p_T for a track density of 100 tracks in the rapidity range 2.5 < η < 4 with a p_T of 0.2, 1.0, and 2.0 GeV/c. The fake global tracks are represented by the red histogram and correctly reconstructed primary tracks by the blue histogram.

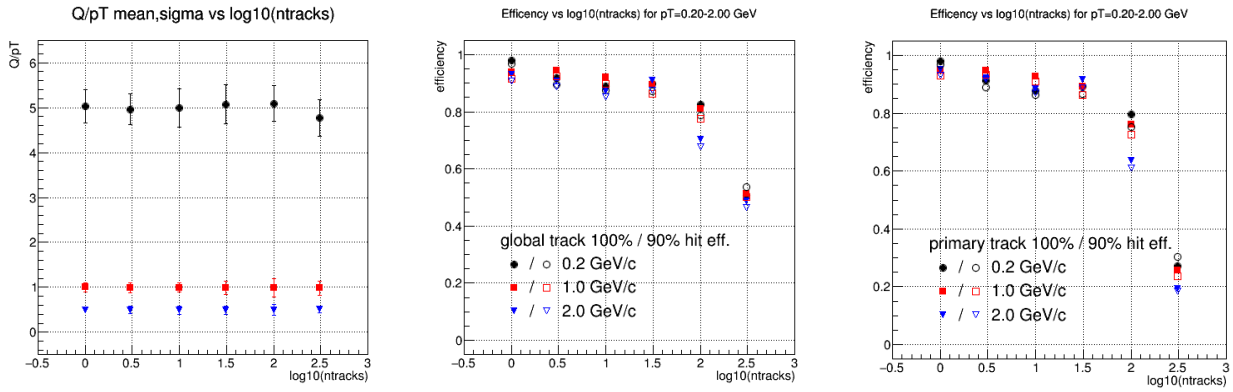

Figure 3-23: Q/p_T, and the tracking efficiency as function of the track density in the rapidity range 2.5 < η < 4 for muons with p_T of 0.2 GeV/c (black), 1 GeV/c (red) and 2 GeV/c (blue).

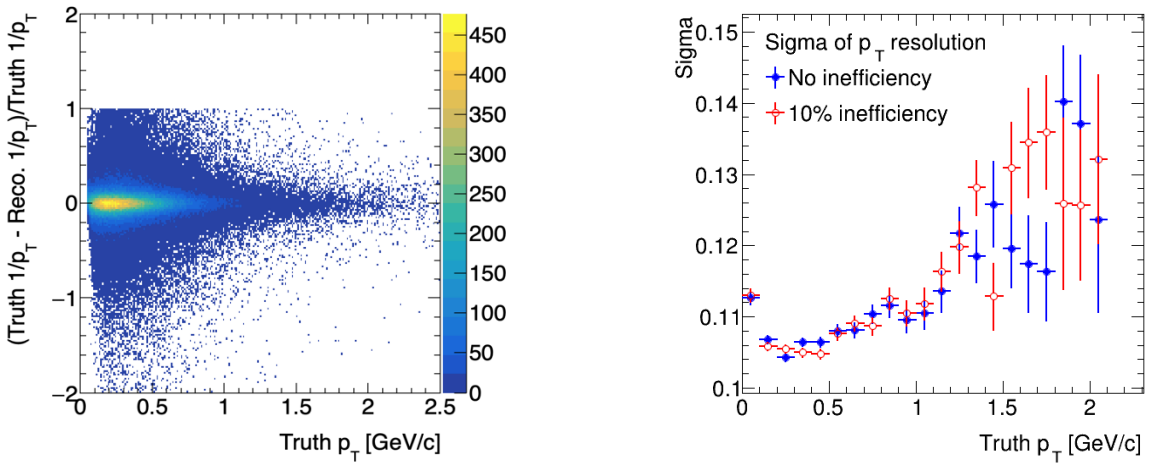

Figure 3-24: The tracking momentum resolution as function of the pT in the rapidity range $2.5 < \eta < 4$ for pions with the PYTHIA6 simulated event.

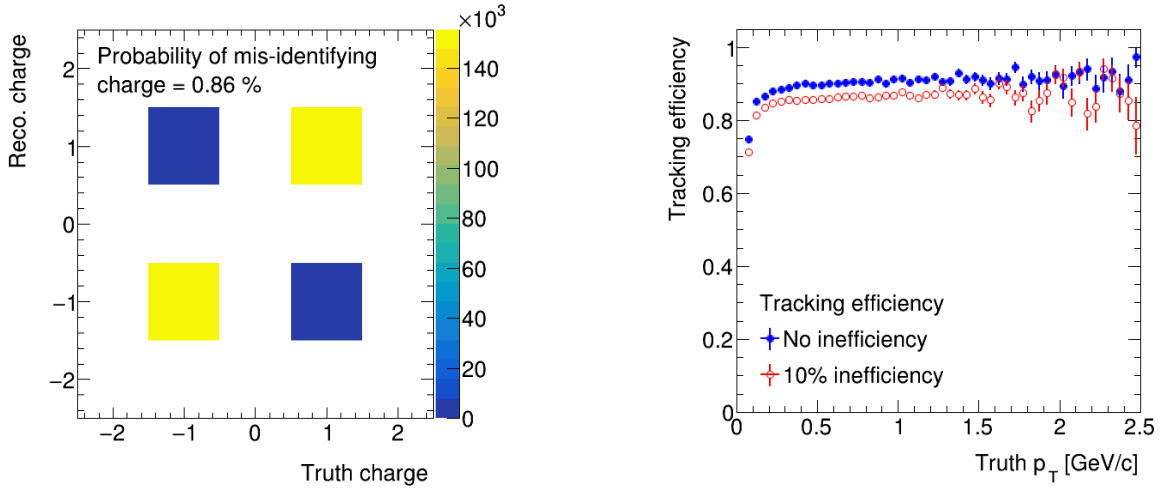

Figure 3-25: The mis-identify probability (left) and tracking efficiency for the charged pion in the rapidity range $2.5 < \eta < 4$ with the PYTHIA6 simulated events.

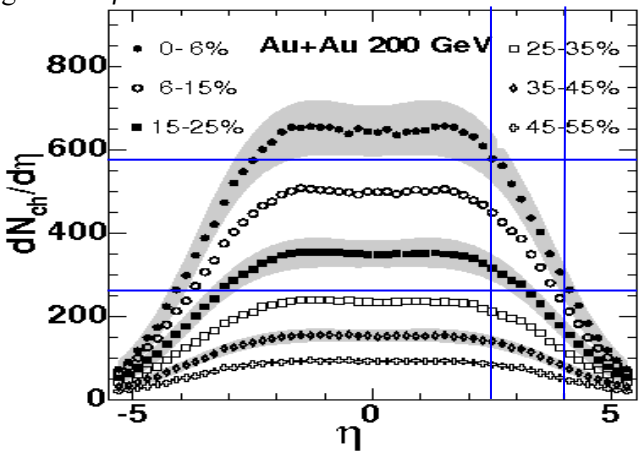

Figure 3-26: The track density / event measured by PHOBOS. The density drops quickly from 600 to 250 tracks for the most central events in the rapidity range $2.5 < \eta < 4$.

We have demonstrated that the tracking performance of the Silicon and sTGC combined setup can achieve efficiencies of 80% out to 100 tracks/event and above 50% at 300 tracks/event. This level of performance satisfies the requirements from both the proton and HIC physics. Figure 3-26 shows the track density measured by PHOBOS. In the 15-25% central collisions, it falls from 300 tracks/event at $\eta = 2.5$ to 150 tracks/event at $\eta = 4.0$.

4 The Forward Calorimeter System

4.1 Introduction

The proposed design of the FCS is a follow-up development of the original FCS system and is driven by cost optimization. The big reduction in cost is achieved by replacing the originally proposed W/ScFi SPACAL ECal with the refurbished PHENIX sampling ECal [129]. In addition, the FSC will utilize the existing Forward Preshower Detector ($2.5 < \eta < 4$) operated in STAR since 2015. The proposed FCS system will have very good electromagnetic (~8%/√(E)) and hadronic (~50%/√(E)+10%) energy resolutions. The FCS consists of 1496 of the 15552 existing PHENIX ECal towers and 520 HCal towers, covering an area of approximately 2.6 m × 2 m. The hadronic calorimeter will be a sandwich iron-scintillator plate sampling type, based on the extensive STAR Forward Upgrade and EIC Calorimeter Consortium R&D. Both calorimeters will share the same cost-effective readout electronics, and SiPMs as photo-sensors. It can operate without shielding in a magnetic field and in a high radiation environment. By design the system is scalable and easily re-configurable. Integration into STAR will require minimal modification of existing infrastructure.

A new method of construction for sandwich hadronic calorimeters was developed during the STAR R&D program. A calorimeter system similar to the FCS is considered as a baseline design in the outgoing hadron region of a dedicated EIC detector.

4.2 Choice of Technology

There are several factors which led us to adopt the technology choice for the proposed FCS. The electromagnetic energy resolution at the level of about 10%/√(E) and hadronic energy resolution at about 50%/√(E)+10% are sufficient to carry out the proposed measurements outlined in previous chapters. The same levels of energy resolution are desired for a future EIC detector as was carefully studied in Ref. 5. For comparison, the best hadronic energy resolution of 44%/√(E) was achieved by the ZEUS collaboration in their compensated uranium sampling calorimeter. Calorimeters in ATLAS and CMS at LHC have hadronic energy resolution > 100%/√(E). To achieve the best hadronic energy resolution (for single hadrons) usually requires a compensated calorimeter system, which was realized in the original FCS design. By constructing the EM section from existing PHENIX EM modules, there is no reason to make the hadronic section from lead, as the whole system is no longer compensated. Targeted energy resolution can be reached by replacing lead with iron in the hadronic section. This solution is cost-effective but will require more complicated procedures for energy reconstruction.

The forward calorimeter system has to be very compact for the STAR forward upgrade. This is required by the configuration of the STAR IP and existing STAR detector. We chose SiPMs as photo-detectors for both EM and HAD sections.

The FCS has to be designed so that the hadronic calorimeter can be assembled in place. The access at the FCS location is limited, with no overhead crane available. Thus, it will be preferable to have the whole detector assembled from relatively light parts *in situ*, preferably by undergraduate and graduate students, who provide important manpower resources in the STAR collaboration.

4.3 Hadronic Section -- Technology and Design

The design of the sampling structure of the HCal is modeled after the ZEUS Pb/Sc compensated prototype, which was the first compensated calorimeter. Mechanically, the HCal section is a stack of layers of absorber and scintillation plates. The easiest way to describe the assembly

process is to imagine building an entire HCal block from LEGO-style parts layer-by-layer. The basic structure of the HCal mechanical prototype is shown in Figure 4-1.

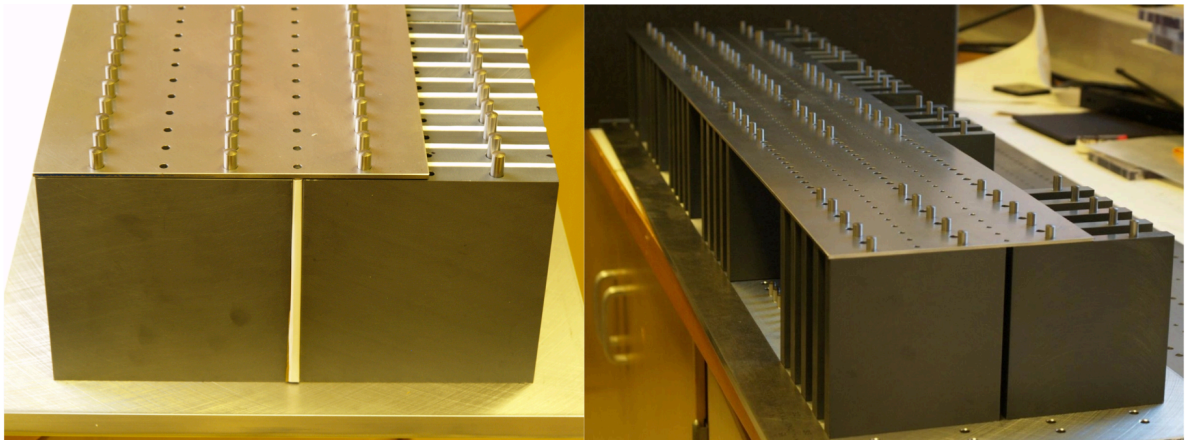

Figure 4-1: LEGO-type HCal mechanical structure. Absorber plates (gray in color) are positioned with the aid of dowel pins. Scintillation and WLS plates (white in color) are inserted in between absorber plates. Steel master plates work as a link between adjacent rows and front-and-back plates of the calorimeter.

Holes in the bottom base plate of the detector provide locations for the absorber plates. Each absorber plate has four holes for dowel pins, two at the bottom and two at the top. Steel dowel pins (5 mm in diameter) position absorber plates with respect to the bottom base and top steel master plates. A single master plate covers one and a half rows of HAD towers, providing interlinks between all absorber plates within one tower, between front and back steel plates of the HAD section, and between adjacent rows of the HAD towers. The iron absorber plates are 20 mm thick, and the gap between two adjacent absorber plates is 3.1 mm. Scintillation plates of thickness 3 mm are placed inside these gaps. There are 38 layers of Fe/Sc in the hadronic section, which is approximately 4.5 interaction lengths. Scintillation light from each tower is collected with a 3 mm thick wavelength shifting (WLS) plate (EJ-280), which is placed in the gap between two adjacent HCal towers. All scintillation and WLS plates are "floating" within each layer (there are no mechanical loads on these elements). Figure 4-2 shows an assembled HCal prototype. We assembled this prototype in place at the FNAL test beam facility in order to validate the construction technique. It took about eight hours for four people to build the sixteen-channel HCal prototype from the individual components at the test beam site. With a reduced number of layers in the proposed FCS, the assembly process will be faster.

The light collection scheme of the original HCal was optimized to provide uniform and efficient light collection from all scintillation tiles along the depth of the HCal tower. All optical connections in the HCal (except for coupling of the silicon photo-multipliers to the WLS) were made through a narrow air gap. We found that a good combination of reflective materials for the WLS plate was a white diffusive reflector (Bicron BC-620) at the far end (from the photo-detector) and aluminized mylar at the back side of the WLS (opposite to the edge of the scintillation tiles). The mylar film also serves as an optical isolator between HCal towers within one layer of the HCal. To achieve uniform light collection (within 10%) along the depth of the HCal tower, we placed a variable density filter printed on a clear mylar sheet inserted between scintillation tiles and the WLS plate. Monte-Carlo calculations show that without such a filter, the energy resolution of the HCal degrades by about factor of two for the energy range above 20 GeV compared to an ideal detector. Variation of light from tile-to-tile in the tower within ±10% has a negligible effect on energy resolution. Bench test measurements also show that variation of the thin air gap between the scintillation tiles and WLS plate (due to mechanical tolerances required for HCal assembly) has a negligible effect on the energy resolution of the detector. We found no degradation in light collection efficiency for unwrapped

scintillation tiles placed between painted absorber plates compared to that for scintillation tiles wrapped with Tyvek.

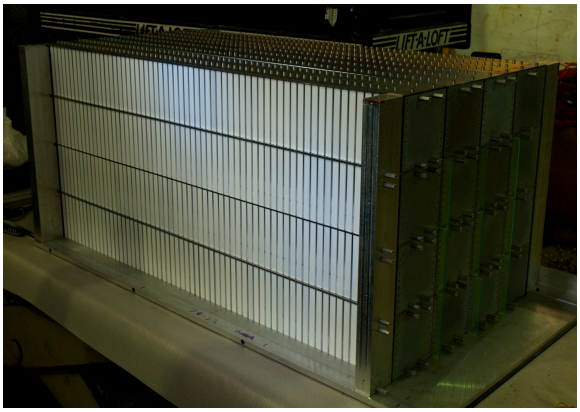

Figure 4-2: A full scale HCal prototype during assembly at the FNAL test run in 2014. The prototype consisted of sixteen individual towers. It was assembled from individual parts directly at the test beam site.

4.4 Photo-sensors and Front-End Electronics

We have developed a new compact readout scheme for the FCS. For both the ECal and HCal sections, we used silicon photo-multipliers (Hamamatsu Multi-Pixel Photon Counters (MPPC) S10931-025p were used in the FANL test run in 2014). They are very compact, fast and insensitive to magnetic fields, and sufficiently radiation hard for FCS readout in STAR [134]. SiPMs do not require HV for operation, which can significantly simplify the readout system. The cost of SiPMs continues to drop, while performance of these devices is becoming better and better for all manufacturers. We are making a second iteration of readout electronics for the re-designed FCS, which were tested during RHIC Run17 at the STAR IP.

In 2016 we tested a PHENIX Shashlyk module in the FNAL test beam. The purpose of this test was to verify energy resolution and to measure the absolute light yield. The measured light yield (with PMTs) was approximately 1000 p.e./GeV, which is more than enough to proceed with SiPM readout.

The frontend electronics for FCS builds on our extensive experience with SiPM readout in STAR and for EIC calorimetry R&D, from the 2014 HCAL R&D, the FMS preshower and postshower detectors, and more recently the Event Plane Detector (EPD) and 2017 test of PHENIX ECAL modules with SiPM readout and DEP at STAR. The common themes have been: Firstly to provide the SiPM's with accurate, high resolution programmable, low noise bias voltage from a low source impedance, for a stable gain independent of the current drawn. Secondly to provide a simple analog temperature monitoring and temperature compensation (with programmable slope) of the bias voltage, again for a stable gain. Thirdly to load the SiPM's with a low input impedance signal chain, to keep the signal pulse is fast and the bias voltage reasonably stable during the pulse (which goes to ensure that all pixels carry the same weight in the signal). Lastly, to have a relatively simple, modular design which is easily integrated at low cost into a large system. This means low power, a multidrop control interface shared on power or signal cables, a robust signal output that can drive cleanly cables of 25 m or more to the digitizer boards, tolerance of input supply variations and noise (including the bias input supply), and so on.

The FCS ECAL frontend board provides readout for four towers of one calorimeter module. It bolts to the front of the module through standoffs and uses spring-loaded contact "pogo" pins to connect to the SiPM carrier boards, one of which is glued to a light guide block on each tower's fiber bundle end. A precision NTC thermistor exists on each SiPM carrier board and is also connected through the pogo pins (thus 4 pins per tower).Signal processing on the frontend board consists of a 16 Ω load resistor, a passive pulse shaper, a programmable (CMOS switched) attenuator for gain

control, and further a 50 Ω input amplifier, shaper, and cable driver circuit. We use relatively low cost, high density differential pair cables for the signal interface to the DEP boards. This innovation was extensively tested and deployed in the FMS postshower and EPD detectors and saves a lot of cable tray space and installation/maintenance effort. The programmable gain control in the FCS FEE board is a new feature introduced for FCS in order to relate precisely the normal operating gain of the readout (with full scale 180 GeV) to an approximately 5x higher gain that suffices to measures the response to vertical cosmics in the installed detector for calibration purposes. It is expected to provide <1% uncertainty on relative gain (after calibration in the FEE board production test setup).

The SiPM bias voltage is regulated per channel with an on-board precision regulator with 14-bit control DAC with a voltage range of 0 to 70 Volts. The regulator will current limit sharply at roughly 800 µA to protect the SiPM's, but below the current limit the output impedance is <150 Ω over all relevant frequencies. Noise of the regulated bias voltage is <1 mV. Temperature compensation is provided per channel, based on that channel's thermistor on the SiPM board; the temperature compensation slope is set in common for all channels by a 12-bit DAC with a range of 0 to +66 mV/°C. The bias voltage regulator works from an external +80 V input that does not require precision regulation.

The current to each SiPM board is monitored and multiplexed to a 16-bit ADC, with range of 0 to 410 µA (in HCAL, 0 to 614 µA). Without calibration, the absolute accuracy of the bias voltage and current monitor are each expected to be 1 – 2 %, however we plan to calibrate them in the production test fixture to have the option of using this calibration in online controls and monitoring in the FCS.

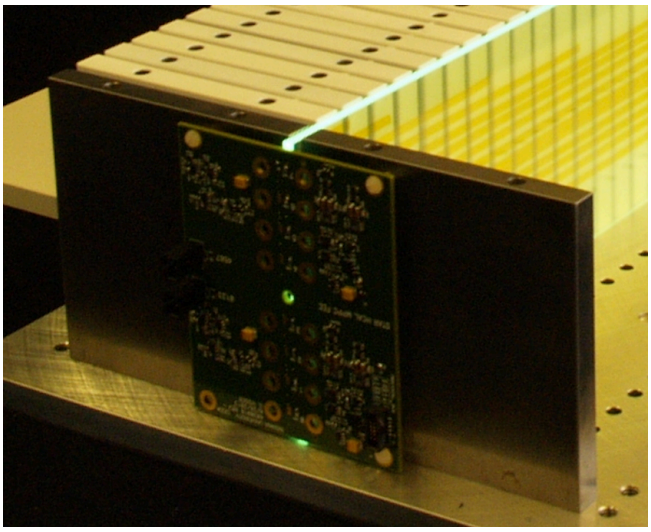

Figure 4-3: HAD FEE attached to a WLS plate during bench tests.

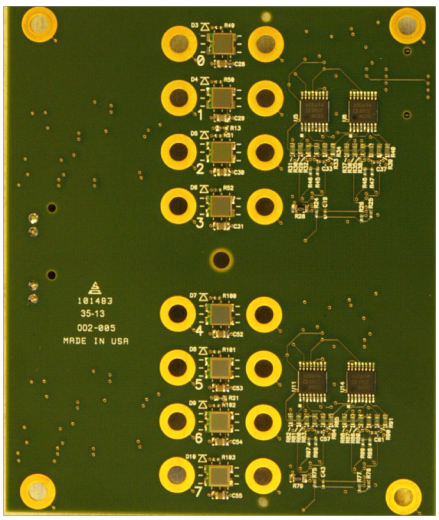

Figure 4-4: HAD FEE Board with 8 SiPMs installed.

The slow controls interface to the FEE board utilizes I^2C, an industry standard although one which is usually deployed only within a single board or box. This has been tested for our purposes in the 2017 ECAL FEE board and at a more realistic large scale proven in the Event Plane Detector. Up to 16 FEE boards can share a common control bus, using an addressable bridge chip on the FEE. The controls master is integrated into the DEP board, and the connections are made using the same cables as are already needed for signals to the DEP and power to the FEE. The master interface on the DEP is opto-isolated to avoid problems from EMI or ground voltage differences. Each FEE board has a serial number chip which can be read and used for calibration lookup, although it is not used for addressing as it was in the FMS preshower and postshower systems. Such "1-wire" controls proved to be too slow.

The FCS HCAL frontend board is a two tower board rather than four, and connects to its two mating SiPM carriers by short (~3 cm) cables. The gain will be set slightly different. Apart from these things the design is absolutely identical to the ECAL frontend board. A photo of the 2017 ECAL FEE board is seen in Figure 4-5, and the 2014 HCAL FEE installed on the HCAL in Figure 4-3 (although the new HCAL FEE is significantly different both mechanically and electrically).

Indiana University will design and (with vendors) produce the FEE boards, and develop the specifications and production test system. University of Kentucky in collaboration with Indiana University will handle the production test and future maintenance of the FEE. We intend to fully involve students in the production test and FEE installation work, it is an excellent learning opportunity for hardware skills, and student's efforts an invaluable resource for the project.

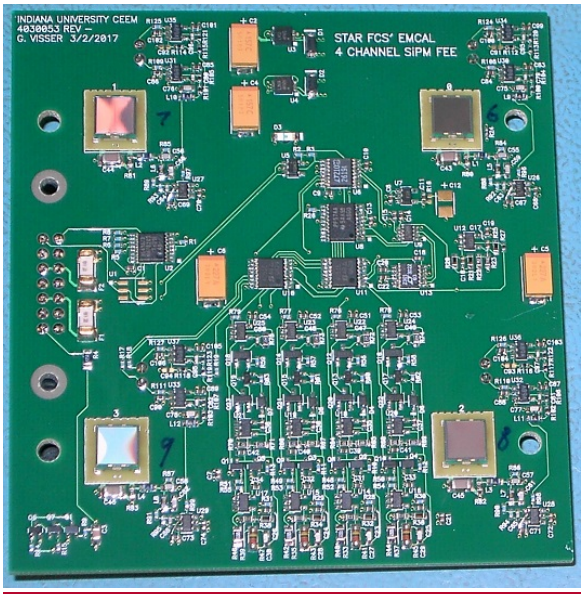

Figure 4-5: 2017 FEE board for PHENIX ECAL at STAR. The four SiPM's are seen on small carrier boards that mount on this FEE.

4.5 Performance of the FCS in the Test Run at FNAL in 2014

We tested the response of the FCS prototype to hadrons, electrons, and muons in the energy range 3-32 GeV at FNAL. Electrons were identified with a differential Cerenkov counter (standard equipment at the Muon Test Beam Facility, MTBF). Impact position was defined by a scintillator XY hodoscope (4.9 mm wide scintillator square rods with readout by SENSL SiPMTs). We minimized the amount of material upstream of the calorimeters in the beam line to about 4 cm of scintillation counters. Additionally, MTBF personnel installed He-filled beam pipes between our apparatus and the upstream Cherenkov counter. The initial setup of our apparatus in the beam line is shown in Figure 4-5. Two MTBF MWPCs (one is seen in Figure 4-5) were used as additional monitoring devices during the beam energy scans to track reproducibility of the beam settings at different energies. The HCal was oriented with a fixed angle of 2.5 degrees between the beam and the primary axis of the HCal towers. The ECal prototype was attached to the front steel plate of the HCal. The angle between the axis of the ECal towers and beam was kept at 4 degrees. All channels of the FCS were equipped with an LED monitoring system. Events for LED monitoring signals and pedestals were continuously recorded at a rate of about 1 Hz during most of the test run. Preliminary analysis of these data showed that stability of the gain for HCal and ECal front-end electronics was better than 1% during a typical twelve-hour shift of data-taking. All SiPM's were tested and calibrated with a laser system prior to the test run. With this system, we verified that the response of the MPPC assemblies for both the HCal and ECal prototypes were set equal to within 1%. We found that no additional tower-by-tower calibration of the ECal prototype with the beam was required. This was expected based on our

previous beam test results in 2012, when we measured excellent internal homogeneity for the ECal modules built with our construction technique.

The HCal required additional tower-by-tower calibrations with MIPs. For that, an absorber was inserted into the beam line (8 GeV muon mode for the MT6 test line). A MIP peak was selected in each HCal tower using an isolation requirement: a single muon hit in a tower, with no other energy deposition in the rest of the HCal. For calibrations with MIPs, the ECal prototype was removed from the beam line. We found that large corrections (~20%) were needed in addition to the calibrations made prior to the test run. About 10% of this shift can be explained by the alignment of the WLS plate and the MPPCs: both have a 3 mm active area, and about 250 microns misalignment is possible due to positioning of the MPPCs on the FEE board). The rest can be attributed to the quality of optical components. One possible source is variations in the response of the WLS tiles used in different HCal towers. The concentration of dopants and attenuation length have not been measured for every WLS tile used in the HCal, and they were all assumed to be identical.

The response of the FCS prototype module to hadrons is illustrated in Figure 4-6. In an ideal, fully compensated calorimeter detector, the reconstructed energy of the incoming hadron is a simple sum of the energy deposited in the ECal and HCal sections (assuming that the responses in both sections are equalized and energy-independent). To obtain the best energy resolution for hadrons in the FCS prototype module, we found that the weighting factor for the ECal section should be energy-dependent. The factor changes from about 2 at a beam energy of 3 GeV, to 1.2 at 20 GeV, then stays approximately flat above 20 GeV. With this energy-dependent weighting of the ECal energy, we measured the *e*/*h* ratio for the FCS prototype module to be close to 0.95, and almost constant above 10 GeV.

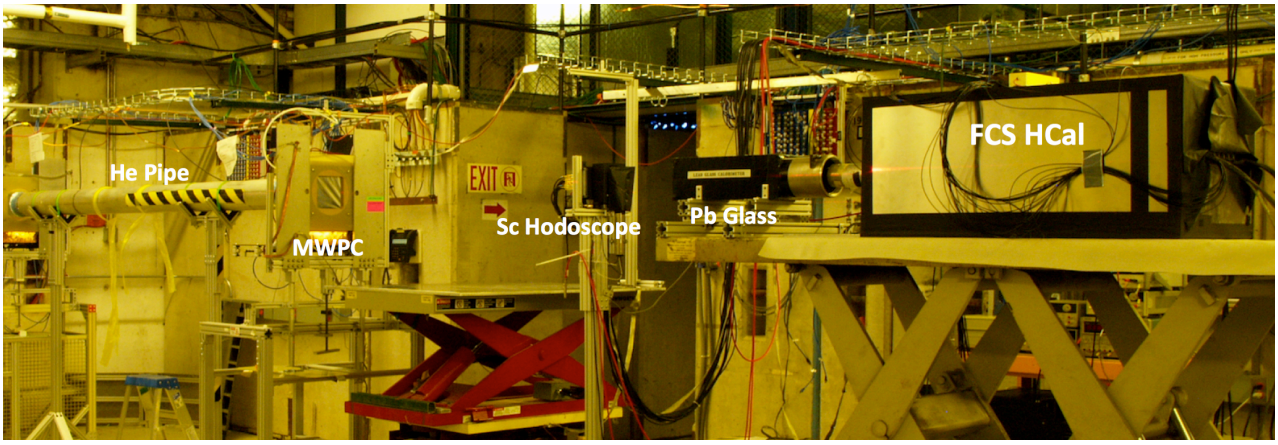

Figure 4-6: FCS prototype at the beam line. The Pb-glass calorimeter in front of the HCal section was used for initial beam studies.

We did not perform any corrections due to leakages in the transverse and longitudinal directions in the FCS prototype module. Qualitatively, this result is close to MC predictions; however, in our MC model we did not include some of the structural elements between the ECal and HCal sections, or account for the limited size of the prototype tested at FNAL. The questions of optimal weighting factor and the final expected *e*/*h* ratio in the FCS prototype module, will need to be clarified with a MC model of the exact geometry of the detector that was used in the test run.

The response of the FCS prototype module to electrons is illustrated in Figure 4-7. Due to non-uniform light collection with MPPCs, the response of the ECal section depends on the impact position. We corrected the energy deposition in the ECal section according to impact position and restricted the impact area only to the circle with a diameter of 1.4 cm at the center of the ECal tower.

Local coordinates of the impact positions were determined using calorimeter information only. We used a logarithmic weighting method with the cut-off parameter set at 3.8. The difference

in the shapes of the responses of the ECal section in the X and Y directions is due to a tilt of the ECal prototype of 4 degrees around the Y-axis.

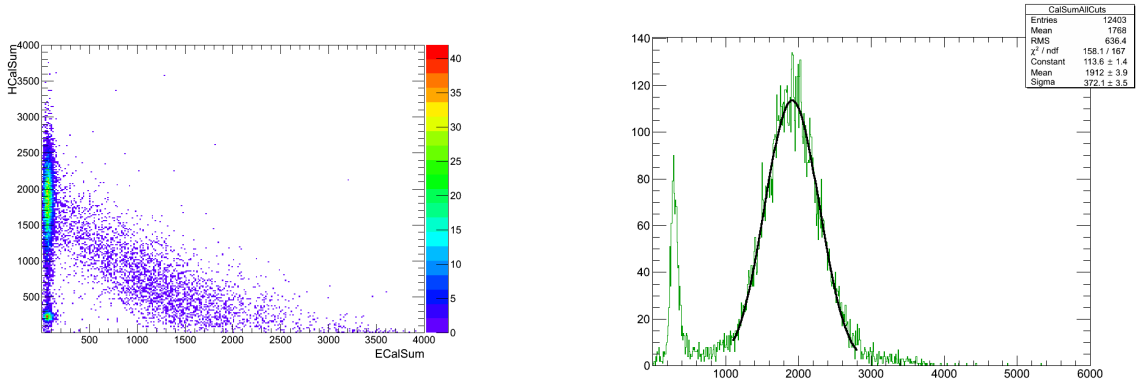

Figure 4-7: Response of the FCS prototype module to hadrons. (*left*) Energy deposition in an HCal section (Y-axis) versus energy deposition in ECal section (X-axis) for 12 GeV hadrons. (*right*) A weighted sum of the energy deposited in ECal and HCal section for 12 GeV hadrons.

The performance of the FCS prototype module during the beam test in 2014 is summarized in Figure 4-8. The response to electrons is approximately linear, while the response to hadrons shows clear deviations from linearity above 15 GeV. The most likely reasons for this deviation are the weighting procedure of the fraction of energy deposited in the ECal section and leakages from the FCS prototype module. We tested the HCal section alone (with ECal section removed from the beam line) and did not observe a similar deviation from linearity in this energy range. The energy resolution of the FCS prototype module for hadrons, shown in Figure 4-8, is about 15% worse compared to MC predictions for the FCS module at 10 GeV. One of the reasons is likely the transverse leakage from the FCS prototype module, which was not taken into account for the test beam results. We also note that the energy resolution of the FCS in the MC simulation depends on the physics list used in GEANT4. We used a LHEP physics list, which, in our studies, provides the most accurate description of the FCS performance. The electromagnetic energy resolution of the FCS prototype module is close to MC predictions. There are two fits to our experimental results shown in Figure 4-8. One assumed that the momentum spread of the beam is zero. In this case the stochastic term is close to 10% and the constant term is 1.7%. If we use our earlier (2012) estimates for the momentum spread of the beam to be 2.7 % below 4 GeV and 2.3% above 4 GeV, then the stochastic term becomes 11% and constant term is close to zero.

The absolute light yield measured in the ECal section is about 400 pixels/GeV, with the front face of the ECal prototype painted with the white diffusive paint BC-620. The measured absolute light yield for the HCal section is about 130 pixels/GeV. MPPCs for both ECal and HCal sections should behave almost linearly with these light yields for the energy range used in the test run.

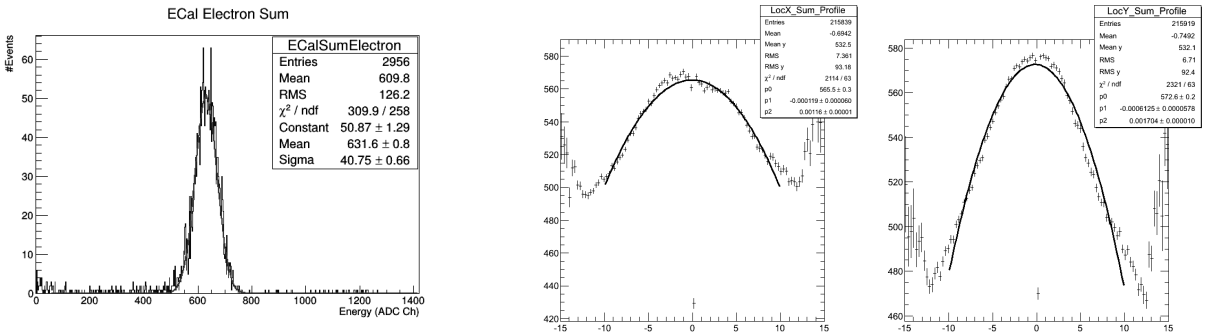

Figure 4-8: Response of the FCS ECal prototype module to electrons. (*left*) Energy deposition in the ECal section for 4 GeV electrons, with the impact point restricted by the scintillation hodoscope to an area of 5

mm x 5 mm. The energies deposited in the ECal section are shown as a function of impact positions in the local X coordinate (*center*) and local Y coordinate (*right*).

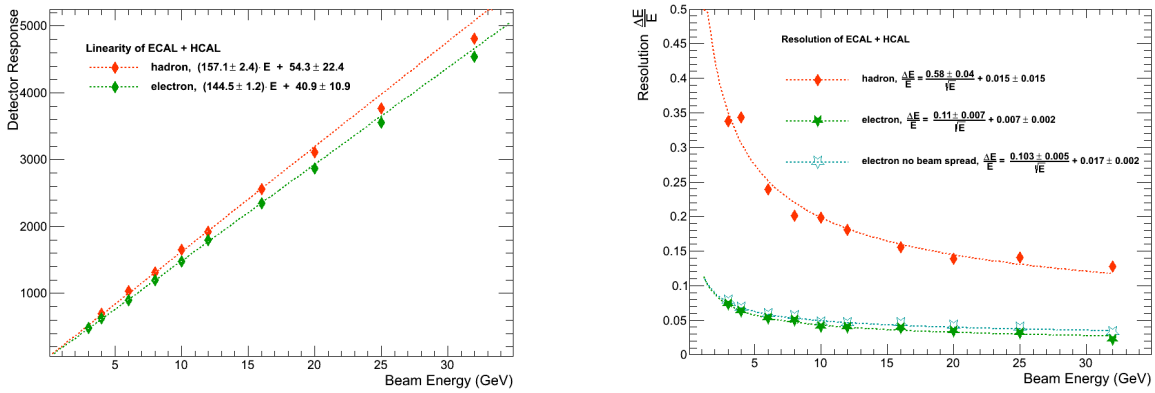

Figure 4-9: (*left*) Responses of the FCS prototype module to electrons and hadrons versus energy. (right) Energy resolution of the FCS prototype module for hadrons and electrons versus energy.

4.6 Summary of Technology Development for FCS

We have developed a new construction technique for a high-resolution lead scintillation tile hadronic calorimeter. The original FCS system with ECal and HCal sections was designed for the STAR forward upgrade and for the Backward calorimeter system for EIC. The performance of the FCS system from the test run data met both STAR and EIC expectations. The novel compact readout scheme based on SiPM readout works well for the FCS prototype. The re-designed FCS based on extensive R&D we performed for the STAR forward upgrade and continuing efforts for EIC calorimetry R&D was described above.

4.7 Mechanical Integration into STAR

Both the ECAL and HCAL will reside on the West Platform (used previously for the FMS detector) and the West Alcove (on top of existing Concrete Structure) in the STAR Experimental Hall. The ECAL is about 10 tons in weight (same as FMS) whereas the HCAL weighs about 40 tons.

For the ECAL installation we will use the existing FMS rails and roller arrangement. The plate on top of the rollers will have to be modified (shortened). The ECAL modules will be stacked on top of this plate.

The HCAL will be sitting on top of the cavity in the west wall. Currently, there exists a 1" thick plate on top of the cavity to support the weight of an ion pump. This plate is covering the existing wall cavity, but does not have enough structural strength to bear the load of the HCAL detector on its own. This requires to design and develop a support structure for the plate from underneath. Such the load can be transferred to the concrete structure of the wall. The plan is to design and build a structure from vertical support beams. Since the HCAL detector will have to be moved to allow for maintenance of the ion pump and cryostat, a rail and roller arrangement similar to the one of the FMS detector will be also built for the HCAL. All these details are shown in Figure 4-10. A Preshower detector will be mounted in front of ECAL using the existing structure of the FMS Preshower with small modifications.

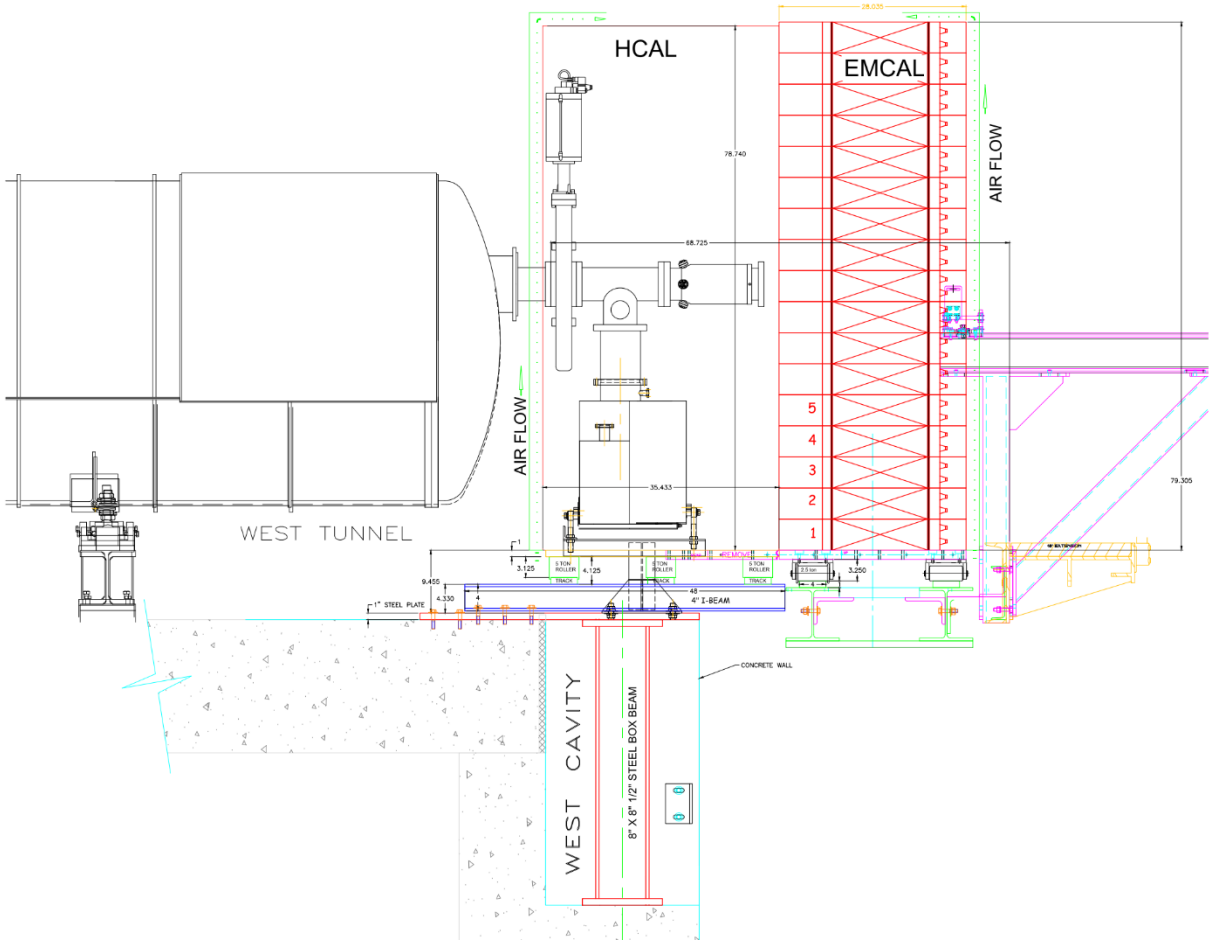

Figure 4-10: Design and Layout of the ECal and HCal on the West Platform of STAR

4.8 Production Plan

The design of the HAD section of the FCS has relied on existing standard technological processes to produce all major components of the detector in industry. Delivery schedule and production capabilities were discussed with companies used for production of components for the full-scale prototype. We do not anticipate any technical or schedule risks associated with production of components for HAD section. Components are trivial to produce and, if needed, it will be easy to run parallel production in few shops (by design there are no interdependencies in the HAD components). The slowest components to produce are scintillation tiles, which has to be cut from larger sheets produced by Eljen Technologies. This trivial, but slow operation will be spread among three or, if needed, four universities shops (Ohio University, ACU, Rutgers) that performed similar tasks in recent past (i.e. all aspects of handling, machining of plastic scintillator materials are known to them). All scintillation tiles for two FCS HAD prototypes were produced in such way. Initially, we planned to produce scintillation tiles for the final detector by injection molding at IHEP (Russia). However, at this time, risk with production of scintillation tiles in Russia outweighs significant cost benefits provided by injection molding technology. For this reason we decided to proceed with scintillation tile production same way we built two full scale HAD prototypes. University groups involved in this project will carry out QA for HCAL components, tests and calibration of the FEEs and SiPMs. The project team will perform the final assembly of the detector in place at BNL, with

help from the STAR technical support group. The STAR technical support group will be responsible for modification of the existing FMS platform.

4.9 Additional R&D

During 2016, 2017 and 2018 R&D program (funded by EIC R&D) we did comprehensive study of SiPM performance in realistic experimental conditions for FCS, which is also expected to be similar for future EIC forward calorimeter system. In 2014 we reported measurements of thermal neutron fluxes at different locations in the STAR experimental hall during RHIC Run 13 with proton–proton collisions at $\sqrt{s}$ = 510 GeV. We compared these measurements to calculations based on PYTHIA as a minimum-bias event generator, using a detailed GEANT3 simulation of the STAR detector and experimental hall, and with GCALOR as the neutron transport code. Fairly good agreement (factor of two) was found between simulation and measurements. Thus we demonstrated that it is possible to do a reliable estimate of the neutron fluxes in the STAR detector. Additional insight into SiPM damage was gained during operation of the Forward Preshower detector (FPS) at STAR in 2015-2016. We observed no degradation of gain, and an increase in leakage current in accordance with calculated neutron fluences at the location of the FPS. We also proved that SiPMs are insensitive to nuclear counting effects unlike APDs, by triggering one of the EIC R&D prototype located at STAR IP equipped with both type of sensors.

In 2017 large sample of SiPMs were exposed during $\sqrt{s}$ = 510 GeV Run 17 at locations spanning FCS acceptance. The main conclusions from these studies were:

- SiPM response will degrade up to 10% during one $\sqrt{s}$ = 510 GeV Run.
- Every SiPM degrades differently.
- Reason for degradation is shift in breakdown voltage.

The first two findings from this studies were very concerning, because it significantly complicates triggering with FCS and requires very good monitoring system. Reasons for shift in breakdown voltage were not immediately clear. Additional studies of SiPM behavior in the STAR experiment were performed during Run 18, however exposure was very low and no significant changes in performance were observed.

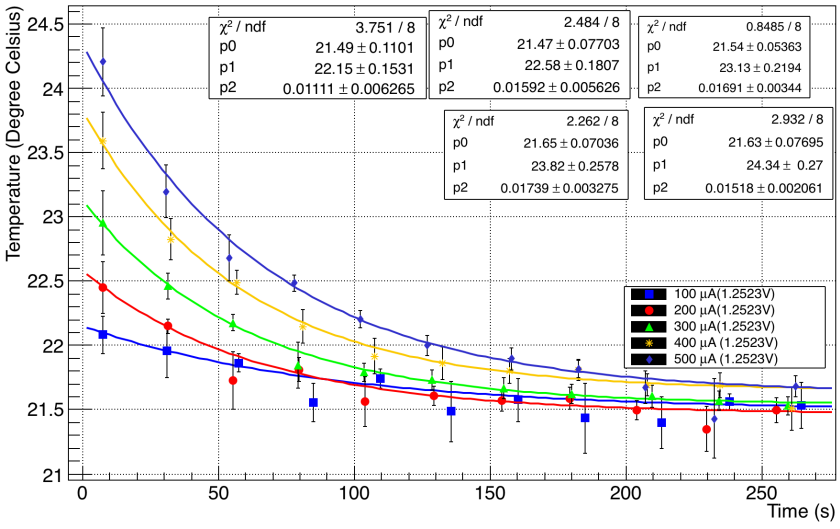

Figure 4-11: Temperature of avalanche region vs time.

In summer 2018 (funder by EIC R&D) we developed two methods to further quantify effects of SiPM degradation observed in Run17. In particular, we developed technique to measure changes in the temperature of the avalanche region of the SiPMs due to increased leakage current, this required developing fast method to measure breakdown voltage. In both methods, SiPM initially was 'heated

up' by external LED (current flowing through SiPM mimics different exposure levels at experiment), then this external LED switched Off and with a dimmed light breakdown voltage or response then measured during next few minutes once avalanche region of SiPM starts to cool down. Figure 4-11 shows fits of temperature of avalanche region vs time with Newton's low of cooling for different initial conditions of the SiPM. For example, for FCS, for this type of SiPMs (S12572-025P sensors) we expect highest combined current in one sensors will be about 100 uA at the end of one 500 GeV run, which will lead to increased temperature on junction of about 0.6 degrees C above ambient, which in turn leads to decrease in response to about 10%, which was observed in Run17.

This and direct measurement of changes in response with time following same scheme (heating/cooling) explained first and third effects observed in Run17. A differential degradation of response from sensor to sensor may be explained by the different overvoltage required to achieve same response for different sensors, which was measured in the past for vary large sample by GlueX, confirmed by our own measurements as well. Since the heat generated in avalanche region is proportional to overvoltage different sensors will have different change in temperature of avalanche region even if the leakage current will be similar. Thus, all effects observed in Run17 were understood.

For FCS changes to 15um S12572 sensors significantly reduces effects of radiation damages on performance of the system, because of smaller gain of 15um sensors compare to 25um sensors, which leads to a lower leakage current with the exposure. It is also clear how to further minimize radiation damages effects by appropriate setting of operation voltages for SiPMs.

In early summer 2018 HPK provided to us samples of new type of wide dynamic range SiPMs they were developing last two years. We fully characterize eight sensors we got, and then with the help from our BNL EIC R&D colleagues got them exposed to about $7*10^{10}$ n/cm^2 in early fall. The main findings from these studies are:

- Temperature dependence of new SiPMs improved (~40 mV/C compare to ~ 60 mV/C).
- Response degradation for FCS in one run can be kept at 1% level.

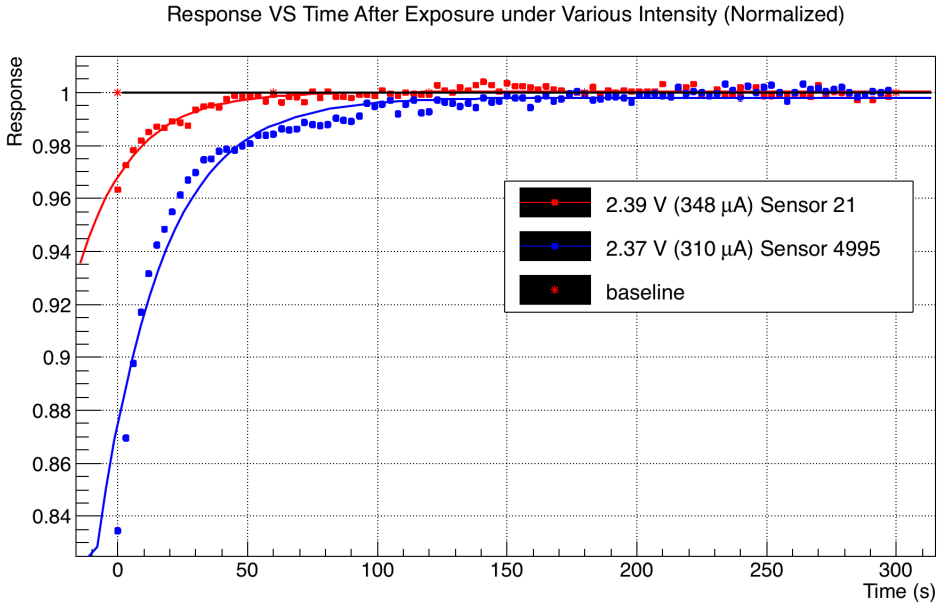

Figure 4-12 Comparison of response degradation for old (blue) and improved (red) HPK sensors

Figure 4-12 shows direct comparison of response degradation for old (Run 17) SiPMs vs new version of SiPM released by HPK (S14160-015P). Leakage current for new sensors irradiated to $7*10^{10}$ n/cm^2 reaches ~ 300 uA, with bias set at ~ 4.25V above breakdown voltage. By setting bias at ~ 2.75V above breakdown leakage current will be ~ 100 uA. The new sensors were greatly improved compare to previous generation of HPK SiPMs.

The highest current expected for FCS will reach ~ 100uA in one 500 GeV Run. With the new sensors (cost is only slightly higher compare to older versions, new sensors quoted $8.9/ SiPM for 10k units) there are no major concerns of impact on FCS functionality due to radiation damages of SiPMs, response degradation will be within ~1% level. This is also true for the older version (15 um pixel size) sensors with appropriate setting of operation voltage.

The effect of increased noise on resolution was measured for both EM and HAD section directly using cosmic muons and sensors exposed during Run17. Effect is small in both cases, for example for HAD section expected resolution at 100 GeV is about 8 GeV, equivalent noise due to radiation damages is ~0.4 GeV (cluster 4 x 4 HAD towers).

As a consequence, requirements for monitoring system can be greatly relaxed, since it will be no longer needed for adjustments of 'gain' with time, but serves mostly as auxiliary system for initial commissioning of the system (with simple design of the monitoring system for FCS we probably still be able to keep 1% monitoring for EM section, with some additional efforts same level can be achieved for HAD section).

To conclude, multi-year R&D program, funded mostly by EIC R&D, give us very good understanding of performance of SiPMs in realistic experimental conditions for FCS and future forward calorimeters systems at EIC. The major concerns after Run17 exposure were relieved by understanding of mechanism of degradation of response and clear guidance how effects of the radiation damages on performance of FCS can be reduced. The development of new SiPM sensors by HPK further reduces concerns of performance of FCS.

4.10 Overview: FCS Electronics Digitizers & Trigger Processors

The FCS electronics system includes trigger, readout of SiPMs, a low-voltage system for SiPMs, low voltage power, slow control functions, calibration and monitoring controls, and interfaces to the STAR trigger, DAQ and slow controls systems. The bulk of the front-end electronics functionality, including signal processing, digitization, buffering, and the formation of trigger primitives, will be carried out by the STAR DEP/ADC board

The STAR BNL Electronics Group proposed to design and build a generic digitizer system ("Detector Electronics Platform" or DEP) which would be cheap, fast and modular, and could be used for many different applications within STAR and its upgrades. It may also serve as a platform for future readout systems at EIC. The basic board would consist of 32 12-bit ADCs running in sampling mode at 8x the RHIC clock. The ADC would be followed by a fast FPGA capable of running various digital filters and other typical trigger algorithms, such as pedestal subtraction, zero suppression, charge integration, moderate timing information (< 1 ns), highest-tower, tower sums, etc. The system will be capable of connecting up to 5 such boards (for a total of 160 channels) into a compact and cost-effective chassis. The data will be sent to a DAQ PC over a fast optical link, and will have sufficient bandwidth to work in full streaming mode for typical occupancies, if so desired. It would also house the STAR TCD interface for the RHIC clock and Trigger command, which could also act as a Slow Controls Interface if needed.

A modification of the basic DEP board (called "DEP/IO") would also be designed by replacing the 32 ADC channels with simple serial differential links. This flavor will act as the main building block for later stages of the FCS-based trigger. The last stage of the trigger will additionally provide a "STAR-standard" interface to the STAR Trigger DSM boards.

Prototypes of the 16-channel digitizer DEP board as well as 2 FCS FEE prototypes (each with 4 channels) were installed in STAR for the FY17 physics proton-proton at 500 GeV/c run and connected to 8 SiPMs. The system was successfully commissioned and is running continuously in STAR controlled by STAR's Run Control as well as STAR's Trigger system & Clock Distribution network Figure 4-14 shows 4 example events for 4 different channels showing the digitized output from the SiPM and FEE cards. The Gaussian fits to the shaped digitized FEE outputs show excellent agreement with the expected response. The abscissa shows the ADC clock (which is 8x the RHIC

clock or 13.3 ns). The width of the pulse from the shaper is thus 50ns, as expected. Note also pulses from other collision crossings.

At the same time the timing information for each event was extracted relative to the RHIC clock edge and is shown in Figure 4-13 below. The resulting width of 3ns is a convolution of the RHIC collision ("diamond") width in time as well as time-of-flight of particles hitting the FCS prototype and is as expected. The prototype 16-channel DEP board is shown in Figure 4-15.

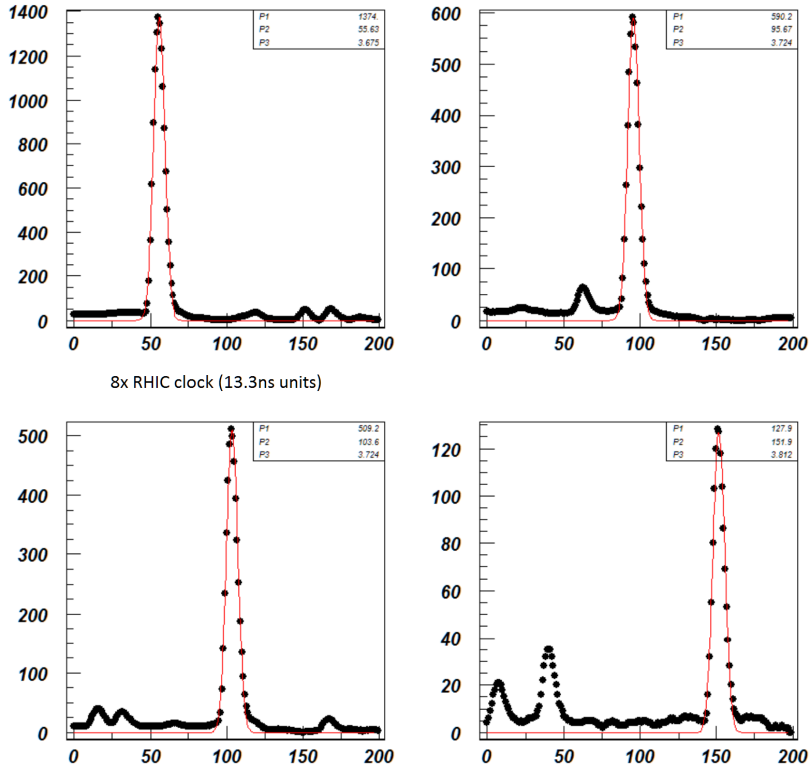

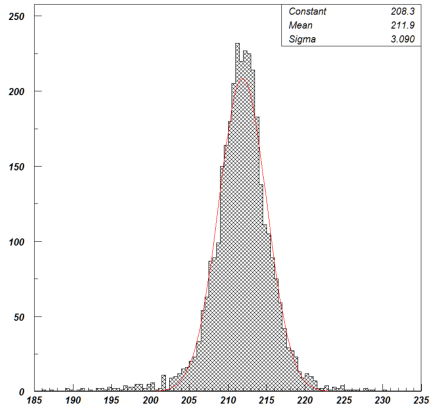

Figure 4-13: Distribution of arrival times of particles relative to the RHIC clock (in ns)

Figure 4-14: ADC output for 4 different DEP channels

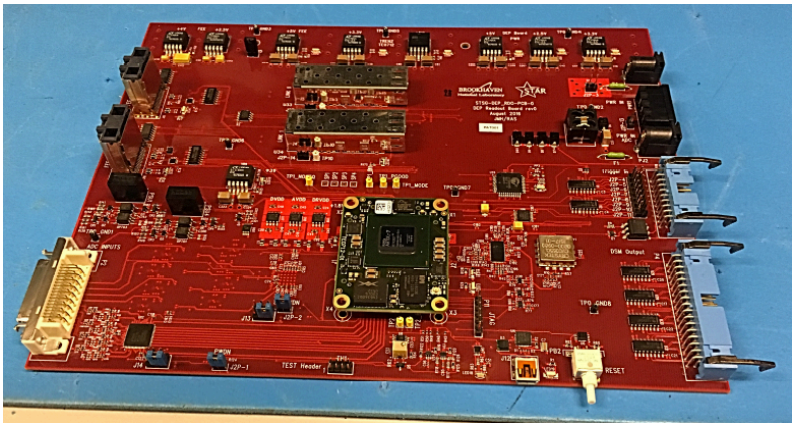

Figure 4-15: First prototype of the DEP board.

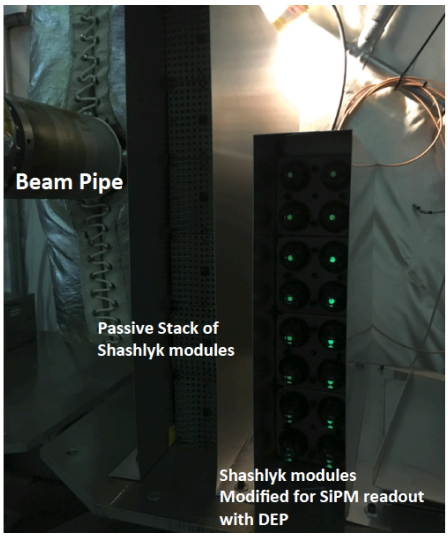

Figure 4-16: Stacks of Shashlik blocks at the East side of STAR.

4.11 Trigger System

The trigger system for the Forward Calorimeter System will consist of layers of DEP/ADC and DEP/IO logic in a tree structure. A DEP/ADC board can send 64 bits of information for every RHIC bunch crossing, or every 107 nanoseconds, to another DEP/ADC or DEP/IO board by serialized FPGA to FPGA communication through a wired connection. A DEP/IO board can receive up to 34 such connections to gather over 2000 bits of information from the ECal, HCal and Pre-shower detectors in a modern FPGA, which will enable complex triggers using correlated information from all three FCS subsystems.

This trigger system using the new DEP/IO board is architecturally similar to the current trigger for the FMS. The FMS trigger consists of initial logic performed in the QT boards that digitize the analog signals for every bunch crossing. The QT boards are followed by a three-layer tree of Data Storage and Manipulation (DSM) boards, each of which receives 128 input bits every bunch crossing, processes them through an FPGA, then outputs the 32-bit result. For the Forward Calorimeter System, DEP/ADC boards will implement the functions currently performed in the QT boards. The existing FMS DSM boards could, in principle, handle the trigger processing for the electromagnetic calorimeter. However, there are several problems with that approach. The much smaller number of input bits per board would severely limit our ability to utilize geometric correlations in the hit information from the ECal, HCal, and Pre-shower. The DSM boards were designed and built in the mid 1990's. Critical components are no longer commercially available. The vintage-1990's FPGAs are barely capable of performing the much simpler FMS logic in the time available. Likely, they are incapable of performing the more complex logic required to merge the ECal, HCal and Pre-shower information together. Furthermore, there aren't enough DSM boards available to instrument the full ECal+HCal+Pre-shower system. For these reasons, we plan to replace the DSM boards with the new DEP/IO logic board that will provide far more input bits and includes a modern, faster, more capable FPGA. The full trigger system is expected to require 74 DEP/ADC boards (which also serve to digitize all the data from the ECal, HCal, and Pre-shower detectors) and 3 DEP/IO boards, plus spares.

The first layer will consist of the DEP/ADC boards that digitize the signals from the ECal, HCal, and Pre-shower detector. Each DEP/ADC board has 32 channels of 12-bit ADCs. An FPGA on each DEP/ADC board will perform pedestal subtraction and gain corrections for the 32 input ADC channels. For the ECal and HCal, each DEP/ADC board that contributes to the trigger will receive signals from 32 contiguous towers, calculate eight sums of (non-overlapping) 2x2 tower groups, and send those sums to the 2nd layer. For the Pre-shower detector, it will send hit map information to the next layer.

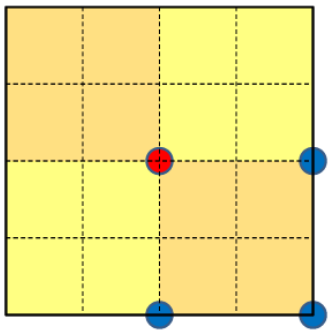

Figure 4-17: This shows a 4x4 HCal trigger patch, created by adding four 2x2 tower sums together. If the center of a non-zero ECal trigger patch projects within the lower-right orange 2x2 sum, the single-particle trigger algorithm matches it either to this patch, with the red dot at the center, or to one of the three overlapping HCal patches that are centered at the blue dots and share the lower-right orange 2x2 sum, whichever contains the most energy (or transverse energy).

The 2nd layer will consist of two DEP/IO boards, one for the north detector and another for the south detector. Each 2nd layer DEP/IO will receive the 2x2 sums and hit map information from 20 ECal, 8 HCal and 4 Pre-shower DEP/ADC boards. Using the 2x2 sums of calorimeter towers, it will form overlapping sums of 4x4 tower groups, referred to as "trigger patches" separately in the ECal and HCal. An electron or hadron trigger will require correlated trigger patch hits in the ECal and HCal, as described below, with a response of more than ½ MIP at the corresponding location in at

least two of the three Pre-shower layers. A photon trigger will require the same electromagnetic signature in the ECal and HCal as an electron trigger, but without the Pre-shower coincidence. For a jet trigger, overlapping large-area transverse energy sums, each spanning approximately ¼ of the detector and summing contributions from both the ECal and HCal, will be used.

The 3rd layer will consist of a DEP/IO board that receives geometrically grouped electron and jet triggers and threshold bits for single electron, photon, jet and hadron triggers from the two 2nd layer DEP/IO boards. A coincidence of two appropriately separated electron triggers will be used to trigger on e^+e^- pairs from Drell-Yan and J/ψ. A pair of separated jet triggers will be used to trigger on di-jets. The results of those algorithms will be sent to the STAR trigger system within 1.35 micro seconds after the collision for every bunch crossing.

We have performed GEANT simulations to optimize the FCS trigger response for single electrons, photons, and charged hadrons. We assume the on-line gains will be optimized for hadrons. Off-line, we will correct for the ~10% difference in sampling fraction when observing electrons or photons. However, we don't intend to make such a correction in the on-line trigger, so we have not done so here. We began by simulating 10, 20, 40, and 80 GeV e^-, γ, π^0, π^-, K^-, p, and $\bar{p}$. Electrons and photons behave very similarly. Likewise, all of the charged hadrons have similar response. So we focused on γ and π^- for the optimization. After a detailed comparison of the locations of the 4x4 ECal and HCal trigger patches where a given particle deposits the m ost energy (or transverse energy), we adopted the matching algorithm described in Figure 4-17.

The ratio of the energies in the matched ECal and HCal trigger patches provides trigger-level gamma/hadron discrimination, with HCal < ¼ ECal primarily selecting electromagnetic events and HCal > ¼ ECal primarily selecting hadronic events. Meanwhile, the sum of the energies in the matched ECal and HCal patches – the "trigger energy" – provides an excellent measure of the total energy observed in the entire ECal+HCal for photon events, and a very good measure for hadron events.

Figure 4-18 shows typical correlations. Photons can also satisfy the hadron trigger condition and vice versa. However, in most cases these "false positives" arise when ECal and HCal patches near the edge of the shower are matched, so the corresponding trigger energies are usually much smaller than the original particle energy (and much smaller than the highest energy pair of ECal-HCal trigger patches). Therefore, appropriately tuned thresholds will reject most of the false positives.

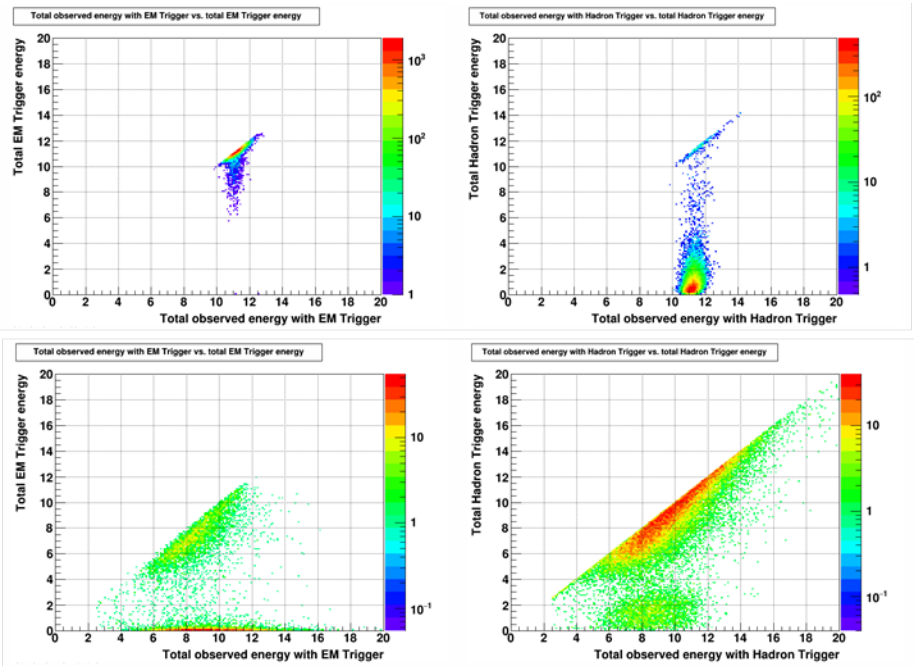

Figure 4-18: Correlation between the trigger energy and the total observed energy for 10 GeV γ (upper panels) and π^- (lower panels). The left panels show the results for matched ECal-HCal trigger patches that obey the electromagnetic event requirement, HCal < ¼ ECal. The right panels show the results for matched ECal-HCal trigger patches that obey the hadronic event requirement, HCal > ¼ ECal.

Figure 4-19 shows the predicted single-particle trigger efficiencies, as well as the false positive rates. For photons, when the trigger threshold is placed at 80% of the true photon energy, the trigger is predicted to be 99% efficient at low energy, dropping to 96% efficient for 80 GeV photons. For pions, when the trigger threshold is placed at 60% of the true hadron energy, the efficiency is only 74% at 10 GeV. Most of this loss arises from events where the total energy observed in the FCS falls below the trigger threshold. Only a small fraction comes from events that fail the HCal/ECal ratio condition. The efficiency increases for higher energy pions that typically produce better developed hadronic showers.

	Fraction of Events Passing EM Trigger with				Fraction of Events Passing Hadronic Trigger with			
Particle/Energy	EM_thr > 8	EM_thr > 16	EM_thr > 32	EM_thr > 64	Had_thr > 6	Had_thr > 12	Had_thr > 24	Had_thr > 48
Photon/10 GeV	**0.99**	0.00	0.00	0.00	0.01	0.00	0.00	0.00
Photon/20 GeV	0.99	**0.99**	0.00	0.00	0.05	0.02	0.00	0.00
Photon/40 GeV	0.98	0.98	**0.98**	0.00	0.31	0.09	0.04	0.00
Photon/80 GeV	0.96	0.96	0.96	**0.96**	0.88	0.44	0.13	0.06
Pion/10 GeV	0.05	0.00	0.00	0.00	**0.74**	0.09	0.00	0.00
Pion/20 GeV	0.09	0.05	0.00	0.00	0.91	**0.83**	0.10	0.00
Pion/40 GeV	0.04	0.03	0.02	0.00	0.98	0.95	**0.90**	0.10
Pion/80 GeV	0.01	0.01	0.01	0.01	0.99	0.98	0.97	**0.91**

Figure 4-19: Calculated efficiencies of the single-particle triggers for photons and π^-. The boxed entries show the efficiency for photons when the trigger energy threshold is set at 80% of the true photon energy and the efficiency for pions when the trigger energy threshold is set at 60% of the true pion energy. The likelihood of false positive triggers is also shown for various trigger energy thresholds and true particle energies.

For energies as low at 10 GeV, the instantaneous photon and hadron rates will be much higher than the data acquisition system will be able to record. So for low energy particles, we might choose to adopt more stringent particle definitions, *e.g.*, HCal < 1/8 ECal for photons and/or HCal > ½ ECal for hadrons, in order to record higher quality events while still filling the available DAQ bandwidth. We will optimize the energy dependence of the HCal/ECal trigger patch ratio criteria when we have a high-statistics sample of simulated PYTHIA+GEANT events.

The next step for the trigger definition will be to optimize the size and number of the overlapping jet patches.

5 The Forward Tracking System

5.1 Overview

The physics case for the STAR forward FCS and Forward Tracking System (FTS) upgrade is described in section 2 of this document. For transverse spin asymmetry measurements of charged pions in the forward direction in p+p and p+A collisions, it is necessary to distinguish positively charged pions from negatively charged ones with momentum up to 80 GeV/c. For Drell-Yan and J/ψ (direct photon and photon+jets) measurements in the forward direction, excellent electron (photon) identification capability is demanded in order to suppress the large hadron backgrounds by 3-4 orders of magnitude. Adding a forward tracking system becomes essential to achieve such goals. The FTS can separate particles with different charge signs, based on the different bending directions in the 0.5 T STAR solenoid magnet field. The FTS can improve electron identification by measuring charged particle momenta and comparing these to the associated energy depositions in the FCS. The FTS can also aid photon identification by vetoing on hits from charged particles. In order to achieve these goals, the FTS needs to have good position resolution and a low material budget. The FTS will provide essential information to study the longitudinal structure of the initial state that leads to breaking of boost invariance in heavy-ion collisions, and to explore the transport properties of the hot and dense matter formed in heavy-ion collisions near the region of perfect fluidity.

5.2 The FTS Silicon-Detector

Silicon detectors have been widely used in high-energy physics experiments. STAR recently built a silicon micro-vertex detector, the Heavy Flavor Tracker (HFT), to study heavy flavor production at mid-rapidity ($|\eta| < 1$) in high-energy nuclear collisions. The HFT includes 3 sub-systems: the Silicon Pixel detector (PXL), made of Monolithic Active Pixel Sensors (MAPS); the Intermediate Silicon Tracker (IST), made of single-sided double-metal Silicon Ministrip sensors; and the Silicon Strip Detector (SSD), made of double-sided Silicon Strip sensors.

In order to achieve good charge separation and momentum resolution, the silicon sensors for the FTS need to have precise position resolution in the azimuthal direction (*c.f.* section 3.3). The requirement on resolution in the radial direction is not very demanding. As it is mandatory to keep the ghost hit rate and occupancy under control, especially for A+A collisions, it is proposed to use single-sided double-metal Silicon Ministrip sensors with fine granularity in ϕ and coarse granularity in r. These sensors will be read out from their edges at large radii, so that the frontend readout chips, cabling, and cooling pipes and liquid can be placed as much as possible outside of the $2.5 \leq \eta \leq 4$ region to minimize the amount of materials in the FTS acceptance.

An FTS using Silicon Ministrip sensors can take advantage of the successful experience of the STAR IST detector. The latter has good S/N ratio (25:1), high hit efficiency (~99%), and small readout dead time (4%@1kHz, with potential improvement). The FTS would consist of three or more planes of Silicon sensors mounted transverse to the beam axis. In order to have the longest possible lever arm for momentum measurements, the FTS plane nearest (farthest) to the center of STAR will be placed at Z=139.9 (186.5) cm. These locations are constrained by the requirement to have η coverage between 2.5 and 4, and by the outer (inner) radius of the beam pipe (TPC inner field cage). As shown below, such a design can provide optimal charge-sign separation and momentum resolution in p+p and p+A collisions, with minimal materials ($\leq$1% X_0/layer) in the acceptance. We estimate that the average occupancy in the silicon-based FTS option is 3.2% (10%) at η = 4 (2.5) in the 0-3% most central Au+Au collisions at $\sqrt{s_{NN}}$ = 200 GeV. This estimate is based on the charged particle multiplicities measured with the PHOBOS experiment [135], taking into account that the number of primary tracks is roughly 50-60% of the total number of tracks.

5.2.1 Silicon Ministrip Sensors

STAR has started an R&D project with Hamamatsu to develop single-sided double-metal Silicon Ministrip sensors for the FTS. Shown in Figure 5-1 are sensor masks under development, in which a second metal layer is needed to bring the signals from the inner radii to the outer radius of the sensors. Shown in Figure 5-2 are finite element simulation results for the sensor electrical properties and its response to charged particles passing through. Prototype sensors will be available in June 2019, followed by a full evaluation of their characteristics and responses to charged particles.

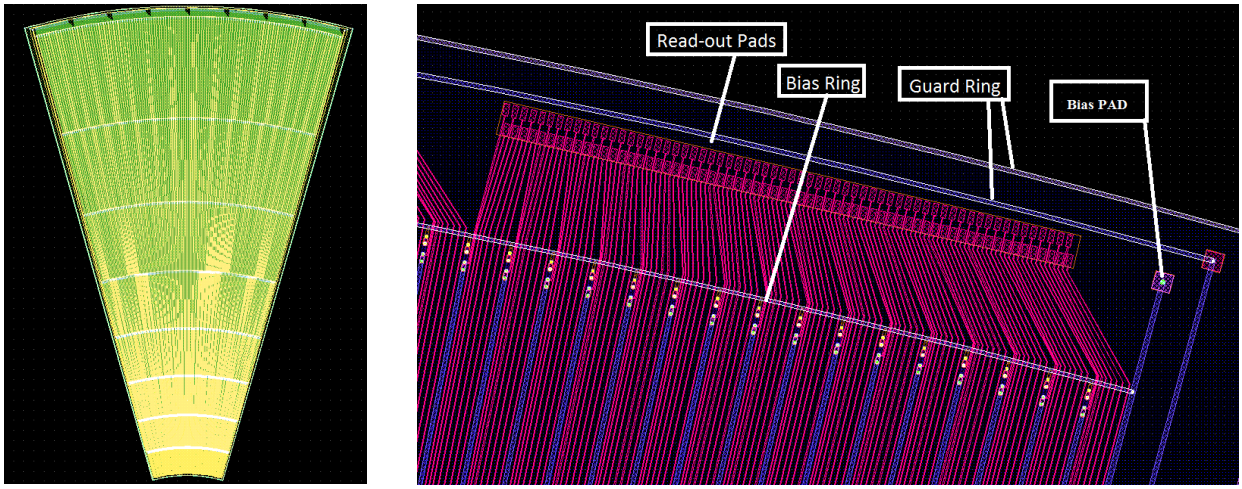

Figure 5-1: (Left) Full view of a FTS Silicon sensor mask. (Right) Zoomed-in view of the sensor mask.

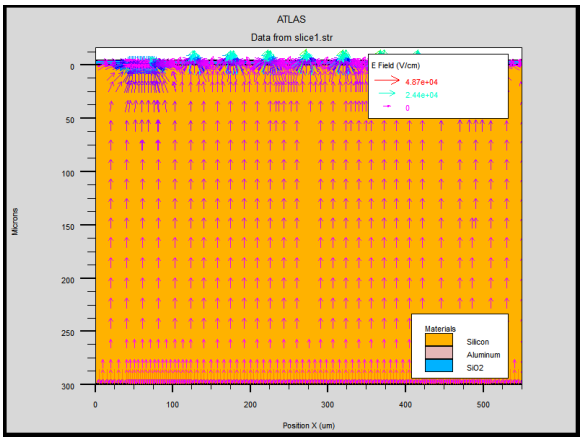

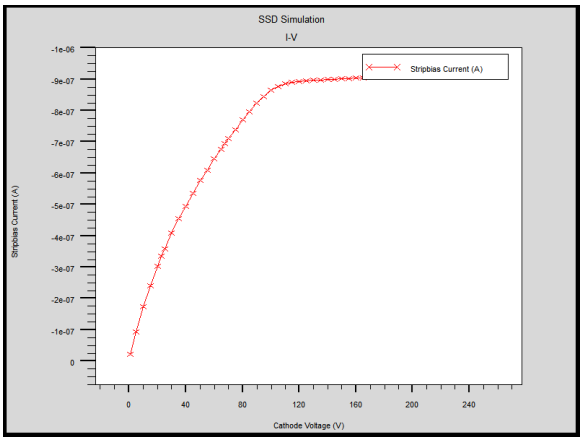

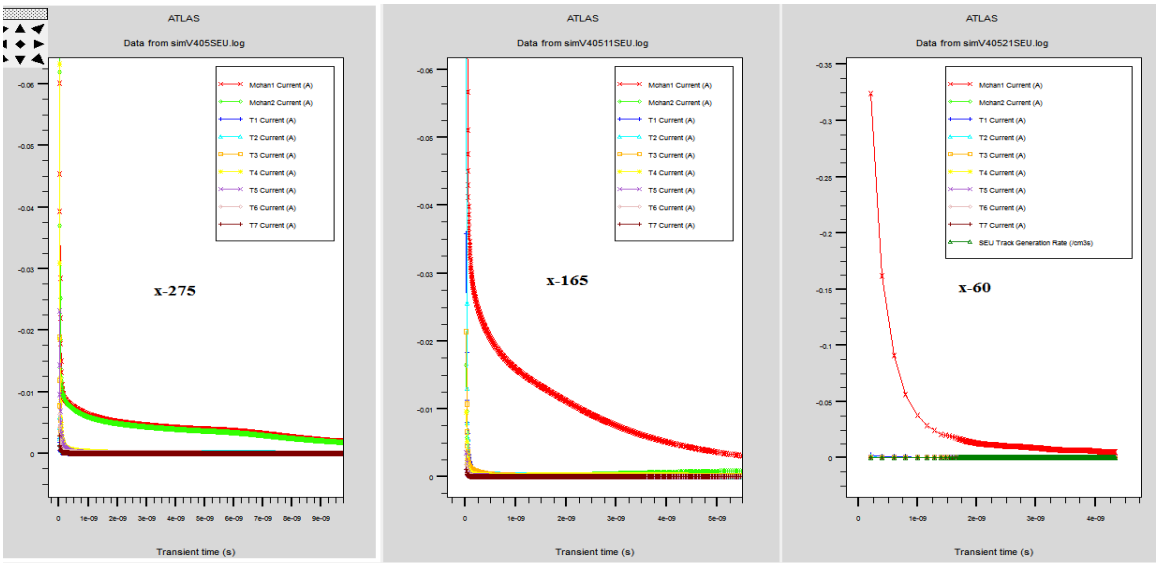

Figure 5-2: Finite-element simulation results of a FTS Silicon Ministrip sensor. Top-left: electrical field lines in the sensor cross-section view. Top-right: sensor leakage current vs bias voltage. Bottom: transient electrical signals from the top layer Al strips when a charged particle hit is in the middle (left), at one quarter of the distance between (middle), or on top of (right) one of the two azimuthally neighboring Silicon P+ implant strips. The red and green curves correspond to the top layer Al strips on top of the Silicon P+ implant strips, while the others are the top layer Al strips to bring signals from smaller radius P+ implant strips to the sensor outer radius edge.

5.2.2 Silicon Detector: Frontend Readout Chips

Several different frontend chips are available to read out the Silicon Ministrip sensors. The APV25-S1 chip has been used in the IST. It has 128 channels each, with a charge sensitive pre-amplifier, shaper, and 4 μs long pipeline (see Figure 5-3). Events are read into the pipeline at 40MHz. Events in the pipeline are selected by triggers and marked for readout. A single differential pair per chip reads out each of the 128 channels in series for a selected event. The APV25-S1 chip can also be used to read out FTS sensors, in which case the same DAQ system as that of the IST can be used to minimize electronics engineering work. In total 288 APV chips will be needed to read out 3 Forward Silicon Tracker (FST) disks, for which a sufficient number of APV chips have been obtained.

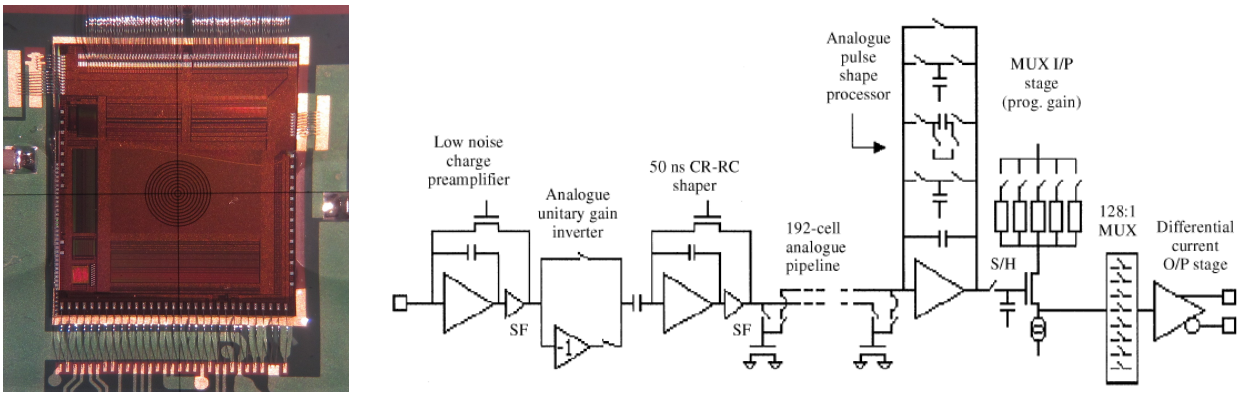

Figure 5-3: Left: Picture of an APV25-S1 chip. Right: block diagram of one channel of the APV25

5.2.3 Silicon Detector Wedges

The preliminary design of the FST wedge includes a supporting structure, three silicon ministrip sensors and eight frontend readout chips mounted on hin, flexible, printed circuit hybrid. The supporting structure is composed of two thin plates for holding the silicon sensors and the readout chips. Moreover, an O-shaped cooling pipe will run underneath the readout chips. In order to avoid the gap between the inner and outer silicon sensors, Silicon sensors will be attached on the different side of the wedge.

The material for the FST supporting structure is the mixture of polyphenylene sulfide (PPS) and 10% carbon fiber. Figure 5-4 show the preliminary design of the single wedge viewed from different directions. The main supporting structure is shown in gray, and the fan-shaped blue areas and the green squares indicate the silicon sensors and readout chips, respectively, and the flexible hybrid is shown in orange. Figure 5-5 shows the integrated wheel-shaped disk for the FST.

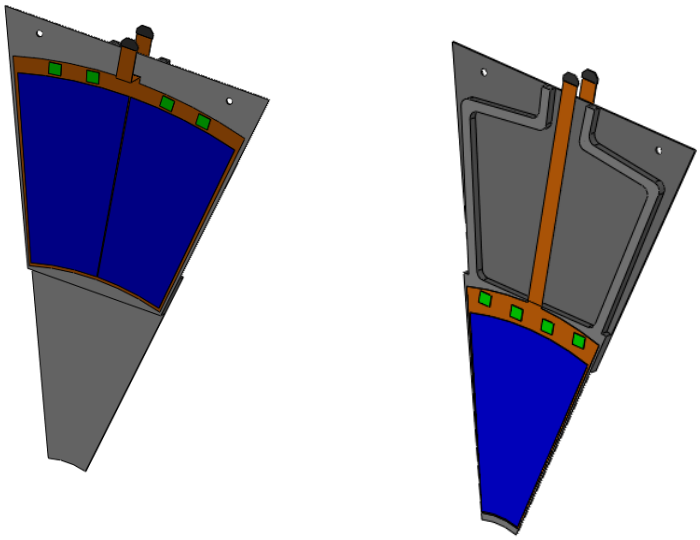

Figure 5-4:
The FTS wedge is composed of a supporting structure (gray), silicon ministrip sensors (blue), flexible hybrid (orange) and readout chips (green).

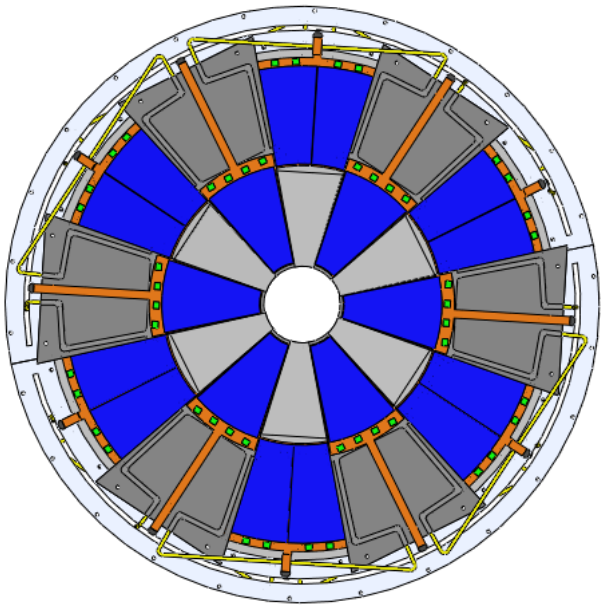

Figure 5-5: The integrated wheel-shaped disk for the FTS. The ring at the outer radius is the interface to the STAR main structure.

5.2.4 Silicon Detector: DAQ System

The DAQ system used to read out the IST with 864 APV chips will be re-used for the FTS with 288 APV chips. The DAQ system has a modular design, which is based on a passive compact PCI backplane running a custom protocol, connecting 6 readout modules to a readout controller module. The readout modules provide all necessary functions, including isolated power supplies, to operate up to 24 APV25 chips per module with high-impedance ground isolation. The frontend boards contain a minimal set of components as they are located inside the STAR TPC inner field cage and are inaccessible except during long shutdown periods. The frontend boards connect to the readout modules with cables up to 24 m in length, carrying unbuffered analog readout signals from the APV25 as well as power, trigger, clock and control signals. The readout module digitizes the APV analog samples to 12-bits at 37.532 MHz, and buffers the data. The readout controller distributes trigger and clock from the central trigger system, gathers the data over the backplane, and ships it to a linux PC via a 2.125 Gbps optical data link (Detector Data Link (DDL) from ALICE). The PC gathers data from multiple readout controllers and dispatches it to the STAR event builders. The readout modules, controllers, and backplanes are housed in a common crate together with the Silicon sensor HV bias power supplies. The DAQ system described above is shown in Figure 5-6.

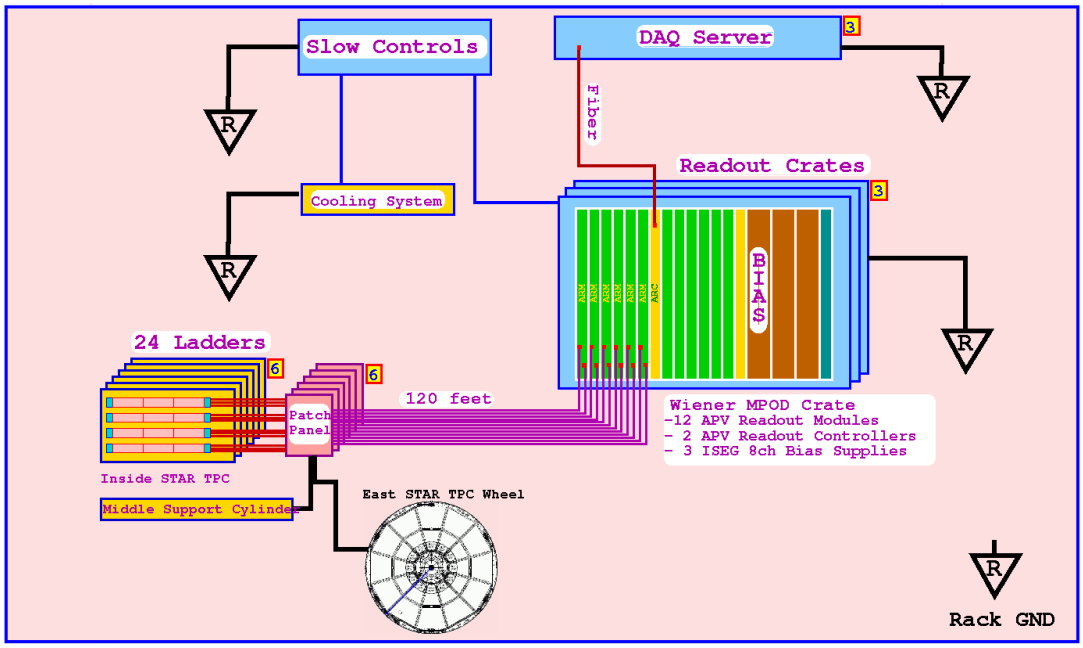

Figure 5-6: DAQ System for the FTS based on APV-chip readout.

5.2.5 Silicon Detector: Cooling System

The amount of heat generated by an APV chip is around 0.3 W. In order to keep the APV chips and Silicon sensors at low temperature, the APV chips need to be cooled. The IST cooling system (shown in

Figure 5-7) keept the IST at room temperature by using 3M NOVEC to transfer out the heat generated by 864 APV chips. It will be re-used for the FST (288 APV chips).

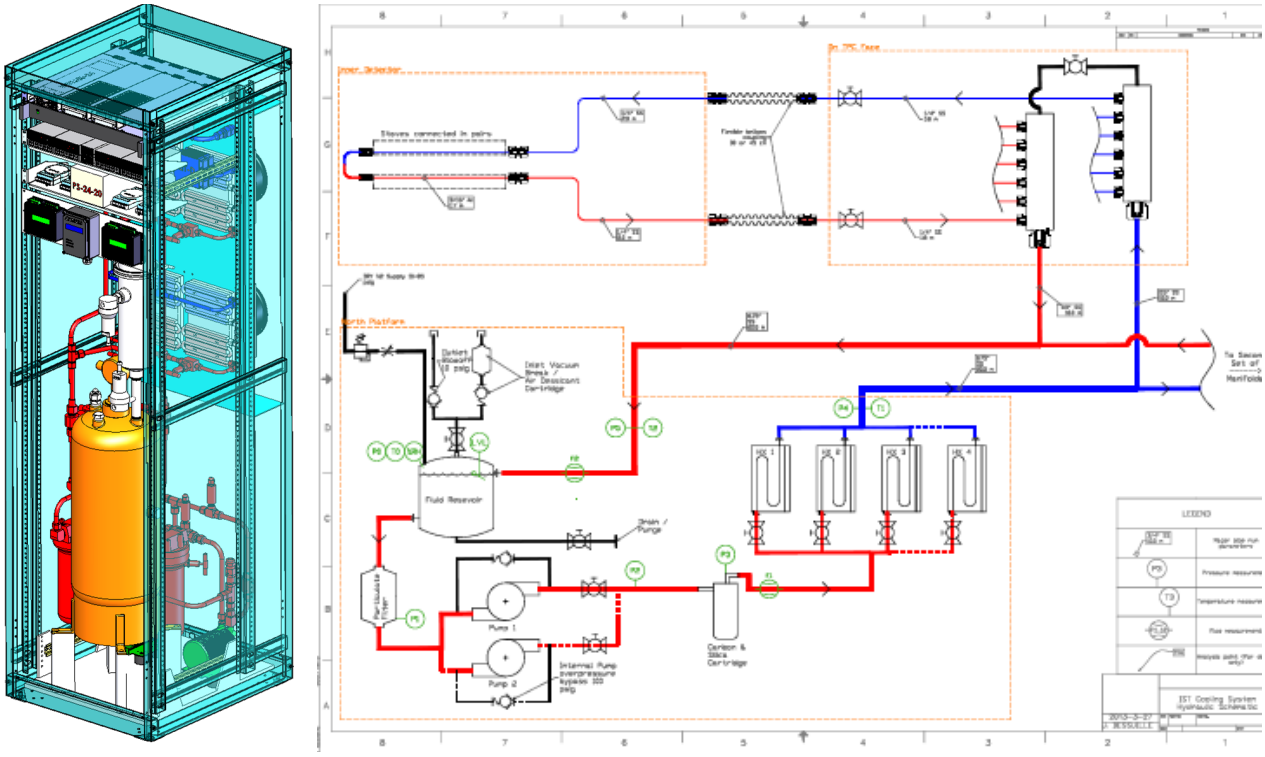

Figure 5-7: FTS cooling system. (Left) CAD drawing of the cooling system rack. (Right) Connections and flows.

5.2.6 Silicon Detector: Slow Control System

The slow controls system will serve as the primary means for controlling and monitoring the working parameters of the FTS. These parameters, such as temperatures, component currents and voltages will be interfaced with the standard STAR alarm system. The alarm system logs the parameter history and alerts the shift crews if operating limits are exceeded. The slow controls for the FTS and readout crates will be handled exclusively by Ethernet traffic to the FTS Linux box, through the ALICE DDL link to the readout crates, and then finally through the RDOs to the APV's via the local I^2C link. There will be no other hardware needed for slow controls. All power supplies will be fitted with an Ethernet controls interface.

5.2.7 Silicon Detector: Radiation Exposure

The primary concerns in radiation damage to Silicon Ministrip detectors include possible damage to frontend readout chips by ionizing energy losses of charged particles, and to Silicon sensors by non-ionizing energy losses (NIEL) of hadrons. The former won't be a concern for APV chips which were designed for the much higher radiation environment at the LHC. It is manufactured using an IBM 0.25μm radiation hard process and can tolerate 20+ Mrad radiation dose. The expected ionizing radiation exposure at STAR is orders of magnitude smaller, as shown in Table 5-1.

The NIEL can be estimated from MC simulations and previous Silicon detector running experience. After 14 weeks of Au+Au collisions at $\sqrt{s}$=200 GeV in 2014, the bias current in the IST increased by 1-2 μA per sensor. These Silicon sensors have a volume of 0.03*4*7.7 cm^3. This suggests that the NIEL for the IST in Run14 was less than $5*10^{10}$ cm^{-2} 1-MeV neutron equivalent flux. By scaling this number to the particle flux maps that are obtained from MC simulations and verified by measurements [136], the total NIEL for the FST during the entire proposed p+p and

Au+Au runnings ranges between 1 - 7*10^{12} cm^{-2} across the detector surface, with an average value of around 1.2*10^{12} and 2*$10^{12}$$cm^{-2}$ for the sensors in the outer and inner regions, respectively. The 1-MeV neutron equivalent flux won't have a significant impact on the sensor performance. Therefore, it can be concluded that radiation damage is not of a concern for the FST during its data taking. Caution will be taken during beam injections and machine studies by turning off the powers to the APV chips and Silicon sensors.

Radius [cm]	200 GeV Au+Au [krad]	500 GeV p+p [krad]
2.5	5.3-28	29-133
14	0.2-1	1-4
22	0.1-0.4	0.4-2

Table 5-1: Radiation field in krad from physics collisions in the center of STAR extrapolated to RHIC II luminosities for different radial positions for 12 weeks of run time.

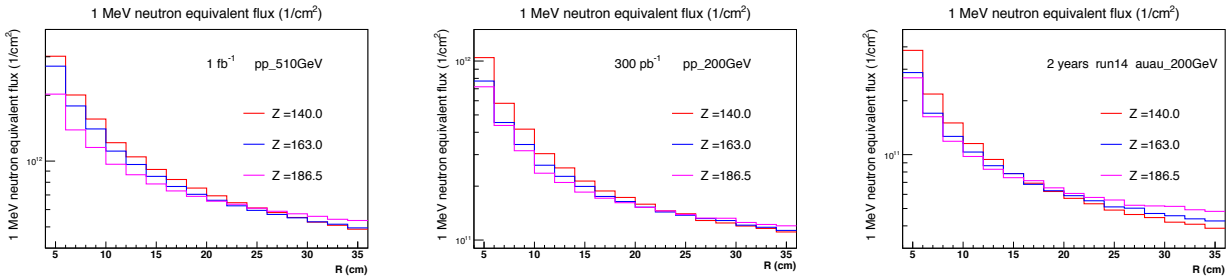

Figure 5-8: Non-ionizing radiation as a function of distance from the beam for 1.1 fb-1 500 GeV p+p (left), 300 pb-1 200 GeV p+p (middle) and two-year 200 GeV Au+Au (right) collisions for the Forward Silicon Tracker stations at Z=140-186.5 cm.

5.2.8 Silicon Detector: Additional R&D

To validate and optimize the FTS design based on the Silicon Microstrip detector technology, R&D is carried to develop appropriate Silicon Ministrip sensors and mechanical supporting structure to meet the requirements. STAR has started an R&D program. Prototype Silicon sensors will be delivered by Hamamatsu in summer 2019. They will be assembled together with APV chips onto prototype mechanical structures fabricated by Aerospace Industrial Development Corporation and tested in Fall/Winter 2019.

5.2.9 Silicon Detector: Survey and Alignment

The FTS planes will have to be aligned, both with respect to each other and with respect to the STAR reference frame. This will be achieved by survey measurements and ultimately by using tracks in p+p, p+A, and A+A collisions. In a silicon-based FTS, the internal structure of the silicon sensors will be known with an accuracy of better than 10 μm, far beyond the physics requirements. This information is obtained through the production mask drawings of the silicon sensors, and accessed through alignment marks on these sensors. The FTS planes and mechanic mounting structures will again be surveyed after their assembly and before the installation into STAR. Once the FTS is installed in STAR, tracks produced in p+p, p+A, and A+A collisions will travel through the FTS planes. The relative positions and rotations among the FTS planes, and between the FTS planes and other mid-rapidity detectors, will be determined using an iterative residual method for the reconstructed tracks.

5.3 The sTGCs for the FTS system

Using Small-strip Thin Gap Chambers (sTGC), as designed by the ATLAS experiment [137,138], are a practical alternative for the FTS forward tracking, when combined with inner silicon-strip sensors. One key advantage is a significant reduction of the project cost, while maintaining the excellent momentum resolution required.

5.3.1 sTGC Detector technology

The basic structure of a sTGC is shown in Figure 5-9; more details can be found in Ref. [139]. It consists of a grid of 50 μm diameter gold-plated tungsten wires, with a 1.8 mm pitch, sandwiched between two cathode planes located at a distance of 1.4 mm from the wire plane. The operating voltage is 2900 V for the wires. The cathode planes are made of a graphite-epoxy mixture with a typical surface resistivity of 100 kΩ sprayed on a 100 μm thick G-10 plane. Behind the cathode planes, on one side of the anode plane there are copper strips for precise coordinate measurements that run perpendicular to the wires, and on the other side of the anode plane are copper pads used for fast triggering. The copper strips and pads act as readout electrodes. The pads cover large rectangular surfaces on a 1.5 mm thick printed circuit board (PCB), with the shielding ground on the opposite side. The latter will probably not be used at STAR.

The strips have a 3.2 mm pitch, much smaller than that of the ATLAS TGC; hence, they are named 'small-strip TGC'. This strip pitch was optimized for good position resolution (< 100 μm) using charge division between strips while maintaining a minimal number of read-out channels [140]. In practice, single strip-layer position resolutions of better than 50 μm have been obtained, uniform along the sTGC strip and perpendicular wire directions, in recent prototype tests [141]. The operational gas is a mixture of 55% CO_2 and 45% n-pentane. For the FTS setup, two layers of sTGC modules, with their strips perpendicular to each other, will be combined into one sTGC disk, which will provide *x-y* (2-d) position reconstruction from strip charge read out. Four 60cm x 60cm double-sided sTGC will form one plane.

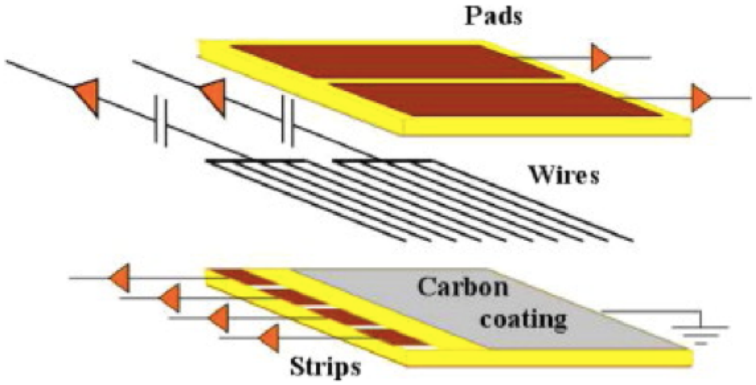

Figure 5-9: The sTGC internal structure.

5.3.2 Readout electronics of the sTGC

The detector is basically an MWPC with pad readout – similar to the STAR TPC – so this offers the possibility for large savings in cost and effort by re-using the STAR TPC electronics for its readout.

We plan to reuse the current STAR TPC electronics as-is (based on the ALTRO ASIC). A sufficient amount of this electronics will become available after 2019 when STAR will replace it with new electronics for the STAR Inner TPC (iTPC) Project. The obvious advantage is little or no cost in the design & production of the readout system. The whole section of the TPC readout chain can thus

be repurposed, including the frontend (FEE) cards, the multiplexer cards (RDO), power-supplies, optical fibers, the readout cards, readout PCs, all the DAQ readout and control software, leading to a dramatic decrease in cost, effort, risk & integration.

Recently, the TPC electronics was used for the test of ALTAS sTGC module readout at Shandong University. Four strips on the sTGC were connected to the FEEs and were read out by the TPC electronics. At 2900 volts, the ALTAS sTGC working HV, clear signal distributions were observed. However, the peak structure indicates that with this HV the signal reaches the limit of TPC measuring range. To lower the gain, a HV scan was performed from 2900 volts down to 2600 volts. Clear decreasing signals were observed consistent with our expectation. By selecting suitable working HV, the detector can give a signal within the TPC electronics limit. For these tests, the noises were at a high level compared to the TPC regular value. This was likely caused by the grounding issue and/or cable connection from the strips to the FEE.

In addition, a prototype of 30cm×30cm sTGC was constructed with TPC electronics readout. In this prototype, the spare strips were grounded and the FEE were directly connected to the readout strips of the PCB. Figure 5-10 below shows ADC versus time bin for all readout channels in a cosmic ray event. A strong and large signal is seen. After a thorough test at Shandong University, this prototype will be shipped to BNL and installed at the STAR experiment for the Run 2019.

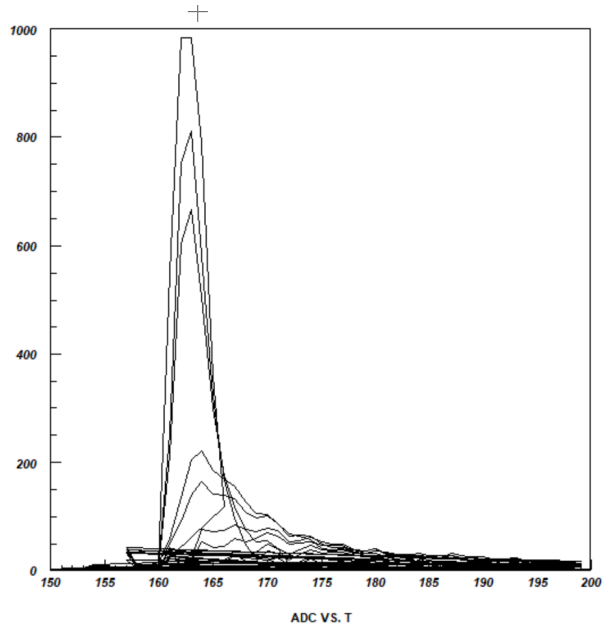

Figure 5-10: ADC as a function of time bin in a cosmic ray event for a prototype of 30cm×30cm sTGC with TPC electronics readout.

5.3.3 Construction & cost estimation sTGC

The high-energy physics group at Shandong University is responsible for building 40 modules (each consisting of four layers) of new small-wheel sTGC's. Because of the minimal re-design of the sTGC for the STAR forward tracking option – for example, using a square shape of 60 cm x 60 cm, with 3.2 mm strip pitch perpendicular to wire direction – it will be straightforward for the Shandong University group to produce 4 sTGC disks (each consisting of two layers and four modules per layer) for STAR. The construction cost is estimated to be about $200K, based on ATLAS experience, which will be financed by the STAR Chinese groups.

The main cost will come from the mechanical integration and cooling. The cost for electronics will be greatly reduced since we reuse the TPC electronics. For each 60 cm x 60 cm sTGC module, assuming 3.2 mm strip pitch, with each strip segmented into 4 pieces (15 cm long), and four two-layer disks, 24000 channels will be required. Segmented strips are important for multiple readout of each line perpendicular to the wire, for high-multiplicity events such as heavy ion collisions.

5.4 Installation Procedures for the FTS

Following cosmic-ray, source, and beam tests, the FTS will be transported from UIC, the facilities where the wedges are assembled to Brookhaven National Laboratory for final assembly and integration. It is planned to design and use a suitable extension of the existing West-Support-Cone internal rail structure on the West side of the STAR experiment, similar to the insertion mechanism of the FGT shown Figure 5-11. Besides installation, this support will allow systematic in-situ tests of the FTS with STAR services as well as maintenance repair between RHIC runs without having to move the main detector to the assembly hall.

The Si Disks will be installed inside the existing Carbon Fiber Structure (STAR IDS or Cone). This detector will consist of 3 Si disks. Detector, services and installation structure will weigh between 15 kg. Existing features (threaded holes) on the TPC wheel and the end ring of the IDS can be used to mount one end of the structure and the second end will be supported by using pushers/adjusters to align the detector to the beam pipe.

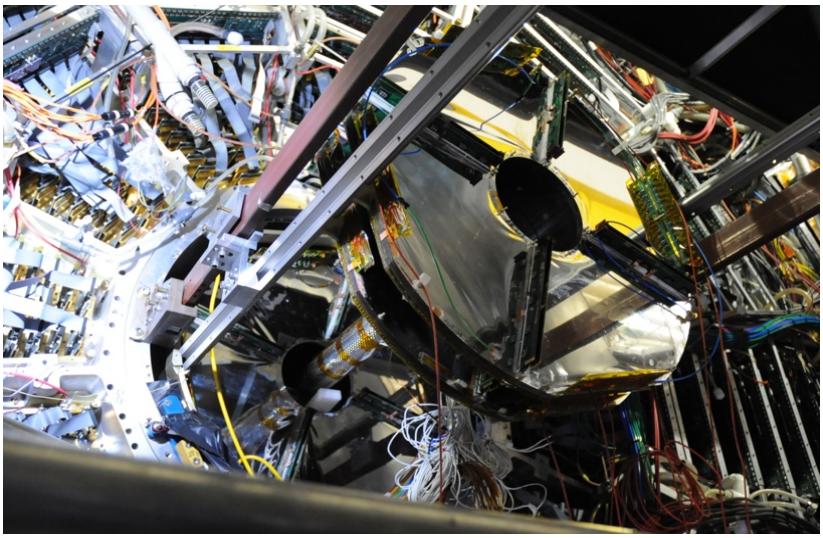

Figure 5-11: Rail setup for the STAR in-situ installation of the FGT subsystem. A similar concept is proposed for the FTS.

The sTGC detector will be sitting in the center of the west pole-tip opening and will weigh approximately 800 pounds. It will consist of 4 planes with each plane weighing about 200 pounds. The existing EPD mount brackets and existing threaded holes in the poletip/EEMC detector ID face will be used to mount the installation structure to support the weight of the detector planes. This installation structure will also be used to mount the electronics and cooling manifolds needed for the detector.

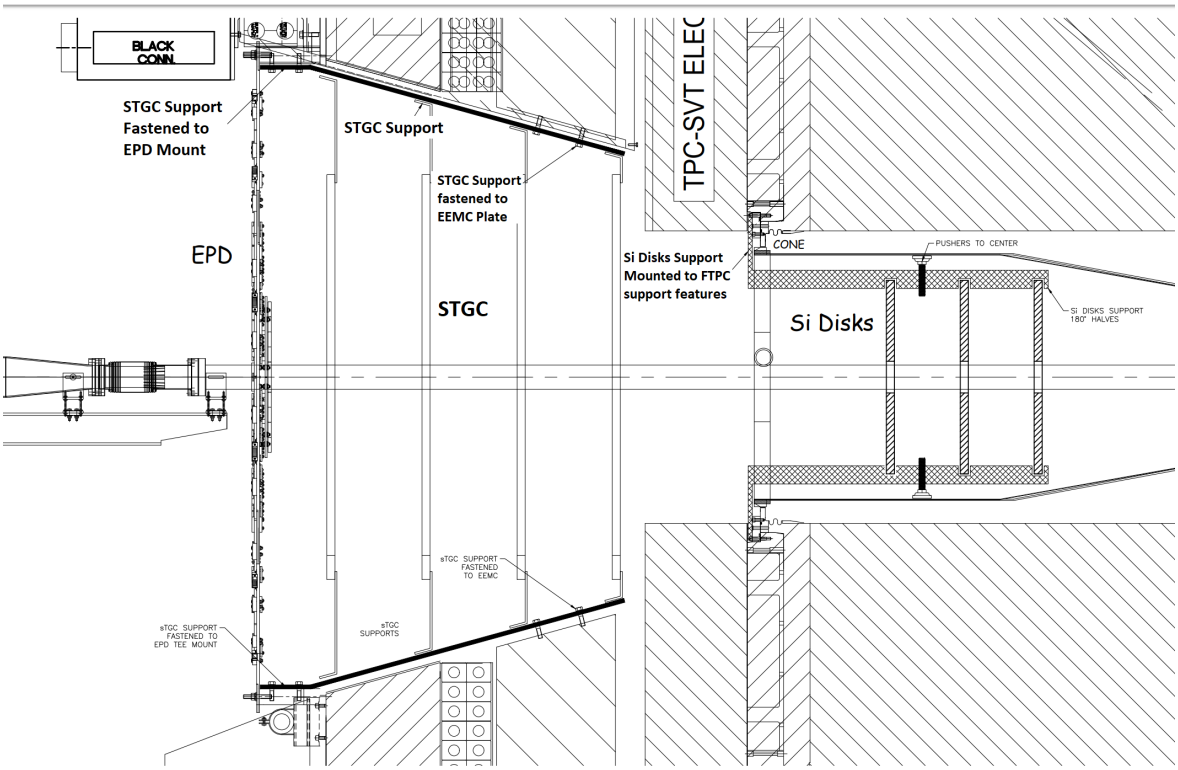

Figure 5-12: Design and Layout of the Silicon and sTGCs on the west side of STAR.

6 Bibliography

[1] The 2015 Long Range Plan for Nuclear Science "Reaching for the Horizon" http://science.energy.gov/~/media/np/nsac/pdf/2015LRP/2015_LRPNS_091815.pdf.
[2] The RHIC Cold QCD Plan for 2017 to 2023 – A Portal to EIC E.C. Aschenauer et al., arXiv:1602.03922
[3] The STAR midrapidity pp, pA, AA physics program beyond BES-II https://drupal.star.bnl.gov/STAR/starnotes/public/sn0669
[4] A. Abusleme et al., Nucl.Instr. & Meth. A817 (2016) 85.
[5] V. Smakhtin et al., Nucl.Instr. & Meth. A598 (2009) 196.
[6] RBRC Workshop on "Emerging Spin and Transverse Momentum Effects in pp and p+A Collisions", BNL February 2016, https://www.bnl.gov/estm2016/
[7] The RHIC Spin Program: Achievements and Future Opportunities E.C. Aschenauer et al., arXiv:1501.01220
[8] A. V. Efremov and O. V. Teryaev, Sov. J. Nucl. Phys. 36 (1982) 140 [Yad. Fiz. 36, 242 (1982)]; Phys. Lett. B 150 (1985) 383
J.-W. Qiu and G. F. Sterman, Phys. Rev. Lett. 67 (1991) 2264; Nucl. Phys. B 378 (1992) 52; Phys. Rev. D 59 (1999) 014004.
[9] K. Kanazawa, Y. Koike, A. Metz and D. Pitonyak, Phys. Rev. D 89 (2014) 111501(R).
[10] BRAHMS Collaboration, Phys. Rev. Lett. 101 (2008) 042001.
[11] A_NDY Collaboration, Phys. Lett. B750 (2015) 660.
[12] L. Gamberg, Z.-B. Kang, and A. Prokudin, Phys. Rev. Lett. 110 (2013) 232301.
[13] J.C. Collins and T. Rogers, Phys.Rev. D91 (2015) 074020.
[14] J. Ralston and D.Soper, Nucl. Phys. B152 (1979) 109.
[15] R. Jaffe and X. Ji, Nucl. Phys. B375 (1992) 527.
[16] P. Mulders and R. Tangerman, Nucl. Phys. B461 (1996) 197.
[17] D. Sivers, Nuovo Cim. C035N2 (2012) 171
[18] R. L. Jaffe and X. Ji, Phys. Rev. Lett. 67 (1991) 552.
[19] A. Courtoy, St. Baeßler, M. Gonzalez-Alonso and S. Liuti, Phys.Rev.Lett. 115 (2015) 162001.
[20] J. C. Collins, Nucl. Phys. B396 (1993) 161.
[21] J. C. Collins, S. F. Heppelmann, and G. A. Ladinsky, Nucl. Phys. B420 (1994) 565.
[22] A. Airapetian *et al.* (HERMES Collaboration), Phys. Rev. Lett.94 (2005) 012002; 103 (2009) 152002; Phys. Lett. B693 (2010) 11.
[23] V. Y. Alexakhin *et al*. (COMPASS Collaboration), Phys. Rev. Lett. 94 (2005) 202002;
E. S. Ageev *et al*. (COMPASS Collaboration), Nucl. Phys. B765 (2007) 31;
M. G. Alekseev *et al.* (COMPASS Collaboration), Phys. Lett. B673 (2009) 127; B692 (2010) 240;
C. Adolph *et al.* (COMPASS Collaboration), Phys. Lett. B717, 376 (2012);
N. Makke (COMPASS Collaboration), PoS EPS-HEP2013 (2013) 443.
[24] A. Airapetian *et al.* (HERMES Collaboration), JHEP 0806 (2008) 017.
[25] C. Adolph *et al.* (COMPASS Collaboration), Phys. Lett. B 713 (2012) 10.
[26] R. Seidl *et al.* (Belle Collaboration), Phys. Rev. Lett 96 (2006) 232002; Phys. Rev. D 86 (2012) 039905(E).
[27] A. Vossen *et al.* (Belle Collaboration), Phys. Rev. Lett. 107 (2011) 072004.
[28] M. Anselmino *et al.,* Phys. Rev. D 75 (2007) 054032; Nucl. Phys. B, Proc. Suppl. 191 (2009) 98; Phys. Rev. D 87 (2013) 094019.
[29] A. Bacchetta, A. Courtoy, and M. Radici, Phys. Rev. Lett. 107 (2011) 012001.
[30] F.Yuan, Phys. Rev. Lett. 100 (2008) 032003; Phys.Rev.D77 (2008) 074019.
[31] U. D'Alesio, F. Murgia, and C. Pisano, Phys. Rev. D 83 (2011) 034021.
[32] A. Bacchetta and M. Radici, Phys. Rev. D70 (2004) 094032.
[33] L. Adamczyk et al. (STAR Collaboration), Phys. Rev. D 97, 032004 (2018).
[34] L. Adamczyk et al. (STAR Collaboration), Phys. Lett. B780, 332 (2018).
[35] STAR Collaboration, Phys.Rev.Lett. 115 (2015) 242501
[36] [M. Radici and A. Bacchetta, Phys. Rev. Lett. 120, 192001 (2018)
[37] Z.-B. Kang, Phys. Rev. D83 (2011) 036006.
[38] St. Kofler and B. Pasquini, arXiv: 1701.07839,

Z. Ye *et al.,* Phys.Lett. B767 (2017) 91
B. Yoon *et al.*, Proceedings of Science LATTICE 2015 (2016) 116, arXiv:1601.05717
Z.-B. Kang, A. Prokudin, P. Sun, and F. Yuan, Phys.Rev. D91 (2015) 071501
[39] M. Anselmino *et al.,* Phys.Rev. D73 (2006) 014020.
[40] T.C. Rogers and P.J. Mulders, Phys.Rev. D81 (2010) 094006.
[41] J.L. Drachenberg (STAR Collaboration), Proceedings of the 20th International Conference on Particles and Nuclei (PANIC 14), (2014), pp. 181–184, http://inspirehep.net/record/1375601/files/78.pdf.
J.L. Drachenberg (STAR Collaboration), EPJ Web Conf. 73 (2014) 02009.
[42] J. Soffer, Phys.Rev.Lett. 74 (1995) 1292.
[43] Z. Kang, A. Prokudin, P. Sun, and F. Yuan, Phys.Rev. D93 (2016) 1, 014009.
[44] L. Adamczyk *et al.* (STAR Collaboration) Phys. Rev. D 95, 071103(R)
[45] S. Ramachandran (STAR Collaboration), PoS DIS2016 (2016) 231, arXiv:1608.01332
[46] J. Adam et al. (STAR Collaboration), Phys. Rev. D 98, 032011 (2018).
[47] STAR Collaboration, Phys.Rev.Lett. 115 (2015) 092002.
[48] Z. Chang, Proceeding Spin-2014, arXiv:1512.05400.
[49] B. Jäger, M. Stratmann and W. Vogelsang, Phys. Rev. D 70 (2004) 034010.
[50] A. Mukherjee and W. Vogelsang, Phys. Rev. D 86 (2012) 094009.
[51] D. de Florian, R. Sassot, M. Stratmann, and W. Vogelsang, Phys. Rev. Lett. 113 (2014) 012001.
[52] E. Leader, A.V. Sidorov, and D.B. Stamenov, Phys. Rev. D 82 (2010) 114018.
[53] The NNPDF Collaboration: E.R. Nocera, R.D. Ball, St. Forte,
G. Ridolfi and J. Rojo, Nucl.Phys. B887 (2014) 276.
[54] PHENIX Collaboration, Phys.Rev. D90 (2014) 072008.
[55] PHENIX Collaboration, Phys. Rev. D93, (2016) 011501.
[56] B. Jäger, A. Schäfer, M. Stratmann and W. Vogelsang, Phys. Rev. D 67 (2003) 054005.
[57] E.C. Aschenauer, R. Sassot, and M. Stratmann Phys. Rev. D 92 (2015) 094030.
[58] A. Accardi et al. , EIC White Paper: Electron Ion Collider: The Next QCD Frontier - Understanding the glue that binds us all, arXiv:1212.1701.
[59] E.C. Aschenauer et al. , The RHIC Spin Program: Achievements and Future Opportunities, arXiv:1501.01220
[60] A. Airapetian *et al.* (HERMES Collaboration), Phys. Lett, B577 (2003) 37; Nucl. Phys. B780 (2007) 1; Phys. Lett. B684 (2010) 114.
[61] W. Brooks and H. Hakobyan, Nucl. Phys. A830 (2009) 361.
[62] M. Vasilev *et al.* (E866 Collaboration), Phys. Rev. Lett. 83 (1999) 2304.
[63] H. Paukkunen, DIS-2014,
http://indico.cern.ch/event/258017/session/1/contribution/222/material/slides/0.pdf
[64] D. de Florian, R. Sassot, M. Stratmann, and P. Zurita, Phys.Rev. D85 (2012) 074028.
[65] PHENIX Collaboration, Phys.Rev.Lett. 98 (2007) 172302.
[66] K. J. Eskola, H. Paukkunen, and C. A. Salgado, JHEP 0904, 065 (2009).
[67] R. Sassot, M. Stratmann, and P. Zurita, Phys. Rev. D81 (2010) 054001.
[68] H. Paukkunen, DIS-2014,
http://indico.cern.ch/event/258017/session/1/contribution/222/material/slides/0.pdf
[69] K.J. Eskola, P. Paakkinen, H. Paukkunen, C.A. Salgado, Eur.Phys.J. C77 (2017) no.3, 163,
N. Armesto, *et al.*, Eur.Phys.J. C76 (2016) no.4, 218.
[70] PHENIX Collaboration, Phys.Rev.Lett. 98 (2007) 172302.
[71] K. J. Eskola, H. Paukkunen, and C. A. Salgado, JHEP 0904, 065 (2009).
[72] H. Paukkunen and P. Zurita, JHEP 1412 (2014) 100.
[73] E.C. Aschenauer *et al.*, eRHIC Design Study: An Electron-Ion Collider at BNL, arXiv:1409.1633.
[74] H. Paukkunen, K. J. Eskola, and C. A. Salgado, Nucl. Phys. A931 (2014) 331;
K. J. Eskola, H. Paukkunen, and C. A. Salgado, JHEP 1310, 213 (2013).
[75] L. V. Gribov, E. M. Levin, and M. G. Ryskin, Phys. Rept. 100 (1983) 1;
E. Iancu and R. Venugopalan, hep-ph/0303204;
H. Weigert, Prog. Part. Nucl. Phys. 55 (2005) 461;
J. Jalilian-Marian and Y. V. Kovchegov, Prog. Part. Nucl. Phys. 56 (2006) 104;
F. Gelis, E. Iancu, J. Jalilian-Marian, and R. Venugopalan, Ann. Rev. Nucl. Part. Sci. 60 (2010) 463;
J. L. Albacete and C. Marquet, Prog. Part. Nucl. Phys. 76 (2014) 1;
Y. V. Kovchegov and E. Levin, Quantum Chromodynamics at High Energy,

Cambridge University Press, 2012.
[76] A. H. Mueller and J.-W. Qiu, Nucl. Phys. B268 (1986) 427;
L. D. McLerran and R. Venugopalan, Phys. Rev. D49 (1994) 2233; D49 (1994) 3352; D50 (1994) 2225;
Y. V. Kovchegov, Phys. Rev. D54 (1996) 5463; D55 (1997) 5445;
J. Jalilian-Marian, A. Kovner, L. D. McLerran, and H. Weigert, Phys. Rev. D55 (1997) 5414.
[77] A. H. Mueller, Nucl. Phys. B415 (1994) 373;
A. H. Mueller and B. Patel, Nucl. Phys. B425 (1994) 471;
A. H. Mueller, Nucl. Phys. B437 (1995) 107;
I. Balitsky, Nucl. Phys. B463 (1996) 99; Phys. Rev. D60 (1999) 014020;
Y. V. Kovchegov, Phys. Rev. D60 (1999) 034008; D61 (2000) 074018;
J. Jalilian-Marian, A. Kovner, and H. Weigert, Phys. Rev. D59 (1998) 014015;
J. Jalilian-Marian, A. Kovner, A. Leonidov, and H. Weigert, Phys. Rev. D59 (1998) 014014;
E. Iancu, A. Leonidov, and L. D. McLerran, Phys. Lett. B510 (2001) 133;
Nucl. Phys. A692 (2001) 583.
[78] A. Accardi et al. , EIC White Paper: Electron Ion Collider:
The Next QCD Frontier - Understanding the glue that binds us all, arXiv:1212.1701
[79] Y. V. Kovchegov and M. D. Sievert, Nucl.Phys. B903 (2016) 164;
I.Balitsky and A. Tarasov, JHEP 10 (2015) 017;
Y. V. Kovchegov, D. Pitonyak, and M. D. Sievert, JHEP 1601 (2016) 072.
[80] CMS Collaboration, Eur. Phys. J. C74 (2014) 2951;
ALICE Collaboration, Phys. Rev. C91 (2015) 064905.
[81] D. Kharzeev, E. Levin and L. McLerran, Nucl. Phys. A 748 (2005) 627.
J. Jalilian-Marian, Prog.Theor.Phys.Suppl. 187 (2011) 123, arXiv:1011.1601.
[82] E. Braidot for the STAR Collaboration, arXiv:1008.3989.
[83] PHENIX Collaboration, Phys. Rev. Lett. 107 (2011) 172301.
[84] C. Marquet, Nucl. Phys. A796 (2007) 41.
[85] J. L. Albacete and C. Marquet, Phys.Rev.Lett. 105 (2010) 162301.
[86] Z.-B. Kang, I. Vitev and H. Xing, Phys.Rev. D85 (2012) 054024.
[87] M. Strikman and W. Vogelsang, Phys. Rev. D83 (2011) 034029.
[88] J. Jalilian-Marian and A.H. Rezaeian, Phys. Rev. D86 (2012) 034016.
[89] J. L. Albacete and C. Marquet, Nucl.Phys. A854 (2011) 154.
[90] K. J. Eskola, H. Paukkunen, and C. A. Salgado, JHEP 0807 (2008) 102.
[91] A. Rezaeian, Phys. Rev. D86 (2012) 094016.
[92] T. Sjöstrand, S. Mrenna, and P. Skands, Comp. Phys. Comm. 178 (2008) 852.
[93] Di-jet production from PYTHIA-8.189 is scaled down due to its overestimation of inclusive
π^0 yields compared to those reported by BRAHMS in Phys. Rev. Lett. 98 (2007) 252001
and STAR in Phys. Rev. Lett. 97 (2006) 152302.
[94] S. Chatrchyan et al. (CMS) 2012 Eur. Phys. J. C72 2012, arXiv:1201.3158
Dumitru A, Gelis F, McLerran L and Venugopalan R 2008 Nucl.Phys. A810 91–108,
Dusling K and Venugopalan R 2012 Phys.Rev.Lett. 108 262001,
Kovner A and Lublinsky M 2011 Phys.Rev. D83 034017,
Schenke B, Schlichting S and Venugopalan R 2015 Phys.Lett. B747 76–82,
Dusling K, Tribedy P and Venugopalan R 2016 Phys. Rev. D93 014034
[95] S. Chatrchyan et al. (CMS Collaboration) 2013 Phys.Lett. B718 795–814 (Preprint 1210.5482),
B. Abelev et al. (ALICE Collaboration), Phys.Lett. B719 (2013) 29;
G. Aad et al. (ATLAS Collaboration), Phys.Rev.Lett. 110, 182302 (2013).
[96] V. Khachatryan et al. (CMS) 2016 Phys. Rev. Lett. 116 172302, JHEP 1009 (2010) 091.
[97] B. Abelev et al. (ALICE Collaboration), Phys.Rev.Lett. 110, 082302 (2013).
[98] Paul Romatschke, Eur.Phys.J. C77 (2017) no.1, 21
[99] P. Bozek and W. Broniowski, Phys. Rev. C88, 014903 (2013), arXiv:1304.3044,
P. Bozek, W. Broniowski, and G. Torrieri, Phys.Rev.Lett. 111, 172303 (2013), arXiv:1307.5060,
A. Bzdak, B. Schenke, P. Tribedy, and R. Venugopalan, Phys.Rev. C87, 064906 (2013),
arXiv:1304.3403,
G.-Y.Qinand, B.Muller, Phys.Rev.C89,044902 (2014), arXiv:1306.3439,
K. Werner, M. Bleicher, B. Guiot, I. Karpenko, and T. Pierog, Phys.Rev.Lett. 112, 232301 (2014),
arXiv:1307.4379,

J. L. Nagle, A. Adare, S. Beckman, T. Koblesky, J. Orjuela Koop, D. McGlinchey, P. Romatschke, J. Carlson, J. E. Lynn, and M. McCumber, Phys. Rev. Lett. 113, 112301 (2014), arXiv:1312.4565.
B. Schenke and R. Venugopalan, (2014), arXiv:1405.3605 [nucl-th]
[100] A. Dumitru, F. Gelis, L. McLerran and R. Venugopalan Nucl.Phys. A810 (2008) 91
Dusling K and Venugopalan R 2012 Phys.Rev.Lett. 108 262001 (Preprint 1201.2658),
Kovner A and Lublinsky M 2011 Phys.Rev. D83 034017 (Preprint 1012.3398),
Schenke B, Schlichting S and Venugopalan R 2015 Phys.Lett. B747 76–82 (Preprint 1502.01331),
Dusling K, Tribedy P and Venugopalan R 2016 Phys. Rev. D93 014034 (Preprint 1509.04410)
[101] A. Adare, et al., Phys. Rev. Lett. 114 (19) (2015) 192301. arXiv:1404.7461,
A. Adare, et al., Phys. Rev. Lett. 115 (14) (2015) 142301. arXiv:1507.06273
[102] P.Romatschke, Eur.Phys.J.C75(7)(2015)305. arXiv:1502.04745,
B. Schenke, R. Venugopalan, Nucl. Phys. A931 (2014) 1039–1044. arXiv: 1407.7557
[103] J. Adams et al. (STAR Collaboration), Phys.Rev.Lett. 95, 152301 (2005);
B. Abelev et al. (STAR Collaboration), Phys.Rev. C80, 064912 (2009);
B. Alver et al. (PHOBOS Collaboration), Phys.Rev.Lett. 104, 062301 (2010);
B. Abelev et al. (STAR Collaboration), Phys.Rev.Lett. 105, 022301 (2010),
[104] M. Asakawa et al., Proceedings of Quark Matter 2015, Kobe, Japan, Nucl. Phys. A 956, 332 (2016)
[105] Dumitru A, Gelis F, McLerran L and Venugopalan R., Nucl. Phys. A810 (2008) 91, arXiv:0804.3858
[106] P. Huo, J. Jia, S. Mohapatra, Phys. Rev. C 90, 024910 (2014)
[107] P. Tribedy et al., Proceedings of Quark Matter 2017, Chicago, IL, arXiv:1704.03845
G. Denicol, A. Monnai, B. Schenke, Phys. Rev. Lett. 116, 212301 (2016), 1512.01538
B. Schenke, S. Schlichting (2016), 1605.07158
[110] H. Niemi et al, Phys. Rev. Lett. 106, 212302 (2011), 1101.2442
[111] A. Aprahamian et al., "Reaching for the horizon: The 2015 long range plan for nuclear science" 2015, http://science.energy.gov/~/media/np/nsac/pdf/2015LRP/2015_LRPNS_091815.pdf
[112] B. Schenke and S. Schlichting (2016), arXiv:1605.07158
[113] P. Tribedy [STAR Collaboration], arXiv:1612.05593 [nucl-ex].
[114] P. Bozek et al, Phys. Rev. C83, 034911 (2011). J. Jia and P. Huo, Phys. Rev. C90, 034915 (2014),
L.-G. Pang et al, Eur. Phys. J. A52, 97 (2016), arXiv:1511.04131 [nucl-th].
[115] V. Khachatryan et al. (CMS), Phys. Rev. C92, 034911 (2015).
[116] A. Bzdak, D. Teaney, Phys. Rev. C87(2), 024906 (2013), 1210.1965
[117] J. Jia, S. Radhakrishnan, M. Zhou (2015), 1506.03496
[118] ATLAS detector, Tech. Rep. ATLAS-CONF-2015-051, URL : http://cds.cern.ch/record/2055672
[119] A. Monnai, B. Schenke (2015), arXiv:1509.04103
[120] A. Mazeliauskas, D. Teaney (2015), 1509.07492
[121] R.S. Bhalerao, J.Y. Ollitrault, S. Pal, D. Teaney, Phys. Rev. Lett. 114(15), 152301 (2015), 1410.7739
[122] STAR Collaboration (Adamczyk, L. et al.) arXiv:1701.06496 [nucl-ex],
STAR Collaboration (Adamczyk, L. et al.) arXiv:1701.06497 [nucl-ex]
[123] L.G. Pang, G.Y. Qin et al., arXiv:1410.8690 (2014); private communication.
[124] S. Jowzaee for the STAR Collaboration, Proceedings of Quark Matter 2017, Chicago, IL.
[125] L. Adamczyk et al, Nature 548, 62 (2017), F. Beccattini et al. EPJC 75(2015)406; H. Li et al., Phys.Rev. C96 (2017) 054908
[126] A. Dobrin (ALICE), Nucl. Phys. **A904-905**, 455c (2013), arXiv:1211.5348 [nucl-ex] .
[127] G. Aad *et al.* (ATLAS Collaboration),
https://atlas.web.cern.ch/Atlas/GROUPS/PHYSICS/CONFNOTES/ATLASCONF-2014-022.
[128] O. D. Tsai, et al., Journal of Physics: Conference Series 404 (2012) 012023 'Results of R&D on a new construction technique for W/ScFi Calorimeters'
Y. Fisyak et al., NIM A 756(2014) 68-72' Thermal neutron flux measurements in the STAR experimental hall'.
O. D. Tsai, et al., Journal of Physics: Conference Series 587(2015) 01205 'Development of a forward calorimeter system for the STAR experiment'
[129] L. Aphecetche et al., The PHENIX calorimeter, NIM A499 521-536 (2003)
[130] W. Vogelsang, private communication (2013).
[131] D. de Florian, *Phys. Rev.* **D79**, 114014 (2009).
[132] D. Boer and P. J. Mulders, Phys. Rev. **D 57**, 5780 (1998).
[133] T. Rogers, Phys. Rev. **D 88**, 1, 014002 (2013).

[134] Y. Fisyak *et al*., Nucl. Instr. & Meth. A756 (2014) 68
[135] B. Alver et al (PHOBOS Collaboration), Phys. Rev. C83, 024913 (2011).
[136] Y. Fisyak, O. Tsai, F. Videbæk and Z. Xu, Nucl. Instr. Meth. A756 (2014) 68-72
[137] A. Abusleme et al., Nucl.Instr. & Meth. A817 (2016) 85.
[138] V. Smakhtin et al., Nucl.Instr. & Meth. A598 (2009) 196.
[139] A. Abusleme et al., "Performance of a full-size small-strip thin gap chamber prototype for the ATLAS new small wheel muon upgrade", Nuclear Instruments and Methods in Physics Research A 817 (2016) 85–92
[140] V. Smakhtin, G. Mikenberg, A. Klier, Y. Rozen, E. Duchovni, E. Kajamovitz, and A. Hershenhorn, Thin Gap Chamber upgrade for SLHC: Position resolution in a test beam, Nucl. Instr. & Meth A598 (2009) 196.
[141] ATLAS New Small Wheel Technical Design Report, ATLAS-TDR-020-2013, June 2013